Non-canonical Wnt signalling in craniofacial skeletogenesis: Role of *wls*, *gpc4*, *wnt5b* and *wnt9a*

Irving Teck-Cheng Ling

MBBS, MRCEd

Submitted in fulfilment of the requirements for the degree of

Doctor of Philosophy

College of Medical, Veterinary and Life Sciences

University of Glasgow

Research by Furth at Centre for Regenerative Medicine, Harvard Medical School

2017

Declaration

I hereby declare that all work presented in this thesis is the result of my own work and experimentation. No part of this work has been submitted for consideration as part of any other degree or award at any other university.

Irving Ling

2017

Acknowledgements

I owe my deepest gratitude to my thesis supervisor, Dr Eric Liao at Harvard Medical School for supporting me throughout this project. I want to thank you for agreeing to take me into your lab and immersing me in a thriving environment at the Centre for Regenerative Medicine and Harvard Stem Cell Institute. It has been your dedicated reminder to focus my projects and manage my time that made everything possible to complete this thesis. You offered me independence and your astute guidance drove me to work harder and to push myself to expand my bandwidth.

I would express my sincere thanks to my other supervisors, Professor Andrew Hart and Dr Alastair Gracie. Without their determined support, this arrangement would not have been possible. Thank you for relentlessly defending my position and pushing me further to complete the research. I would like to thank Prof Hart for always believing in me and guiding me in every step.

I would also like to thank Dr Jenna Galloway at Harvard, a great mentor, collaborator and wonderful scientist who has inspired me to read and love science. Thank you for all our scientific discussions, experimentation help, mentoring sessions and fun times at the bowling alley with the rest of your lab. I would also like to thank Dr Patty Purcell, a dedicated mentor of mine whom I have the utmost honour of knowing during my time at Harvard. Her contagious positive attitude makes me always see the silver lining.

I am indebted to my postdoctoral mentors at the CRM, Lucie Rochard, Rishita Shah and Mor Grinstein. Lucie, you have been the cornerstone during my time at the lab. Thank you for teaching me everything I need to know on how to be/think like a scientist, sharing the ups and downs, drinking many cups of coffee together, discussing scientific ideas, offering me life advices and helping me carry on despite the bluest days. I am so privileged to have learnt developmental biology from you and to your other half, Antoine for never failing to offer a helping hand, scientific advice and to share a beer at any time. You both gave me so much courage and hope to carry on and I owe this thesis to you.

Rishita, thank you for being there to answer any of my questions about science, the laughs, the extended periods trying to work the two-photon, dissection discussions and many life advices. Thank you to your other half as well, Nandan for the many life advises, tennis

matches and scientific discussion. All the best to both of you at Columbia! Thank you Mor for always being so optimistic about science despite all odds and your extensive experience in everything in life. Thanks to Heather Dingwall too for all the science discussions, chats, laughs and sharing life as grad students! Not long now! I am grateful and honoured to have worked with such amazingly talented and genuine scientists.

I would also like to thank the other members of the Liao lab; Kusumika Murkherjee – for basically planting me on the ground from Day 1 and teaching me basic molecular biology. Thanks to Stefanie Monica-Gaster for sharing laughs, protocols and the corner lab desk. And thanks to the other lab members past and present, Mike Grimaldi, Renee Daigle (for looking after my fish), Kana Ishii, Edward Li, Yawei Kong and Brittany Garrity.

Finally, thank you to my parents, brother and sister. I am incredibly blessed to have their unconditional support and for pushing me to achieve my goals. Thank you for giving me hope.

A Shriners Research Grant and a National Institute for Dental and Craniofacial Research R03 grant supported the work presented in this thesis.

Abstract

Craniofacial development requires progressive morphologic change, proliferation, differentiation and organization of chondrocytes preceding osteogenesis. The Wnt signalling pathway has been involved in regulating bone development and maintenance. As they are fated to become bone, chondrocytes require Wnt to polarize and orientate appropriately to initiate the endochondral ossification program. Although the canonical Wnt signalling has been studied in the context of bone development, the effects of non-canonical Wnt signalling in regulating the timing of cartilage maturation and subsequent bone formation in shaping ventral craniofacial structure is not well understood. In this thesis, I examined the role of the non-canonical Wnt signalling pathway (through the study of the role of *wls, gpc4, wnt5b* and *wnt9a*) in regulating zebrafish Meckel's cartilage maturation to the onset of osteogenic differentiation. First, I show that disruption of *wls* resulted in a significant loss of craniofacial bone, whereas lack of *gpc4, wnt5b* and *wnt9a* resulted in severely delayed endochondral ossification. This demonstrates the importance of the non-canonical Wnt pathway in regulating coordinated ventral cartilage morphogenesis by directing chondrocyte polarity. Second, I found distinct cellular requirements within the body and midzone of the mandible. Without non-canonical Wnt signalling, chondrocytes within the midzone appear to remain in their prehypertrophic state and fail to elongate and stack. This may suggest the importance of Wnt signalling in determining jaw length and size. Third, I generated a double transgenic zebrabow line to allow cellular studies on dynamic cell behaviour during development. Finally, to further interrogate the role of Wnt signalling during chondrocyte maturation, I studied the role of intracellular Wnt trafficking. More recently, there has been increasing evidence that Wnt activity is not only regulated in the receiving cells but also on the level of its secretion (Gross and Boutros, 2013). By studying *wntless* (*wls*), a multi-transmembrane protein that shuttles Wnts from the Golgi to the plasma membrane, I found that *wls* trafficking through coat protein vesicles (COP) is key in neural crest specification and differentiation. These works provide important insights into the non-canonical Wnt signalling during endochondral bone formation and craniofacial lower jaw development.

Table of Content

List of figures and tables

List of abbreviations

6-FAM	6 carboxyfluorescein
A-C-T-G	Adenine, Cytosine, Guanine, Thymine
AP	Anterior posterior
ATAC-seq	Assay for transposase-accessibility chromatin using sequencing
ATF6a	Activating transcription factor 6a
BCIP	5-bromo 4-chloro 3-ondolyl phosphate
Bglap	Osteocalcin
BiP	Binding immunoglobulin protein
BMP	Bone morphogenetic protein
Bp	Base pair
$CaCl_2$	Calcium chloride
cDNA	Complement DNA
ChIP	Chromatin immunoprecipitation
Col10a1	Type X collagen
Col1a1	Type 1 Collagen
Col2a1	Type II collagen
COP	Coat protein complex
CRISPR	Clustered regularly Interspaced Short Palindromic Repeats
CTGF	Connective tissue growth factor
dCAPS	Derived cleaved amplified polymorphic sequence
DLX2A	Distal-less homeobox 2a
DMSO	Dimethylsulfoxide
Dpf	Days post fertilization
DSB	Double stranded break
DV	Dorsal Ventral
EMT	Epithelial mesenchymal transition
ENU	N-Ethyl-N-nitrosouea
ER	Endoplasmic reticulum
EVL	Enveloping layer
FGF	Fibroblast growth factors
FNP	Frontonasal prominence
FOXD3	Forkhead Box Protein D3
FRET	Fluorescence resonance energy transfer

Fwd	Forward primer
FZD	Frizzled
gDNA	Genomic DNA
GPC4	Glypican-4
GPR177	Wntless (WLS)
HDR	Homologous-directed repair
HMG	High mobility group
Hpf	Hours post fertilization
HSP	Heat-shock protein
IACUC	Institutional Animal Care and Use Committee
IHH	Indian hedgehog
IRE1a	Inositol-requiring protein a
KCl	Potassium chloride
KOH	Potassium hydroxide
MAB	Maleic acid buffer
MBT	Midblastula transition
MeOH	Methanol
$MgSO_4$	Magnesium sulphate
Mitf	Microphthalmic-associated transcription factor
MMP13	Metalloproteinase 13
MnP	Mandibular prominence
mRNA	Messenger RNA
MTOC	Microtubule organizing centres
MxP	Maxillary prominence
NaCL	Sodium chloride
NaOH	Sodium hydroxide
NBT	Nitro blue tetrzolium chloride
NCC	Neural crest cells
NHEJ	Non-homologous end-joining
OPG	Osteoprotegerin
PA	Pharyngeal arch
PAM	Protospacre-adjacent motif
PBS	Phosphate buffered sulphate solution with tween
PBS	Phosphate buffered solution
PCP	Planar cell polarity
PCR	Polymerise chain reaction

PFA	Paraformaldehyde
PORCN	Porcupine
Rev	Reverse primer
SDS-Page	Sodium dodecyl sulfate polyacrylamide gel electrophoresis
SHH	Sonic hedgehog
SNP	Single nucleotide polymorphism
SOX	SRY-related HMG box
SP1	Osteopontin
SP7	Osterix
SPP1	Osteopontin
SRY	Sex determining region Y
SSC	Saline sodium citrate
TALE	Transcription activator like effectors
TCS	Treacher Collins Syndrome
TE	Tris-EDTA
UPR	Unfolded protein response
UTR	Untranslated region
Vegfa	Vascular endothelial growth factor A
WISH	Whole-mount in situ hybridization
WLS	Wntless
YSL	Yolk syncytial layer
ZFN	Zinc fingers

Chapter 1. Introduction

1.1 General introduction

The work in this thesis aspires to uncover the role of non-canonical Wnt signalling by studying several key genes; *wls, wnt9a, wnt5b* and *gpc4* during zebrafish craniofacial lower jaw development. The thesis is divided into 3 areas of interest; firstly, in studying the function of these genes *in vivo* and understanding how disruption affects proper shaping and maturation of chondrocytes as well as endochondral bone formation; secondly in developing a zebrafish transgenic tool to further our understanding of chondrocytes dynamic cell behaviour in craniofacial development and finally, in studying the role of trafficking and discussing endoplasmic reticular stress in chondrogenesis.

This introductory chapter includes a brief overview of *Danio rerio* as a model organism to study craniofacial development that will then branch into two sections, first describing zebrafish skeletal development and secondly highlighting molecular pathways involved in craniofacial development, focusing on the Wnt signalling pathway.

1.2. Craniofacial development

The head has the most complex architecture of the body and requires precise cellular and molecular interactions to form distinct shapes and structures. The combination of connective tissue, musculature, vasculature and innervations, derived from all germ layers; endoderm, mesoderm and ectoderm as well as the cranial neural crest cells all contribute to the craniofacial structure. Orchestrated signalling between all four cellular components towards the craniofacial mesenchyme (formed by cranial neural crest and mesoderm) help provide positional cues to determine growth, differentiation and shape. The modulation of this highly choreographed process makes it susceptible to genetic and environmental perturbations. As such, craniofacial anomalies such as orofacial clefts are the most common birth defect affecting approximately one in 800 live birth and results in a socioeconomic burden (Dixon et al., 2011). As much of the face is derived from neural crest cells (NCC), studying perturbations in signalling affecting this population will help us understand the mechanisms underlying craniofacial malformations.

NCC are defined as a transient population of multipotent stem cells that originate at the edge of the neural plate border (between the neural and non-neural ectoderm) and prospective epidermis (Sauka-Spengler and Bronner, 2010). They emerge from the neural

tube as it closes and undergo an epithelial to mesenchymal transition (EMT) by delaminating from the neuroepithelium and initiate extensive migrations to various parts of the embryo. Definitive NCCs are specified and initiate expression markers as premigratory cells within the dorsal neural tube. Soon after migrating to their final position, NCCs differentiate to form a wide range of derivatives such as neurons of the peripheral nervous system, melanocytes of the epidermis, craniofacial bone and cartilage, smooth muscles and parts of the cardiac outflow tract (Bronner and LeDouarin, 2012, Dupin et al., 2001). This diversity in cells and tissue derivatives led to the idea that neural crest constituted a 'fourth germ cell layer' (Hall, 2000). **Figure 1** summarizes the key steps during neural crest cell development (using a chick embryo as an example). Below, I summarize the process of neural crest formation, its role in craniofacial development and related birth malformations.

1.2.1. Neural crest induction

Neural crest induction is mediated by different signals including FGFs, BMPs and WNTs that are secreted from surrounding tissues, forming gradients. Convergence of BMP gradient from the ectoderm, ectoderm-derived Wnt and mesoderm-derived Fgf signalling triggers upregulation of transcription factors such as *Msx1/2*, *Pax3/7, Dlx5, Gbx2* and *Zic1* (Basch et al., 2006, Betancur et al., 2010, Huang and Saint-Jeannet, 2004). Collective regulation and expression of these genes, designated as 'neural plate border specifiers', at the neural plate border region then leads to neural crest specification.

1.2.2. Neural crest specification

The neural plate border specifier genes subsequently activate a different set of transcription factors in the dorsal neural tube that includes genes like *Snail2, FoxD3, Ets-1, Sox8/9/10, Slug* and *c-Myc*. These genes control cell cycle, proliferation, survival, delamination and promite epithelial-mesenchymal transition (EMT). They regulate downstream effector genes to start promoting migration; at which point the NCCs have specified and become an identifiable distinct population of multipotent migratory stem cells with the capacity for self-renewal (Bhatt et al., 2013). Interestingly, this stemness has been seen in adult neural crest cells in niches that can be readily isolated, purified, cultured and potentially used in clinical therapeutic applications (El-Nachef and Grikscheit, 2014, Greiner et al., 2014, Konig et al., 2014).

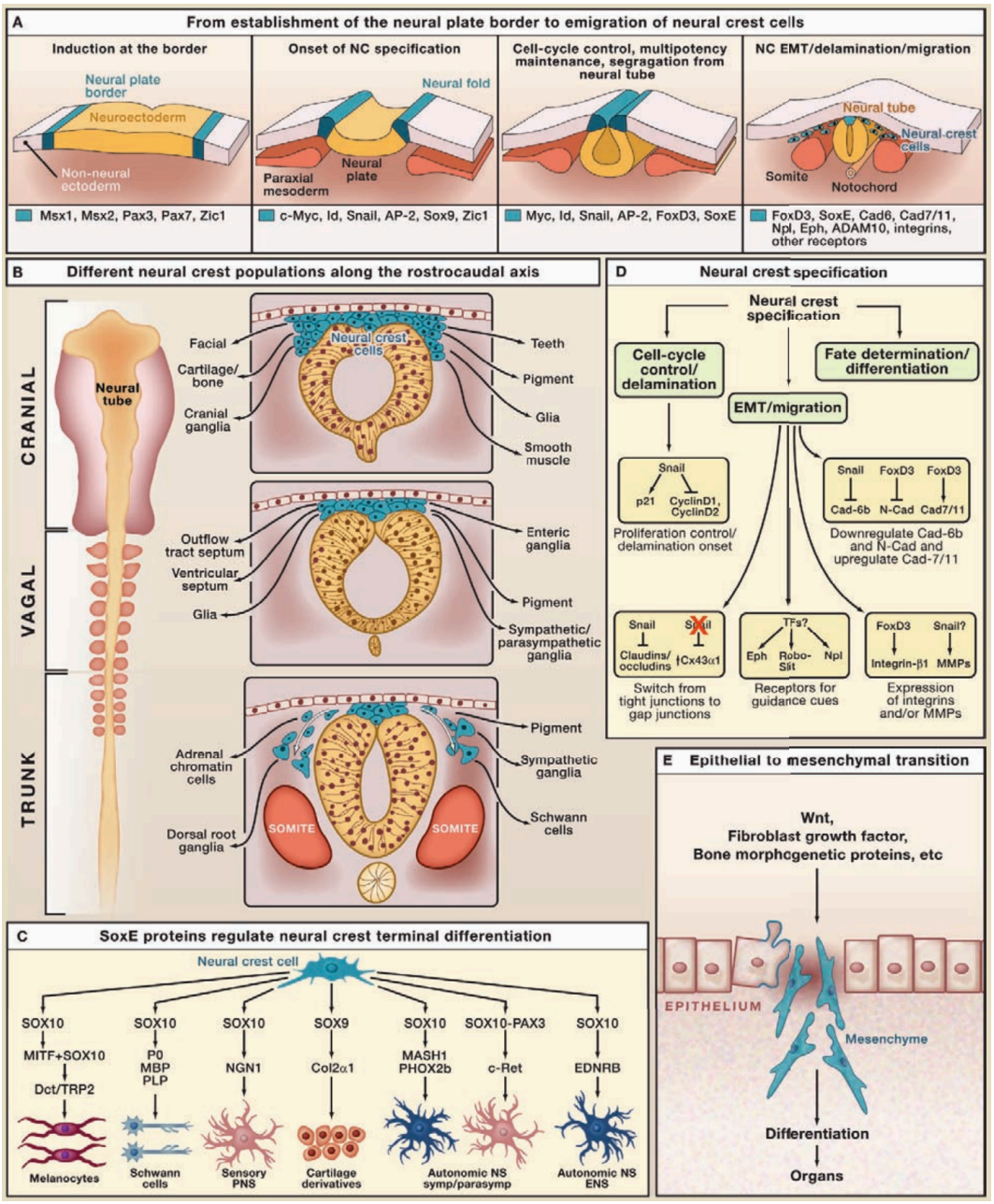

Figure 1. An overview of neural crest development directly taken from (Sauka-Spengler and Bronner, 2010).

The diagram provides a snapshot of key events during neural crest formation, migration and differentiation.

1.2.3. Neural crest migration and differentiation

Following EMT, NCCs migrate throughout the embryo and respond to various intrinsic and extrinsic signals to promote their proliferation and survival. Neural crest cell specifier genes repress epidermal and neural tube markers such as *Sox2* and *E-cadherin* and upregulate factors such as cadherin-y and matrix metalloproteinases. This facilitates

migration by enabling EMT and promiting NCC delamination from the neuroepithelium (Bronner and LeDouarin, 2012, Milet and Monsoro-Burq, 2012).

NCCs can be categorized as cranial, cardiac, vagal, trunk and sacral based on their axial position and the tissues they contribute to during their terminal differentiation (Bhatt et al., 2013). Cranial NCCs give rise to craniofacial bone and cartilage along with neurons and glia of the cranial ganglia, smooth muscle and pigment cells. They contribute to craniofacial structures through their differentiation into chondrocytes to form cartilage anlages, osteoblasts to form bone and odontoblasts to produce teeth and dentine. Non-cranial NCC derivatives include various cardiac structures, the enteric nervous system, melanocytes, secretory cells, neurons and glia of the peripheral nervous system and the sympathetic ganglia. (Burns and Douarin, 1998, Burns and Le Douarin, 2001, Simoes-Costa and Bronner, 2013). The next section will focus on craniofacial development.

1.2.4. Neural crest cell in craniofacial development

Following delamination from the neural tube, cranial neural crest cells (CNCC) begin their migratory path to help form the facial prominences. The frontonasal prominences (FNP) arise from CNCC that migrated from the diencephalon and anterior mesencephalon while CNCC from the posterior mesencephalon and rhombomeres 1 and 2 of the hindbrain populate the first pharyngeal arch (PA1) which then forms paired maxillary prominences (MxP) and paired mandibular prominences (MnP) (Wilkie and Morriss-Kay, 2001). The face subsequently forms by integrated fusion of these five facial primordia, the FNP with the paired MxP and MnP that surrounds the oral cavity (**Figure 2**). Invagination of the nasal placodes then forms the medial and lateral nasal prominences to ultimately shape the future nose (Minoux and Rijli, 2010). Failure of the fusion of these prominences will result in orofacial clefts (Jiang et al., 2006).

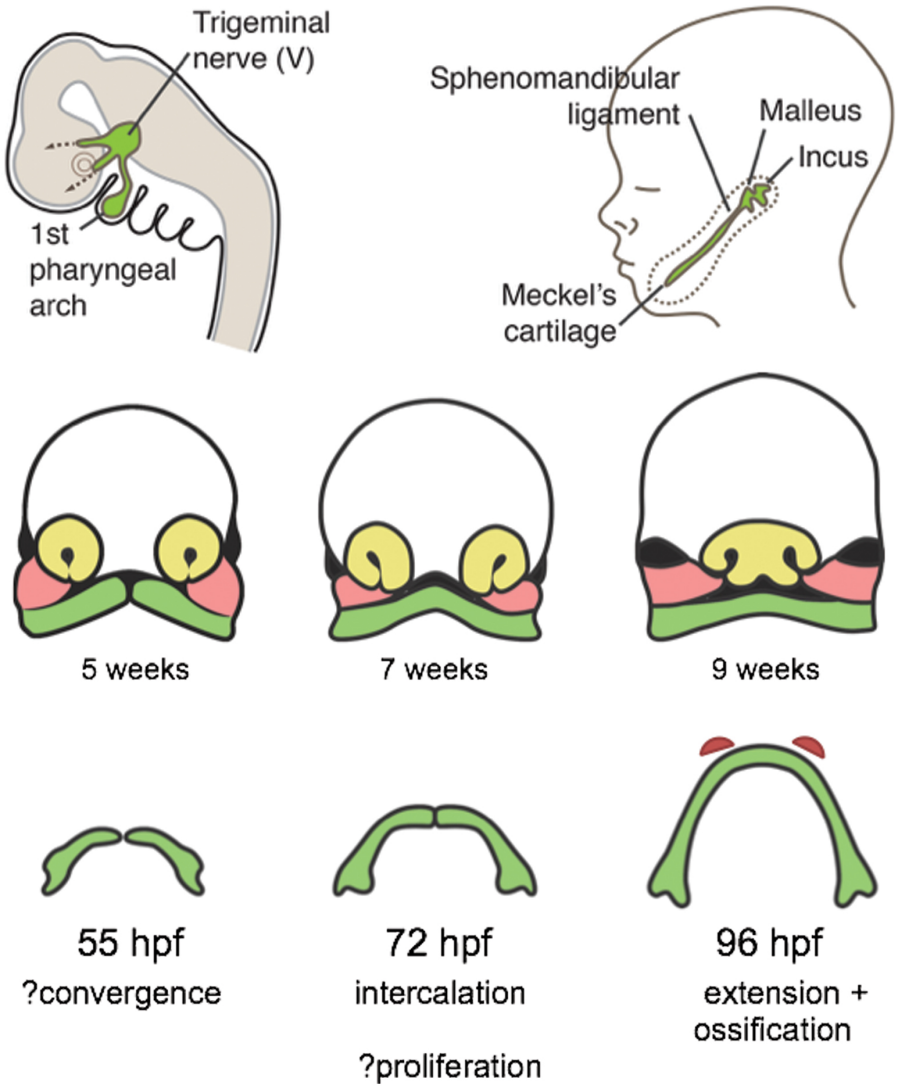

Figure 2. Mandibular development and homology between humans and zebrafish

Top left figure represents a human embryo highlighting the 1st pharyngeal arch and is fated to become the future mandible amongst other structures. The top right figure shows the 1st pharyngeal arch derivatives. The middle figure shows the developing Mandibular prominence (green), maxillary prominences (red) and nasofrontal prominence, a protrusion of the maxillary prominence (yellow). The mandibular prominence appears to fuse by 7 weeks in utero. The bottom figure shows the developing Meckel's cartilage in zebrafish where two separate prominence fuses around 55 hpf and forms an arch by 96 hpf. The red protrusions in the bottom right figure shows the future dentary bone formation.

A key downstream gene reported to cause syndromic Van der Woude syndrome (OMIM 119300) with cleft lip with or without cleft palate was *IRF6* that was first reported in 2002 (Kondo et al., 2002). Since then, a wealth of research has looked at regulation of *IRF6* including the importance of the WNT-p63-IRF6 signalling at the lambdoidal junction (fusion of the MxP and FNP). Another factor, Sonic hedgehog (SHH) has also been

implicated in correct fusion at this lambdoidal junction through modulating Wnt signalling (Kurosaka et al., 2014).

The mandible is derived from the MxP and mandibular processes of the 1st pharyngeal arch with patterning signals arising from the foregut endoderm as well as surrounding CNCC derived mesenchyme (Couly et al., 2002, Rochard et al., 2016). Endothelin plays a key role in directing post-migratory CNCC to PA1 and mandibular process. *Endothelin-1* is highly expressed in PA1 in the surrounding ectodermal epithelium of the mandibular process and signalling is through endothelin receptor type A (Ednra), which is present in the underlying NC-derived mesenchyme. Defects in *Ednra* as seen in *Ednra* null murine embryos showed an increase in apoptosis of NC-derived mesenchymal cells. Developmental abnormalities that are most common to the mandible include micrognathia or retrognathia with midline clefting defects being less common. One syndrome that includes micrognathia as a phenotype includes Treacher Collins syndrome (TCS, OMIM 154500). TCS is a craniofacial disorder with features including coloboma of the lid, micrognathia, microtia, hypoplastic zygomatic arches, cleft palate, slanted palpebral fissures and macrostomia. The genetics of TCS highlights the many different signalling pathways involved in early craniofacial patterning and trophic skeletal morphogenesis.

Therefore, to further our understanding of the developmental mechanisms behind these malformations, we turned to basic developmental biology work to uncover cellular signalling pathways in morphogenesis. I use zebrafish, a telost fish as a powerful model organism to study craniofacial development and subsequently focused on the Wnt signalling pathway in mediating the shaping of craniofacial skeletal elements.

1.3. Zebrafish as a model organism

Craniofacial structures and morphologies are enormously diverse with the fundamental signalling pathways and cellular events that control the nascent skeleton found to be highly conserved from fish to humans. The zebrafish, *Danio rerio,* has been a popular model to study craniofacial development since the 1990s. Major differences exist between zebrafish and other mammals such as human or mouse model but *Danio rerio* present great strengths and advantages over other laboratory animals. Strengths of the zebrafish model include being low-cost for rearing facilities, short breeding cycle, high fecundity and prolific layers (around 600 eggs per week). Zebrafish undergo rapid *ex utero* embryonic development

making it possible to observe different structures in the embryo and therefore, an excellent tool for researchers to observe key steps of development as they are happening in real time. Additionally, zebrafish have a simplified skeleton during early larval stages, and are amenable to transgenesis and complex genetics. In addition, genetic manipulation of the embryos such as mRNA injections can be achieved. Apart from some of the primitive advantages of teleost as model organism, zebrafish exhibit adaptive radiation and trophic polymorphism making it valuable in understanding how key pathway members affect trophic structures and diversification (Hulsey et al., 2005). Lastly their transparency and size enables easy visualization of the embryo at high resolution through single and multi-photon microscopy, allowing for their study in real time.

Sequencing of the zebrafish genome has demonstrated that many of zebrafish genes present very good homology to their human orthologues thereby human mutations can easily be studied in zebrafish with reliable transferability. In fact, cancer models such as melanoma have used zebrafish for large scale chemical screens. Additionally, it remains a popular model in developmental studies. One of its most advantageous characteristics is susceptibility to gene manipulation with reliable genotype-phenotype correlations. This led to the use of N-Ethyl-N-Nitrosouea (ENU) or viral insertional mutagenesis that have uncovered many genes involved in complex developmental processes (Driever et al., 1996, Neuhauss et al., 1996, Amsterdam et al., 1999, Amsterdam et al., 2004, Gaiano et al., 1996, Golling et al., 2002). More recently, gene editing using CRISPR/Cas9 has enabled quicker and more efficient studies of gene function in zebrafish. These papers used mutants known to disrupt *wntless (c186;* ENU*),*(Yu et al., 2014), *wnt5b (hi12735;* viral insertion*), gpc4 (hi1688;* viral insertion*)* (Rochard et al., 2016, Sisson et al., 2015) and *wnt9a* (CRISPR editing) (Rochard et al., 2016). To understand zebrafish a model organism for developmental studies, I will briefly discuss the important aspects of its embryo development as well as highlighting craniofacial morphogenesis.

1.3.1. Brief zebrafish embryology

Zebrafish embryos develop rapidly. Within the first 72 hours, a single cell will develop into a free-swimming larva with all major axes, organs and structures patterned. These first 3 days are divided into seven periods of early development: zygotic, cleavage, blastula, gastrula, segmentation, pharyngula, hatching and early larva (Kimmel et al., 1995) (**Figure 3**).

The zygotic stage covers the first 40 minutes and starts following fertilization and ends when the first cleavage occurs. Fertilization activates cytoplasmic movements that stream from the granule-rich yolk towards the animal pole and segregates to form a blastodisc (one-cell). This process continues into the cleavage phase. The cleavage period starts upon the first cleavage of the cell or blastomere that continues to divide at approximately 15-minute intervals. They undergo meroblastic divisions (incomplete undercutting of the blastomeres) and remain interconnected by cytoplasmic bridges. The first five cleavages are confined to the animal pole at regular orientations and the sixth cleavage occurs in the horizontal plane, resulting in a two-tiered arrangement of cells. This regular succession of cleaves will continue until the tenth time, marking the start of the blastula period, a time when the blastodisc begins to look ball-like (approximately 128-cell stage) (Kimmel et al., 1995).

Three important processes occur during the blastula period: midblastula transition (MBT), formation of the yolk syncytial layer (YSL) and epiboly begins. Cells of the blastula divide metasynchronously whereby blastomeres near the pole enter the mitotic division wave first and the marginal cells last. Lengthening of cell cycle marks the onset of MBT (tenth cell cycle; 512-cell stage). Here, the interphases lengthen, cells become motile and RNA synthesis increases over background maternal mRNA levels (i.e. the cells are synthesizing their own mRNA). The marginal blastomeres in the early blastula lie against the yolk cell and remain cytoplasmically connected throughout cleavage period. At the start of the 10^{th} cycle, cells are further divided into three distinct populations: 1) the enveloping layer (EVL) forming the periderm or outer most layer that acts to surround and protect the embryo, 2) the deep cell layer, which develops into the embryo proper and 3) the yolk syncytial layer (YSL), formed from marginal cells that collapses, releases their cytoplasm and nuclei into the immediately adjoining cytoplasm of the yolk cell. The YSL is unique to teleost and does not directly contribute to the body of the embryo. Its role is to drive epiboly that begins at late blastula.

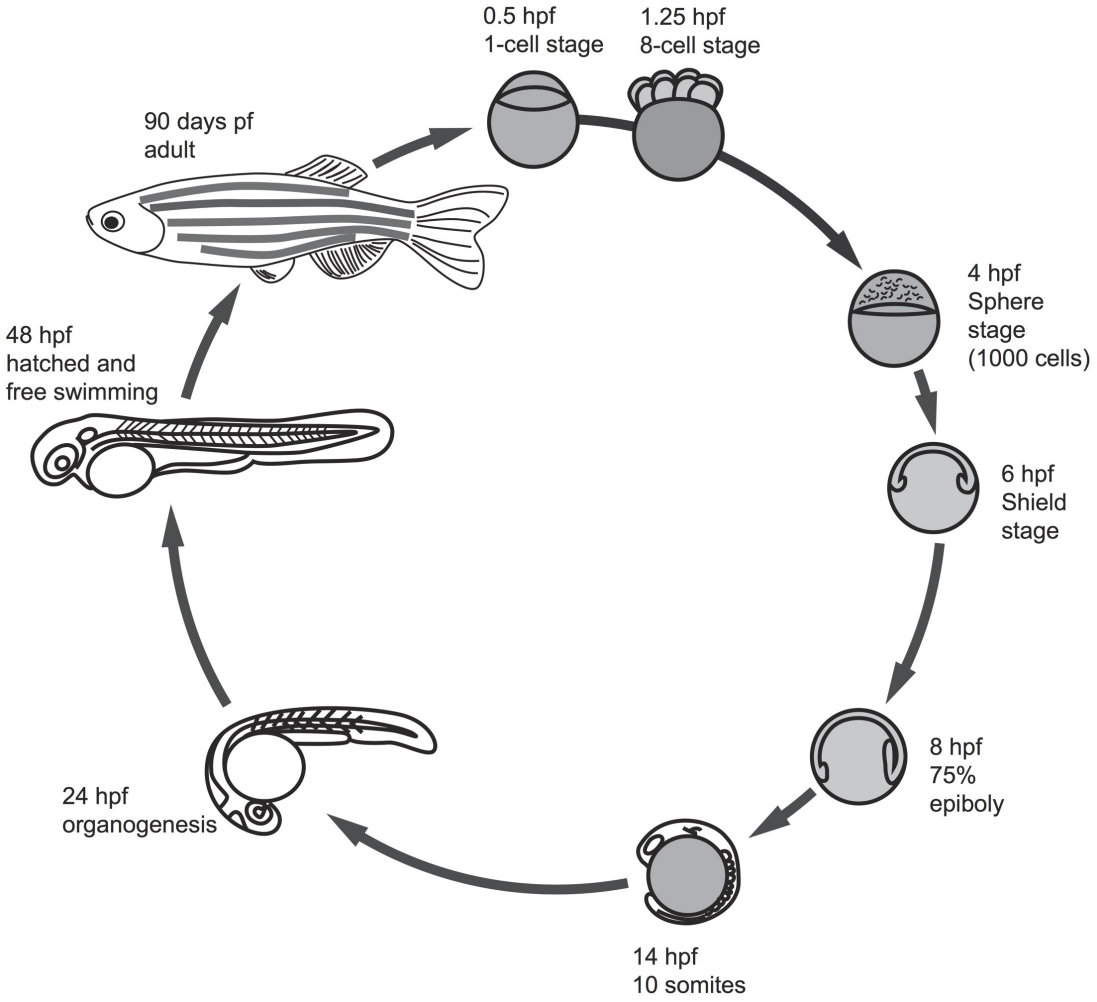

Figure 3. Schematic representation of zebrafish life cycle from zygotic stage till adulthood.
Representative diagrams at different stages starting with zygotic period (1 cell), cleavage period (8-cells), blastula period (sphere), gastrula (shield and 75%-epiboly), segmentation (10-somite), pharyngula (Prim-5 24hpf), hatching period (long-pec, 48hpf) and finally adulthood around 90 days where they are fertile. (Adapted from "Stages of embryonic development in zebrafish (Kimmel et al., 1995)).

Epiboly represents the first major morphogenetic movement of the embryo and is the thinning and spreading of the YSL and blastodisc over the yolk cell to eventually engulf it completely. The bulging/doming of the inner YSL toward the animal pole marks the clearest sign of epiboly. Epiboly relies on functional microtubules to generate the force necessary for coordinated movement of cells of the blastoderm from their animal location towards the vegetal pole. Changes are also observed in the EVL where it flattens and stretches to surround the embryo and form a tightly sealed epithelial monolayer (Bennett and Trinkaus 1970).

As epiboly continues, involution, convergence and extension occur, producing the primary germ layers and the embryonic axis, thus marking the start of the gastrula period. This occurs at approximately 50% epiboly (percentage-fraction of yolk cell that the blastoderm covers) where a thickened marginal region or the germ ring appears. Involution produces this germ ring by folding the blastoderm back on itself. This rapid convergence of cells at one position of the germ ring causes epiboly to temporarily arrest at which point the embryo reaches shield stage. This marks the formation of the dorsal organizer termed the embryonic shield in zebrafish and is equivalent to the node in mouse, Hensen's node in chick and Spemann's organizer in amphibians (Hamburger, 1969, Zoltewicz and Gerhart, 1997). The embryonic shield reliably marks the dorsal side of the embryo as well as determining the Anterior-Posterior (AP) and Dorsal Ventral (DV) axes for the first time. After the shield has formed, epiboly resumes and the margin of the blastoderm advances around the yolk. Around 90% epiboly (determined by a small yolk plug protruding from the vegetal pole), the dorsal epiblast thickens anteriorly to form the neural plate (future brain) and the deep cell multilayer starts to differentiate into cells that will eventually form the notochord, axial somite-derived muscles and hindbrain neurons. At 10hpf, epiboly ends when the blastoderm completely envelops the yolk cells (100% epiboly). Soon after closure, the posterior end of the embryonic axis develops the tail bud. Just anterior to the tail bud lies the thickened neural plate along the embryonic axis where cells will contribute to trunk spinal cord. Thickening is prominent near the animal pole that forms the head. In addition, the prechordal plate is seen to accumulate deep, anterior to the neural plate forming a prominent bulge, or polster of cells (see Chapter 5 for highly specific *copa* expression in this region). This polster will begin to indent the yolk cell surface in the midline and will eventually contribute cells to the head (Kimmel et al., 1995).

As gastrulation ends following 100% epiboly, the segmentation periods begin. During this time, somites develop, major body axes are formed, the three germ layers become organized and the tail bud becomes more prominent. Somitogenesis appears sequentially from anterior to posterior and is most useful for staging. Somites consist of paired blocks of undifferentiated mesenchyme enclosed in epithelium that will differentiate into the myotome and sclerotome, both of which will then differentiate into muscle and trunk cartilage structures respectively. At 4-5 somites stage and by the 8-10 somites stage, early rudiment of the pronephros is formed and early NCCs migrations occur. The next landmark is the otic placode that appears around 14 somites. This marks an important stage where three prominent subdivisions of the brain; prosencelphalon (that later divides into

telencephalon and diencephalon), mesencelphalon (midbrain) and rhombeencephalon (hindbrain), can be distinguished. The rhombomeres begin to take shape and neural crest starts migrating in streams in the head and trunk. Constriction of the yolk appears in the posterior region and gives it a kidney bean shape, thereby forming the extension from the rest of the yolk. Eventually around 30-34 pairs of somites form, exhibiting the chevron shape. Spontaneous myotomal contractions begin marking the end of segmentation stage and the beginning of the pharyngula period.

The pharyngula stage (24-48hpf) refers to when the embryo develops to the pholotypic stage and into a complex swimming vertebrate fish. Pigment cells differentiate and melanin deposition becomes visible, circulatory system forms and behavioural development can be observed through tactile sensitivity. At 24hpf (primitive-5 stage), the heart starts to beat and the pectoral fin buds form lateral to the 3rd somites. By 30hpf (prim-15 stage), the median dorsal stripe develops due to dorsal clustering of melanophores. Towards the end of the pharyngula stage (high-pec 42hpf), the mandibular and hyoid arches become well define and xanthophores and iridophores make an appearance.

The hatching period (48-72hpf) marks an important point in lower jaw morphogenesis. This section briefly describes the general changes that occur. (Detailed description of craniofacial morphogenesis is discussed in the next section). During this period, the pectoral fins, ventral cartilage structures and gills start to take shape. A small open mouth at around 48hpf (long-pec stage) can be readily observed midventral position between the eyes and provides a useful landmark for staging and imaging purposes. Differentiation of the first cartilage structures at the pectoral fin bud can be observed from a compact mesenchymal condensation. From here, chondrocytes can be observed along the trabeculae of the ethmoid plate and at around 55hpf, the Meckel's bud appears along with the palatoquadrate (Dougherty et al., 2012). At the protruding mouth stage (72hpf), the mouth is wide open and the Meckel's cartilage forms a unique arch that articulates in the midline with its other half as well as proximally with the palatoquadrate to form the jaw-joint. Gill slits can be observed at this stage and prominent buds of developing gill filaments including blood vessels. The first bone of the zebrafish, the cleithrum appears at the boundary between the first two myotomes and serves as an important anchor to the pectoral fin girdle. By the end of 3 dpf, the hatched larva has completed morphogenesis and soon after, ossification of the cartilaginous structures begins. The major aim of this thesis is to look at early craniofacial development stages during the hatching period and

how disruption of important signalling cues at the early stages (gastrulation) affects later development, shaping and patterning of skeletal structures and bone formation.

1.4. Zebrafish craniofacial development and anatomy

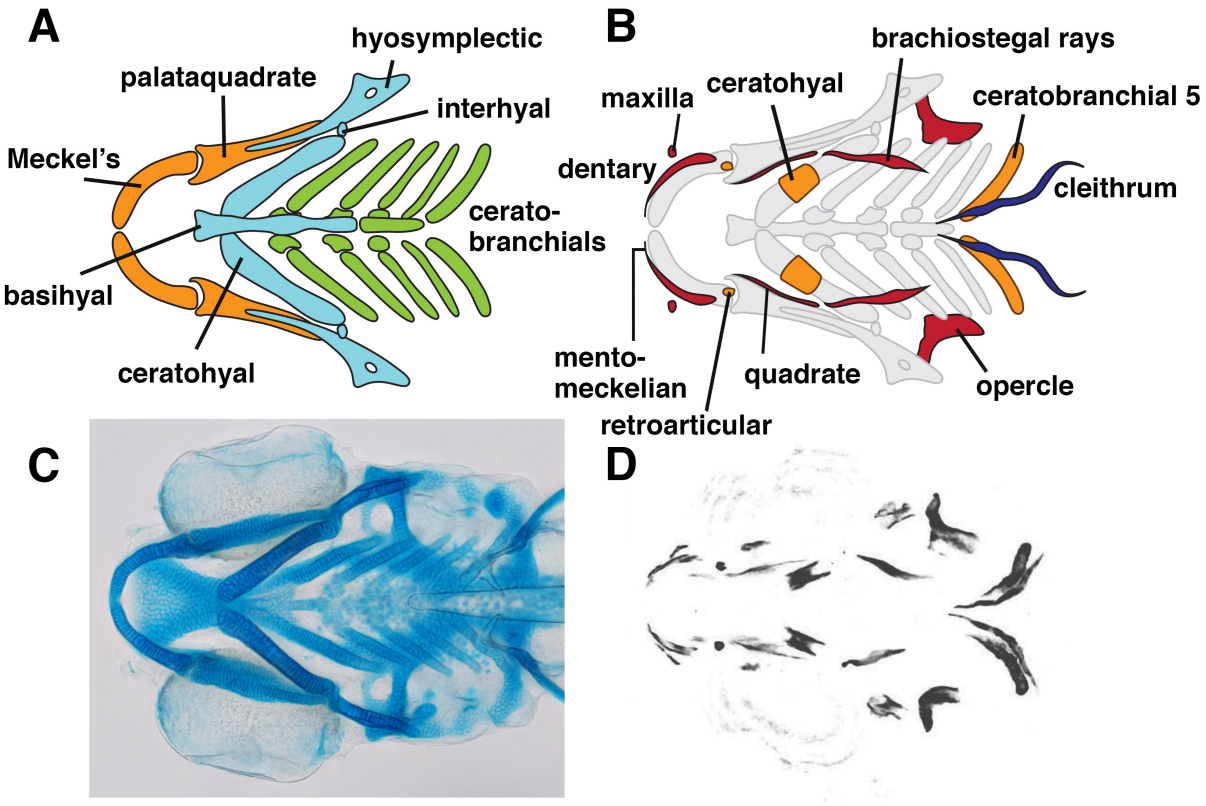

Figure 4. Graphic diagram of zebrafish ventral cartilage structures (left) and bones (right).
A. Names of corresponding cartilage structures. Orange indicates first pharyngeal arch derivatives, light blue – second arch derivative and green – third arch onwards derived. B. Names of craniofacial bones at 4 dpf. Red indicates neural crest cell derived intramembranous bone, orange indicated neural crest cell derived endochondral bone and blue mesoderm derived bone. C. Alcian blue stain of a 4 dpf larvae showing craniofacial cartilage structures. D. Whole mount Alizarin red stain of 4 days post fertilization (dpf) larvae.

Zebrafish have seven pharyngeal arches, which are primordial for trophic structures consisting of a core of mesoderm, followed by cranial neural crest cells (CNCC) and then lined externally by ectoderm and internally by endoderm (Mork and Crump, 2015). The arches are extensively patterned by surrounding signals as well as autocrine signals in NCC. *Hox* genes determine anterior-posterior axes while *Endothelin-1*, *Jagged-Notch*, *Bmp* and *Dlx* determines the dorsal-ventral axes, fine-tuned by Fgf, Hh and Wnt signalling to establish domain-specific skeletal blueprints (Kimmel et al., 2010, Mork and Crump, 2015).

The first pharyngeal arch will form skeletal elements of the anterior neurocranium, the ethmoid plate (homologous to the human primary palate) and anterior ventral cartilage structures notably the bilateral Meckel's cartilages that serve as a lower jaw. It also contributes to the dorsal palatoquadrates that articulate with Meckel's to form the jaw joint, pterygoid processes of the palatoquatrate that forms articulation with the ethmoid plate (**Figure 4**). The second or hyoid arch forms the dorsal hyosymplectics and ventral ceratohyals that are connected by interhyals to create hinge or hyoid joints. The ceratohyals are linked in the midline to the basihyal cartilage. The hyosymplectic connects the central cartilage structures to the posterior neurocranium via the anterior part of the otic cartilage. This secures the jaw skeleton to the head. The posterior arches 3-7 will form 5 paired ceratobranchial cartilages that support gill tissues (Piotrowski et al., 1996, Schilling et al., 1996). The fifth pair of ceratobranchial forms several ossified pharyngeal teeth (Kimmel et al., 2010) but have evolved independently of the more anterior cartilage structures and are not present in all teleost fish (Hulsey et al., 2005, Mehta and Wainwright, 2008). The final organized shape and pattern of the cartilage structures are summarized in (**Figure 4**).

The general pathways involved in patterning the pharyngeal arches and cartilage structures have been shown to be highly conserved across vertebrates (Mork and Crump, 2015). One example of conservation between mice and zebrafish is mutations in the Endothelin-1 (Edn1) pathway that results in changes to the mandible in mice mutants (Kurihara et al., 1994) as well as defective Meckel's and ceratohyals in zebrafish *edn1* mutants (Miller et al., 2000). In a *Dlx5/6* mice mutant, two downstream Edn1 targets, homozygotes displayed a homeotic transformation of the lower to upper jaw suggesting key roles of the pathway in lower jaw morphogenesis (Depew et al., 2002).

This deep conservation across species during early craniofacial development justifies the use of zebrafish as a model to study other pathways involved during this process (Mork and Crump, 2015). To further justify the model, skeletal elements in the zebrafish head have homologs in mammals. The first pharyngeal arch derivatives such as the malleus and incus of the mammalian middle ear have been found to be evolutionarily homologous to the posterior end of Meckel's cartilage and palatoquadrate in zebrafish (Anthwal et al., 2013). Similarly, the stapes, a second arch derivate has connections to the hyomandiblar and otic cartilage in fish.

1.5. Skeletal development

Skeletal development is conserved among vertebrates and involves two processes; skeletal patterning to define the shape and location within the body and then differentiation of skeletal progenitors (Olsen et al., 2000). As described in the previous chapter, many of the facial bones and the cranium are derived from NCC compared to the parietal and axial bones derived from the paraxial mesoderm and the sternum and long bones formed from the lateral plate mesoderm. Despite these three separate cell lineages to form different bony structures, each gives rise to a common bone matrix secreting cell; the osteoblast (Rodda and McMahon, 2006, Olsen et al., 2000).

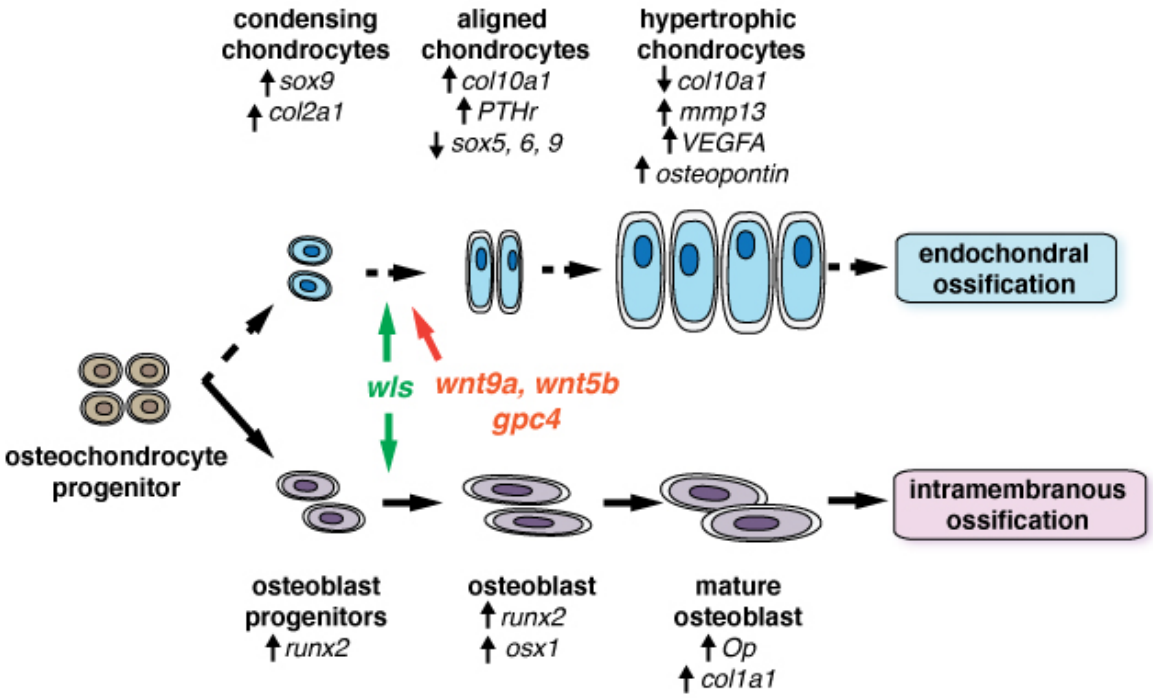

Figure 5. Summary of bone formation pathway showing both endochondral and intramembranous ossification process with genes implicated in each stage process.

Bone formation involves two mechanisms, intramembranous and endochondral ossification (summarized in **Figure 5**). Intramembranous ossification defines the direct differentiation of mesenchymal progenitors into osteoblasts for the formation of many of the bones of the skull and face. This thesis focuses on endochondral ossification which, in contrast, requires that a chondrocyte cartilaginous anlage anticipates bone formation at a later stage (Kronenberg, 2003). The general pathway involves chondrocytes differentiation

from NCCs that subsequently undergoes maturation, hypertrophy and later apoptosis to leave behind a matrix for invasion of osteoblasts to deposit bone.

On a molecular level (summarized from (Kronenberg, 2003), this complex process starts with *Sox5*+, *Sox6*+, *Sox9*+ mesenchymal cells condensing at their terminal location to form chondrocytes. These chondrocytes are immature proliferating cells and produce extracellular matrix proteins such as type II collagen (*Col2a1*). Within the prehypertrophic and hypertrophic zones, chondrocytes start to mature, enlarging and becoming more distant from each other. Here, *Sox5*, *Sox6* and *Sox9* are down-regulated while parathyroid hormone 1 receptor and Indian hedgehog (*Ihh*) are upregulated to initiate the formation of hypertrophic chondrocytes. Hypertrophic chondrocytes then start to express type X collagen (*Col10a1*) and connective tissue growth factor (*Ctgf*) (Mackie et al., 2008). At this stage, osteoblast progenitors also start to mature within the periochondrial cells, an inner layer lying adjacent to the hypertrophic chondrocytes. Hypertrophic chondrocytes then down regulate *Col10a1* and upregulate vascular endothelial growth factor A (*Vegfa*), metalloproteinase 13 (*Mmp13*) and osteopontin (*Spp1*) to recruit endothelial cells and osteoprogenitors from the periochondrium to invade the cartilage matrix left behind from the apoptotic chondrocytes (Olsen et al., 2000). Osteoblast precursors initially start expressing *Runx2*, master regulator of bone and cartilage cell fate and then they express *Sp7* (*Osterix*), master regulator of osteoblastogenesis and type I collage (*Col1a1*) as they differentiate into early osteoblast. Osteoblasts mature even further and start to express mineralization genes such as *Sp1* (*Osteopontin*) and *Bglap* (*Osteocalcin*) (Nakashima et al., 2002).

Hedgehog (HH) signalling plays important roles in the regulation of endochondral ossification (Karsenty, 2003). Ihh is produced by hypertrophic chondrocytes and signals to not only adjacent pre-hypertrophic chondrocytes to induce proliferation but also to overlying perichondral cells to induce osteoblasts differentiation (Long et al., 2006, St-Jacques et al., 1999). This was evident when the deletion of *Ihh* co-receptor *Smo* in perichondral lineage cells led to a loss of endochondral bone resulting in cells adopting an alternate chondrogenic fate (Long et al., 2004). In contrast, elevation of Hh signalling through loss of its negative regulators *ptc1* and *ptc2* initiates osteoblast differentiation program in chondrocytes (Hammond and Schulte-Merker, 2009).

While the central dogma of endochondral ossification is the formation of bone over apoptotic chondrocyte scaffold, it has been suggested that some chondrocytes escapes this process and transdifferentiate to long-lived osteocytes or osteoblasts (Paul et al., 2016, Yang et al., 2014, Zhou et al., 2014). In teleost, several studies have eluded to the direct differentiation of periochondral cells to form endochondral bones within the developing larvae (Eames et al., 2012, Hammond and Schulte-Merker, 2009, Paul et al., 2016). Perichondral cells are affected by *ihha* signalling (Hammond and Schulte-Merker, 2009). However, how these cells receive *ihha* signal from the underlying hypertrophic chondrocyte and how the cartilage anlage affect bone development has yet to be explored.

In addition to HH signalling, Wnt signalling also plays a critical role in skeletogenesis and bone homeostasis (Monroe et al., 2012). As Wnt mutations affect craniofacial chondrogenesis, studying the mutants in the context of bone formation will be advantageous. Below, I summarise Wnt signalling, the role of both the canonical and non-canonical pathways and then focus in on the non-canonical pathway.

1.6. Wnt signalling

Wnts are a family of secreted glycoproteins that play major roles during embryonic development. The Wnt signalling pathway is widely conserved across species from *Drosophila*, *Zebrafish, Caenorhabditis elegans* to mammals and display several key embryonic functions such as cell fate specification, cell polarity and cell induction (Nusse and Varmus, 1982).

The first Wnt gene, originally termed *int-1,* was cloned from the mouse genome and originally found to be a frequent insertional target by the mouse mammary tumour virus (MMTV) that causes mammary gland tumourigenesis (Nusse and Varmus, 1982). Later, other mouse loci were also subsequently found to be integrated by the MMTV and aptly termed *int-2* (Dickson et al., 1984) and *int-3* (Gallahan and Callahan, 1987). However, these genes were found to be unrelated to *int-1* with *int-2* encoding fibroblast growth factor family 3 (*fgf3*) (Dixon et al., 1989) and *int-3* a member of the notch gene family (Robbins et al., 1992) with obvious different mechanisms and functions. It was then found that *int-1* encodes a novel secretory glycoprotein that is identical to the product of the Drosophila melanogaster *wingless* gene and that the Drosophila homologue (*Dint-1*) mapped to the same location to *wingless (Rijsewijk et al., 1987)*. Therefore, given that *int-1, int-2* and *int-3* were fundamentally unrelated and *int-1* and *wg* were similar, both *wingless* and *int-1* were amalgamated to *Wnt* with Wnt1 being the first Wnt gene to be characterized (Nusse et al., 1991).

Insight into the mechanism of Wnt signal transduction arose from early studies of several mutants in *Drosophila*. In *Drosophila*, *wingless* mutations can cause wings to transform to a notum or disrupt segment polarity in larvae (Nusslein-Volhard and Wieschaus, 1980). *porcupine*, *dishevelled*, *armadillo* (*Drosophila* homolog of B-catenin) and *pangolin* (*Drosophila* homolog of *Tcf*) display segment polarity like *wingless* (Nusslein-Volhard and Wieschaus, 1980, Wieschaus and Riggleman, 1987). These genes have been ordered in a genetic pathway to understand the intercellular signalling during *Drosophila* embryogenesis (Noordermeer et al., 1994). Since then a wealth of research has augmented the study of Wnt signal transduction and its importance in regulating numerous developmental pathways.

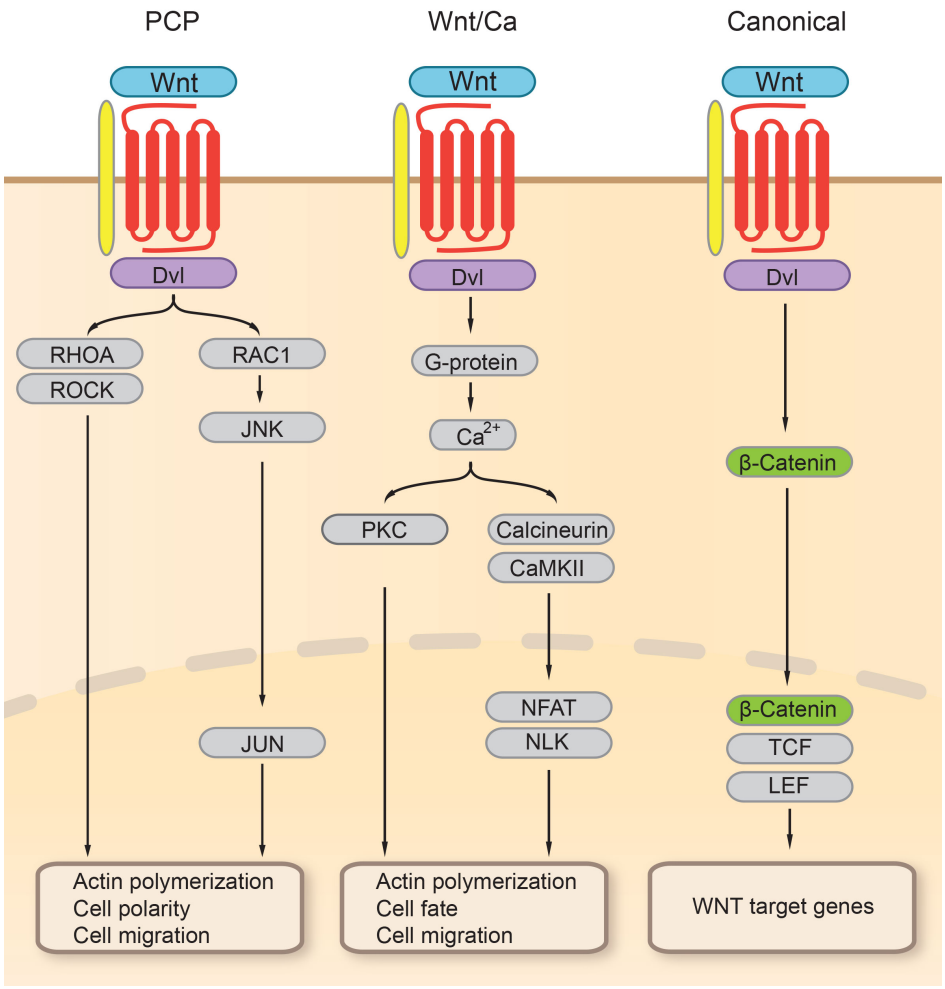

Figure 6. Summary of Wnt signalling pathways.

The two non-canonical pathways (PCP and Calcium) are on the left while the β-catenin pathway is on the right. The red transmembrane receptor represents frizzled alongside LRP5 or LRP6 ligand. The dotted line represents the cell nuclear membrane. Once the Wnt/PCP pathway is activated, it triggers a small G-protein (guanine nucleotide binding proteins that acts as molecular switches), Rho (RHOA) to activate ROCK which is implicated in regulating cellular cytoskeleton. The Wnt/PCP pathway also acts through RAC1 to mediate actin polymerization via JNK activation. The Wnt/Ca^{2+}pathway also acts through a G-protein to influence calcium intracellular movements from the endoplasmic reticulum which increases the concentration of calcium and thereby activating the Protein Kinase C (PKC) pathway. It also activates calcineurin and calmodulin-dependent protein kinase II (CaMKII) to induce activation of nuclear factor of activated T-cells) NFAT that is also implicated in actin polymerization, cell fate and migration. The canonical Wnt pathway acts through β-catenin to activate the TCF/LEF complex and turning on of downstream WNT target genes (Adapted from (Nusse, 2015).

To date, there are two main Wnt signalling pathways described and characterized; the canonical and non-canonical (summarized in **Figure 6**). In the canonical pathway, Wnt proteins (that includes WNT1, WNT3, WNT3A, WNT8 or WNT10B) bind to members of the Frizzled family on cell surfaces. This activates and stabilize β-catenin by releasing it

from the Axin-GSK3-APC-complex (APC = adenomatour polyposis coli). The stabilized β-catenin is then able to translocate to the nucleus and interact with T-cell factor/lymphoid enhancer factor (TCF/LEF) transcription factors. In turn, this proteic complex activates several downstream genes and controls programs regulating cell fate and morphogenesis (van Amerongen and Nusse, 2009). On the non-canonical side, two separate pathways can be activated by Wnt (that includes WNT4, WNT5A, WNT5B, WNT6, WNT7B, WNT9a, WNT11 and WNT16). They can activate two separate non-canonical pathways; one that regulates planar cell polarity (PCP) to stimulate cytoskeletal reorganization through the activation of small GTPases (Rho and Rac), also called the Wnt/PCP pathway and the Wnt/Ca^{2+} pathway that regulates calcium mobilization from intracellular stores through heterotrimeric G-proteins (Veeman et al., 2003). Researchers are still discovering new roles and functions of both of these pathways and even cross-talks (Nusse, 2015).

1.6.1. The canonical Wnt/B-catenin signalling in skeletogenesis

The first evidence of the role of the canonical Wnt signalling in osteogenesis came from studies of human and mouse mutations in the low-density lipoprotein receptor-related protein 5 (*LRP5*) which causes an increase in bone mass (in activating mutations) (Boyden et al., 2002) or decreased bone mass as in osteoporosis pseudoglioma syndrome (null mutations) (Gong et al., 2001). LRPs are co-receptors for Wnt ligands together with transmembrane receptors of the Frizzled (FZD) family. When Wnt binds to the LRP/FZD complex, it triggers a series of downstream events via the β-catenin/LEF/TCF pathway and induces expression of major osteochondrogenic factors such as *Runx2* (Gaur et al., 2005), Osteoprotegerin (*OPG*) (Glass et al., 2005) and *RANKL* (Takahashi et al., 2011) to regulate bone homeostasis and mass.

Apart from homeostasis, the canonical Wnt pathway plays a role in osteoblast specification. This role has been demonstrated in mouse by conditional inactivation of β-catenin in a *Prx1*-cre line. In this model, the head and limb mesenchyme failed dramatically to develop bone. Further characterization revealed that this defect may be due to progenitor cells failing to express *Osterix* (also called *sp7*), a critical transcription factor required for osteoblast differentiation (Hill et al., 2005). Other studies conditionally knocking out β-catenin in the condensing mesenchyme also showed an arrest in osteoblast development (Day et al., 2005). Transcriptional analysis using chromatin immunoprecipitation (ChIP) assays revealed direct binding of TCF1 to *Runx2* promoter

(another key transcription factor required during early osteoblast progenitor differentiation), suggesting that the canonical WNT signalling pathway directly regulates *Runx2* to control osteoblast differentiation (Gaur et al., 2005). Like many aspects of development, the Wnt/β-catenin pathway does not act in solitude during skeletogenesis. As uncovered in many published works, its activity can be restricted by several other factors including BMP signalling (Kamiya et al., 2008), Notch overexpression (Deregowski et al., 2006), or Sox9 (Topol et al., 2009).

From an evolutionary perspective, varying levels of Wnt signalling activity play an important role as a mediator of craniofacial form and plasticity by determining the roundness of the upper jaw as well as exaggeration to jaw protrusion to influence foraging and feeding (Concannon and Albertson, 2015, Parsons et al., 2014). As most of craniofacial bones are NCC derived, the canonical Wnt signalling is also essential in NCC development and differentiation (Lewis et al., 2004, Willems et al., 2015). Alterations in components of the Wnt/β-catenin pathway can directly affect trophic skeletogenesis, including development of the maxilla and mandible as well as tooth development (Ahn et al., 2010, Curtin et al., 2011, Dougherty et al., 2013, Kawakami et al., 2014, Willems et al., 2015). Previous work done in our lab showed that transcriptionally knocking down *wnt9a* affects development of both upper and lower jaw elements (Curtin et al., 2011). *wnt9a* isoform, *wnt9b* also controls the development of anterior skeletal structures and promotes dorsoventral patterning (Jezewski et al., 2008). Studies in zebrafish by another group showed that in addition to regulating bone mass, *lrp5* plays a role in CNCC migration where transient knockdown experiments showed reduced proliferation of premigratory CNCC and thereby abnormal or absent ventral cartilage structures (Willems et al., 2015). In Lake Malawi cichlids, another aquatic model organism, expanded Wnt/β-catenin activity and increased *lef1* expression in preorbital skeletal elements showed increased bony mineralization due to accelerated bone development (Parsons et al., 2014).

1.6.2. The non-canonical Wnt signaling pathway in skeletogenesis

Non-canonical Wnts have been shown to act via the β-catenin-independent pathway to activate the planar cell polarity (PCP) or Wnt/Ca^{2+} signalling (Veeman et al., 2003). Non-canonical Wnts, Wnt/PCP and Wnt/Ca^{2+} controls aspects of gastrulation movements by driving mediolateral convergence and antero-posterior extension (termed convergent extension, CE) of the body axis, notably of presumptive notochord cells, organogenesis

and even of the palate and trophic cartilage structures (Rochard et al., 2016, Wallingford et al., 2002, Tada and Smith, 2000) as well as planar cell polarity as in mouse cochlea (Curtin et al., 2003, Wang et al., 2005). Despite the number of studies, the role of the non-canonical pathway affecting bone homeostasis is still less understood.

Early developmental studies in mice showed that Wnt7b acting through the Wnt-G protein linked PKCδ cascade promotes osteoblast differentiation (Tu et al., 2007). In another study, Wnt5a was shown to bind to Ror2 (a single pass receptor) and Frizzled receptors to enhance RANKL-dependent osteoclast differentiation and bone resorption. Interestingly, the lack of only one copy of *Wnt5a* in mice (as demonstrated in *Wnt5a*+/- mice) is sufficient to result in an osteopenic phenotype with reduced bone formation and resorption (Maeda et al., 2012). Maeda and colleagues also showed that *Wnt5a* acts in a non-cell autonomous manner, being secreted from osteoblast to regulate osteoclastogenesis. During chondrogenesis, studies performed in chick revealed that ectopic *Wnt5a* delays chondrocyte differentiation while *Wnt4* promoted differentiation (Hartmann and Tabin, 2000). In mice *Wnt5a* and *Wnt5b* were shown to regulate chondrocyte proliferation, thus affecting acral long bone skeletal development (Yang et al., 2003). Studies employing zebrafish to explore non-canonical functions of Wnts also revealed key roles in early pharyngeal pouch development and late craniofacial patterning (Curtin et al., 2011, Choe et al., 2013, Heisenberg et al., 2000, Sisson et al., 2015). However, how chondrocyte organization affects craniofacial bone development, especially during endochondral ossification remains to be understood.

1.6.3. Wnt secretion in skeletogenesis

Recently, genome-wide association studies have identified two SNPs (single nucleotide polymorphism) strongly associated with reduced bone mass that lie within the intron of human *GPR177* gene (also known as *Wntless*, *WLS*) (Rivadeneira et al., 2009). Wls, a multispan transmembrane protein is conserved from *C. elegans* to mammals and has been shown to be key in the secretion of Wnt ligands by binding and accompanying Wnt to the cell surface (Banziger et al., 2006, Port et al., 2008). Wnt trafficking and secretion has been an area of interest in different fields including development. Despite Wnts being hydrophobic proteins, they can travel long distances to induce cell-type specific responses. Evidence have shown that some Wnt proteins can be packaged onto extracellular carriers such as exosomes to reach the receiving cell (Gross and Boutros, 2013). Therefore, to

achieve its paracrine effects, trafficking of Wnt from its origin cell to the recipient cell must be tightly regulated. Newly synthesized Wnts are directed to the lumen of the endoplasmic reticulum (ER) where they are palmitoleated by the ER-resident membrane-bound O-acyltransferase Porcupine (PORCN) for Wnts to be able to bind to Wls (Coombs et al., 2010). Wnt-WLS complex are then transported in coatomer (COP) cargos from the endoplasmic reticulum to the Golgi complex and then towards the plasma membrane (Yu et al., 2014, Zhang et al., 2016). As the secretory COP cargos reach the cell surface, Wnts are released from WLS. From here, Frzb (long-range) and Glypican (a class of heparan sulfate proteoglycans that act short-range) proteins facilitate Wnt diffusion to the receiving cells (Zecca et al., 1996). Unloaded WLS is then recycled back to the trans-Golgi network to bind further synthesized Wnts (Belenkaya et al., 2008). Wls secretion is summarized in **Figure 7**.

Considering the major role of Wls in Wnt signalling, dramatic effects of its mutation can be expected. Disruption in *WLS* locus has been associated with changes in human bone mineral density that has implications for diseases such as osteoporosis (Rivadeneira et al., 2009). *Wls* -/- mice results in embryonic lethality while mesenchymal deletion resulted in arrested limb growth and ectodermal loss leading to agenesis of distal limb tissue (Zhu et al., 2012). Osteoblast specific *Wls* deletion in mice resulted in dramatic reduction in cortical bone mass due to defective differentiation and mineralization (Zhu et al., 2012). Further studies using both chondrocyte and osteoblast specific conditional inactivation led to impairment of intramembranous and endochondral ossification by modulating cell proliferation and differentiation (Maruyama et al., 2013). In our lab, previous studies have showed that *wls* is required for convergence extension mechanism of the zebrafish ethmoid plate, a homologous structure to the human primary palate, due to defects in chondrocyte elongation and intercalation (Rochard et al., 2016).

Altogether, these studies have highlighted the important role of Wnt signalling in the crosstalk between different cell populations during development (Gross and Boutros, 2013). In this thesis, *wls* is studied in two contexts; its role in lower jaw development and in another chapter, neural crest cell development.

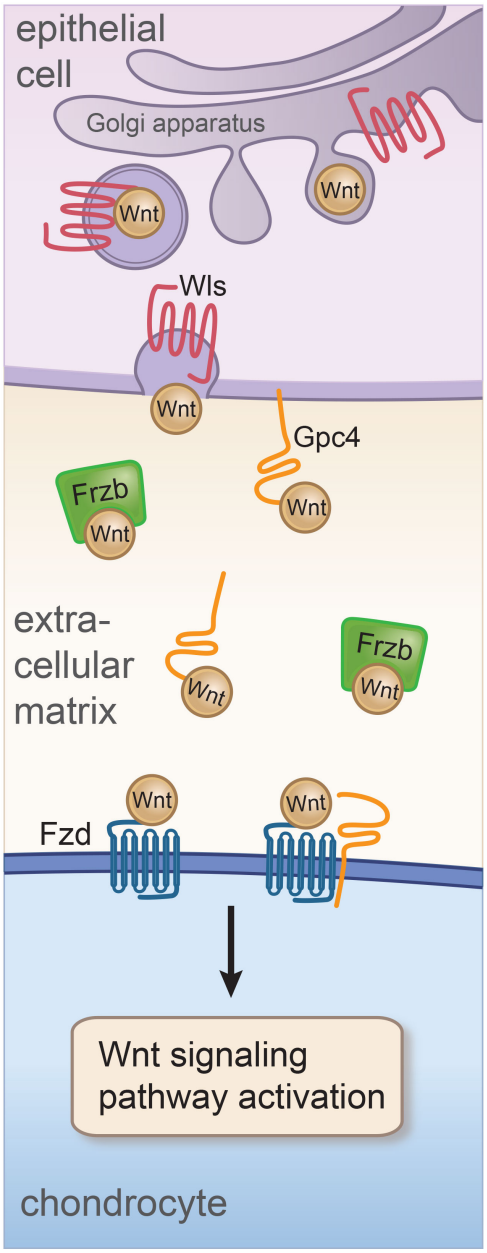

Figure 7. Wnt trafficking following synthesis and palmitoleation within the endoplasmic reticulum. Wnt binds to Wls and is transported in COP cargos from the golgi complex to the cell surface where it is released and diffuses across extracellular matrix with the aid of Frzb (long range) and gpc4 (short range). Once it reaches its target cell, it binds to Fzd receptors to activate downstream signalling effects.

1.7. Thesis aims and hypotheses

1. Understand how the underlying trophic cartilage anlages affect endochondral bone formation and how non-canonical Wnt signalling affect shaping and patterning of trophic craniofacial structure.

    a. Hypothesis: We hypothesize that the cartilage provides a scaffold for bone development and proper shaping and size of this anlage is required for adequate mandibular development.

2. Develop a model to understand dynamic chondrocyte behaviour during craniofacial development by utilizing a multispectral zebrabow transgenic line

    a. Hypothesis: The zebrabow line allows individual colouring of the cells thus enabling us to track cellular behaviour over time to allow us to see how cartilage stack and dynamically interact with each other.

3. Understand how *wls* trafficking via *cop* mechanism affect neural crest development

    a. Hypothesis: We hypothesize that cop will be spatiotemporally expressed during development, with increasing expression in tissues with high metabolic activity to shuttle proteins for growth and development. As wls is known to be shuttled by cop, we predict that defects within the cop mechanism will display severe craniofacial defects.

Chapter 2: Material and methods

2.1 Animals

2.1.1. Zebrafish lines

Zebrafish (*Danio rerio*) were maintained at 28°C on a 14:10 light:dark cycle (Westerfield, 1995). Fertilized eggs were obtained following set up in breeding tanks and grown in incubators set at 28.5°C, left at RT; approximately 22°C (to slow development) or 31°C (to accelerate development). Embryos were then staged according to standard references in the US and agreed by the Institutional Animal Care and Use Committee (IACUC) (Kimmel et al., 1995). Embryos were generated from WT Tübingen. Mutant lines (*gpc4*$^{hi1688Tg/+}$, *wnt5b*$^{hi2735bTg/+}$) were obtained from ZIRC. *wls*$^{c186/+}$ was provided and previously characterized by Marnie Halpern (John Hopkins University) (Kuan et al., 2015) *copa*^{hi1872Tg} was provided by Sun Zhaoxia (Yale University). One of the two previously generated CRISPR *wnt9a* mutant line (Rochard et al., 2016) with the following target sequence TGTCCATTCTGCCACTGACC and harboring a -4bp deletion (allele c.114_117del) was used for this study. The other line with a 13 bp deletion was used as a control and displayed a similar phenotype, allowing validation of the first mutant line. We used the transgenic line Tg(*sox10*:GFP), Tg(*sox10*:mCherry), Tg(*osteocalcin*:GFP) (Singh et al., 2012), Tg(*osterix*:RFP-NTR) (Singh et al., 2012), Tg(*sox10*:creERT2) and Tg(*ubi*:zebrabow). The following transgenic lines were generated using Gateway cloning: Tg(*ubi*:*copa*), Tg(*cmlc2*:GFP,U6:gRNA *copa*, *sox10*:Cas9).

2.1.2. Genotyping

Zebrafish tails were cut and DNA extracted using alkaline lysis method. 100 µL of 5mM NaOH was added and boiled with the tail clip for at least 30 minutes. 25 µL (1:4 ratio) of Tris pH 8.0 was added and vortex for at least 30 seconds to pellet remaining debris. DNA stored at -20°C. 1µL of adult fish DNA was used in a 10 µL PCR reaction for genotyping and run on a 1% TE agarose gel. For preparation of genomic DNA from embryos, a similar protocol was use as above but quantity of NaOH is adjusted per the size of the embryo. Primers for genotyping fish-lines used in this study are listed below:

Table 1. Genotyping primers

Gene	Sequence (5' – 3')	Tm
***c186* fwd**	gactgagaggaaccgctttcagtgttct	58°C
***c186* rev**	agaaaggattctttagctgtactcctctgc	
***wnt9a* FAM Fwd**	agattccaatggctgcgcccacttg	60°C
***wnt9a* Rev**	gagagatggaactgcacgctggagg	
***wnt5b* Fwd**	gggtctattcatcttcttgcctttg	62°C
***wnt5b* rev**	tcgcttctcgcttctgttcg	
***gpc4* Fwd**	ccttgatctgaacttctctattctcag	60°C
***gpc4* rev**	aagagggctaataattgcggac	
***copa* 1872C1 Fwd**	gacgtggagcttgcgatgctg	60°C
***copa* rev2**	ctgtgtggtgtatttcttgaggcc	
***copa* MSL4 rev**	gctagcttgccaaacctacag	

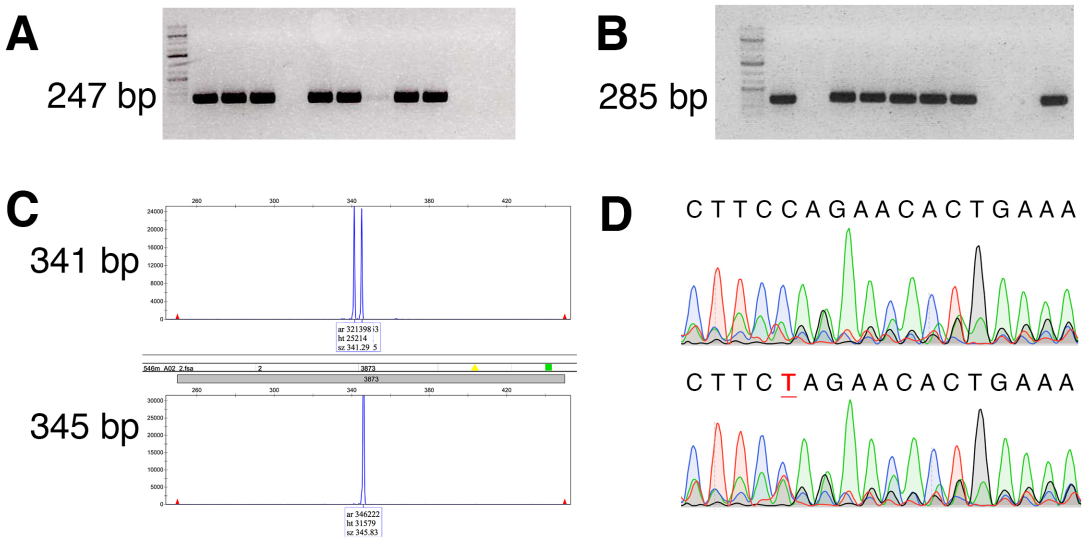

Figure 8. Genotyping of Wnt mutants.

A. *wnt5b hi2735bTg* genotyping. The 247 bp product is specific for the mutant gDNA while no product is generated for wild-type gDNA, as in lanes 5 and 8.

B. *kny hi1688Tg* genotyping. The 285 bp product is specific for the mutant gDNA while no product is generated for wild-type gDNA as in lanes 2, 8 and 9.

C. *wnt9a* CRISPR mutant 6-FAM microsatellite assay showing a 341 bp mutant allele peak and a 345 bp wild-type peak. Two peaks represent a heterozygote embryo.

D. dCAPS assay for *c186* (*wls*). I found the dCAPS digest often did not offer clean bands when ran on a 1.5% agorose gel at low voltage. Therefore, I often sequenced the PCR product using the reverse genotyping primer which shows the C > T mutation (as indicated by the bold red T nucleotide in the bottom image (heterozygote as there is equal intensity of both the T and C nucleotide, compared to the WT).

2.1.2.1. Derived cleaved amplified polymorphic sequence (dCAPS) assay

Genotyping of *c186* allele (*wntless*) was performed using dCAPS assay (Kuan et al., 2015). In this assay, a restriction enzyme recognition site that includes the single nucleotide polymorphism (SNP) is introduced into the PCR product by a primer containing one or more mismatches to the template DNA. The PCR product modified in this manner is then subjected to the restriction enzyme digestion and the presence of absence of the SNP is determined by the resulting restriction pattern and bands compared on a 1% agarose gel. Here, genomic DNA for *c186* allele was PCR amplified using the primers noted in Table 1.

The forward primer contains a mismatch, generating a DNA fragment that is sensitive to XbaI disgestion in the *c186* allele but not in WT. Following XbaI digestion at 37°C overnight, the PCR product can be readily visualized on a 1% agarose gel with a running time of 2 hours to adequately separate out the smaller DNA fragment (Kuan et al., 2015).

Complement to the dCAPS assay for *c186* genotyping, PCR products were at times sent for sequencing using the reverse primer and sequences analysed for the point mutation.

2.1.2.2. Microsatellite DNA fragment analysis

Gene editing by CRISPR-Cas9 methodology created indels in the coding region of our genes of interest. We used the size variations to design genotyping primers. Forward primers were fluorescent dye-labelled with 6-carboxyfluorescein (6-FAM) and labelled DNA fragments were electrophoretically separated using an ABI3730xl Genetic Analyser (available at the MGH Centre for Computational and Integrative Biology Core Facility).

2.1.3. Embryo collection

Zebrafish (*Danio rerio*) female and male pairs are set up in breeding tanks and kept physically separated in the same tank and released when eggs were required the following morning. Embryos were collected in Egg Water (also known as E3) (5.0mM NaCL, 0.17mM KCl, 0.33mM $CaCl_2$, 0.33mM $MgSO_4$ with 0.05% Methylene Blue (as an anti-fungal)) shortly after having been laid. Embryos are then kept in a 28.5°C incubator and E3 changed the following day and dead embryos cleared. Embryos were then either

collected for experimentation or placed in the main zebrafish system after 5 days in a 28.5°C incubator.

For collection, zebrafish embryos were staged according to the morphological criteria (Kimmel et al., 1995), tricaine treated and subsequently fixed at least overnight in 4% PFA in phosphate buffered saline (PBS) at 4°C. Embryos younger than 48hpf were de-chorionated with a short chemical treatment of pronase prior to fixation or by mechanical treatment using forceps. Following fixation, embryos were dehydrated in MeOH/1X PBST graduations (25%, 50%, 100%). Dehydrated embryos were then stored in 100% methanol at -20°C until required. Where bleaching is necessary, prior to dehydration, embryos were incubated in 1.5% H_2O_2/1.5% KOH until pigmentations were cleared, then surfixed in 4% PFA for at least 20 minutes, then dehydrated and stored in 100% MeOH at -20°C.

2.2 General molecular biology techniques

2.2.1. Bacterial Plasmid DNA preparation

The Qiagen Miniprep kit was used for all small-scale plasmid preparations, according to manufacturer's protocol. DNA was then quantified by spectrophotometry (NanoDrop) at 260 nm following calibration with diluent used to elute the DNA. The ratio between 260nm and 280nm provided an estimate of the purity of the nucleic acid preparation (DNA preparations should ideally have a OD_{260}/OD_{280} values of around 1.8 and 2.0)

2.2.2. Gel extraction of DNA

The appropriate band from a DNA agarose gel run was excised under UV light (with appropriate eye protective wear) and DNA extracted using the QIAquick Gel Extraction Kit (Qiagen) according to manufacturer's protocol. Samples were eluted in 30µL EB buffer or water and DNA quantified by spectrophotometry. Typically, 1µg of DNA is used for further ligation reactions.

2.2.3. Restriction digestions

Restriction enzyme digestions were performed at 37°C for at least 2 hours using commercially available restriction enzymes and buffers (New England Biolabs). At least 1µg/mL of bacterial plasmid was used per 50µL reaction. For double digestion, the

appropriate buffers were used as suggested by the manufacturer. Following digestions, reactions were typically column purified, eluted with 20-30µL ddH2O or TE buffer then run 1-2µL on agarose gel to ensure complete and correct product size.

2.2.4. Ligation reactions

Intermolecular ligations were performed in small volumes, typically using 1:3 ratio of DNA insert to linearized bacterial plasmid of choice (expression or non-expression). Usually 20µL for approximately 20ng of vector DNA with 60ng of insert DNA is used. Ligation reactions are carried out overnight at 4°C with T4 DNA ligase (NEB Biolabs) with T4 DNA ligase buffer (NEB Biolabs). Sticky end ligation was performed either using enzymes giving compatible ends or primer-engineered restriction enzyme sites on the ends of PCR amplified DNA. Ligated plasmids were then ready for transformation into chemically competent bacteria or stored at -20°C until use.

2.2.5. Transformation of chemically competent bacteria

For plasmid transformation, ligated DNA or PCR generated DNA fragment was added into thawed competent TOP10 cells, Invitrogen (or using lab stock competent cells) followed by 30 minutes incubation on ice. Typically, 2-5µL of ligation mix was added to 50µL of cells. The cells were then subjected to a 30 second heat shock at 42°C (to allow DNA fragments to enter the cell) and immediately put on ice thereafter. For kanamycin or chloramphenicol resistant competent cells, 250µL of LB (or SOC media) was added and incubated for 1 hour at 37°C followed by plating on the appropriate antibiotic-containing LB agar plates and plates were incubated overnight at 37°C. For pGEM-T easy cloning, 20µL of X-Gal and 40µL of IPTG was used to aid selection of positive colonies. Direction of insertion was then tested by DNA sequencing.

2.2.6. DNA sequencing

For bacterial plasmid sequencing, DNA solutions were sent to MGH DNA Core facility with an aliquot of appropriate primers for sequencing and concentrations per the core facility sequencing guidelines.

2.2.7. Polymerase Chain Reaction (PCR)

PCR reactions were carried out per standard protocols using Eppendorf PCR Thermal Cycler Machines. Taq-DNA polymerase, Promega was used for most molecular characterizations. Platinum Taq DNA polymerase, Thermo Fisher Scientific or Phusion® High Fidelity DNA polymerase, New England Biolabs was used for amplifying sequences to be cloned into expression vectors or for RNA injection studies due to low error copying rate. For templates with high GC content, the addition of DMSO and GC buffer were used with the Phusion® High Fidelity DNA polymerase. Annealing temperatures specific to individual primer pairs were calculated using NEB Tm Calculator (http://tmcalculator.neb.com) and optimized.

Table 2. Standard PCR mix

Component	Volume
2X GoTaq Polymerase	5µl
ddH2O	5µl
Forward primer	0.25µl
Reverse primer	0.25µl
DNA template	0.5 – 1µl
Total	11 – 11.5µl

2.2.8. Tol2kit multisite Gateway cloning

The Gateway® Technology is based on the *att* site-specific recombination system from lambda phage that allows efficient transfer of DNA constructs between plasmids (Hartley, 2003, Walhout et al., 2000). We used the three-insert multisite Gateway system (Invitrogen) that combines three "entry" vectors (p5E, pME and p3E) into a "destination" vector (pDEST).

2.2.8.1. 5' Entry Clone

5' Entry Clone used in this study includes p5E-*ubi:loxP-EGFP-loxP-mCherry (ubi:Switch)* obtained from the Zon lab and p5E-*sox10* generated in our laboratory which contains a 7.2kb region upstream of the zebrafish *sox10*.

2.2.8.2. Middle Entry Clone

Middle Entry clone contains full-length *copa* cDNA. *copa* was PCR amplified with a 4bp Kozak sequence on the 5' end of the forward primer. The following primer sequences used are as follows:

Forward: 5' – **CACC**ATGTTGACCAAATTTGAGACAAAGTCGGCCCG - 3'
Reverse: 5' – AGTCCACTGCAGTTCCGCTGA – 3'
Start and stop codons of *copa* underlined, Kozak sequence in **bold.**

Following PCR amplification, blunt-end PCR product is run on a 1% gel agarose gel to check the integrity and size of the DNA fragment. Subsequently, the following TOPO cloning ligation reaction was set up using a 2:1 molar ratio of PCR product:TOPO vector:

Table 3. TOPO ligation reaction mix

Component	Volume
Fresh PCR product	2μl
Salt solution (provided)	1μl
TOPO vector	1μl
ddH2O	2μl
Total	6μl

The mixture was incubated for 5 mins at RT and preceded to transformation in One Shot chemically competent cells. These were then plated on a kanamycin treated LB plate and incubated overnight at 37°C. The following day, multiple clones were selected and colony PCR performed to identify clones with the insert. For clones that contained the insert, a larger bacterial preparation typically 100-200mLs of LB was set up and subsequent extracted plasmid DNA was sent for DNA sequencing to check for correct sequence insertion using a M13 forward (-20) and M13 reverse primers:

M13 Forward (-20): 5' – GTAAAACGACGGCCAG-3'
M13 Reverse 5' – CAGGAAACAGCTATGAC – 3'

2.2.8.3. 3' Entry clone

3' Entry clone contained a polyadenylation signal, p3E-polyA that comprises the SV40 late polyadenylation signal sequence derived from pCS2+.

2.2.8.4. Destination vector

We used Tol2-based destination vectors to provide the Tol2 transposon ends needed for transposition. The destination vector used has an extra marker cassette featuring the crystalline promoter (*α-crystallin*:mCherry). This vector (pDESTTol2-*α-crystallin*:mCherry) allowed transgenesis with a fluorescent red eye that enabled subsequent scoring and line maintenance by tracking the bright eye expression.

2.2.8.5. LR Recombination reaction

Invitrogen Gateway™ LR Clonase™ II enzyme mix and buffer was used. The LR Clonase enzyme contained the bacteriophage lambda proteins Integrase and Excisionase to catalyze *in vitro* recombination between entry clones with attL-flanked gene and an attR-containing destination vector to generate an attB containing expression clone. The p5E contains attL4 and attR1 sites, pME contain attL1 and attL2 sites, p3E contain attR2 and attL3 sites and the pDestTol2pA contains attR4 and attR3 sites. This is to allow LR reaction by recombination with attL1-attR1, attL2-attR2, attL3-attR3 and attL4-attR4. Once pENTR and pDEST constructs were assembled, MIDI preparations were done, plasmid sequences checked and DNA concentrations measured using the NanoDrop. The amount of DNA needed for each pENTR clone was calculated using the formula below:

$ng = (fmol)(N)(\frac{660\,fg}{fmol})(\frac{1\,ng}{10^6})$. N = size of DNA in bp (i.e. length of plasmid)

A mastermix was made for each ENTR clone (i.e. 1µl containing 10fmol) and 200fmol in 10µl for the pDEST (i.e. 1µl containing 20fmol).

Table 4. Gateway reaction mix

Component	Volume
P5E	1µl (10fmol)
pME	1µl (10fmol)
P3E	1µl (10fmol)
pDEST	1µl (20fmol)
TE buffer pH 8.0	4µl
Total	8µl

LR clonase enzyme was thawed on ice for about 2 minutes, briefly vortex and 2µl was added to the ENTR/DEST mixture and allowed to incubate at RT for 1 hour. 1µl of Proteinase K solution (provided in the kit) was then added to the sample and incubated at 37°C for 10 minutes to stop the clonase reaction. 2µl of the mix was then transformed into Top 10 competent cells and plated on LB plates with ampicillin. Colonies were picked and colony PCR set up using primers specific to the p5E, pME and p3E. Positive colonies were then sent for full plasmid sequencing to ensure correct inserts, orientation and no mutations within the pME. Midi preparations of positive pDestTol2-(promoter)-(gene)-pA-α-crystallin:RFP were set up, DNA concentration measured and stored at -20°C. An example of one of the final plasmid maps used in this thesis is shown in **Figure 9**.

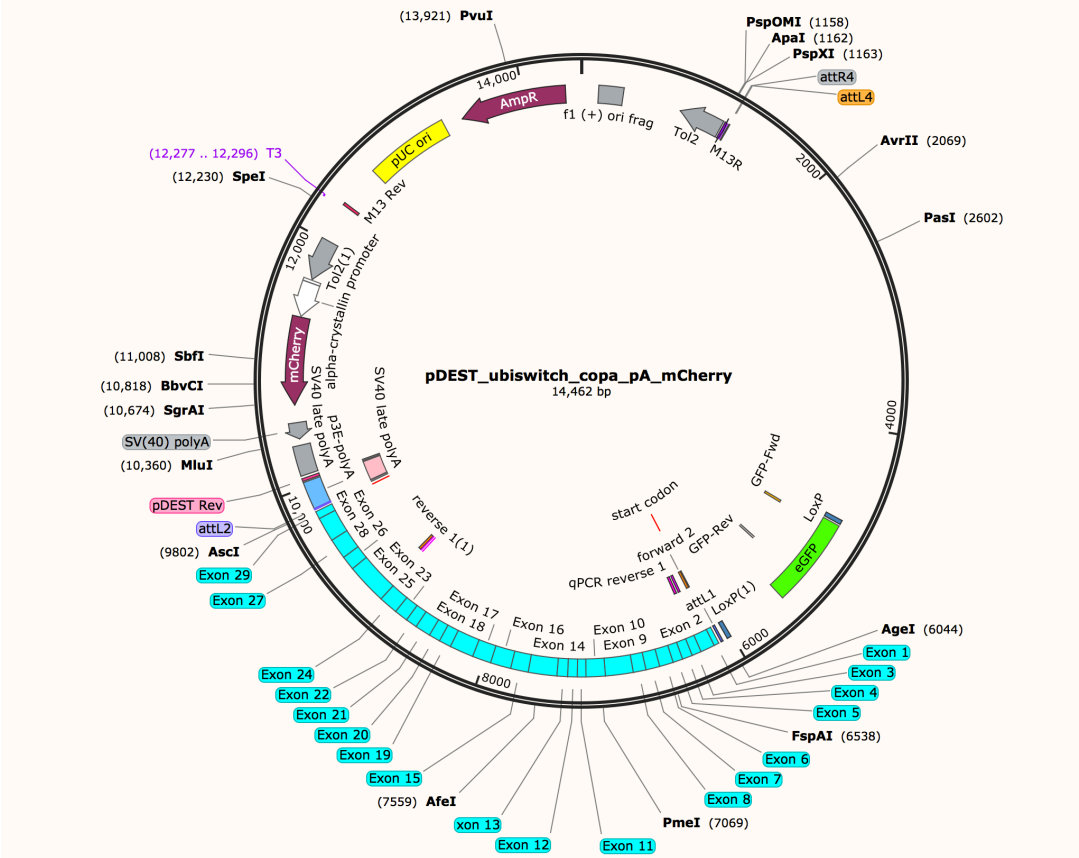

Figure 9. Plasmid map of pDEST-ubiswitch-copa-pA.

Final plasmid sequence map (generated using SnapGene program) following LR recombination using *ubi*:switch as p5E, *copa* mRNA as the pME and a poly-A as p3E into a pDEST containing an α-crystallin promoter driving mCherry expression.

2.2.8.6. Tol2 transposase RNA synthesis

Transposase RNA was generated using the pCS2FA-transposase plasmid (Addgene). 1µg of Plasmid DNA was linearized with Not1 in a 50µl reaction and purified using the Qiagen

PCR Purification kit. Capped RNA synthesis was done using the mMessage mMachine Sp6 kit (Ambion) according to manufacturer's instructions. RNA was then purified with the Qiagen RNeasy Mini Kit and ethanol precipitated. Capped RNA was stored at -80°C.

2.2.9. Injection and generation of transgenic lines

Zebrafish pairs were set up in breeding tanks the previous evening and separated with a divider. The following morning, dividers were pulled and eggs collected approximately 15 mins after spawning and embryos were then placed in a cooled agarose tray with depression to align embryos. Embryos at the 1 cell stage were then aligned in a plastic trough, with their chorions intact. 100ng/µl of purified construct vector (20-30pg) was co-injected with 50ng/µl of Tol2 transposase mRNA (20pg) directly into the cytoplasm (blastomere) of the cell. At least 100 embryos were injected with the construct using a borosilicate glass needle (O.D. 1.0mm, I.D. 0.5mm; Sutter) pulled with a Flaming/Brown Micropipette Puller, Model P-97 and injected using a PLI-90A Pico-Liter Injector (Harvard Apparatus). The injected embryos were left to develop at 28.5°C. Injected embryos are then transferred to petri dishes, washed with E3 water and allowed to develop in a 28.5°C incubator.

Positive transgenic embryos (F0) were selected (based on the expression of the α-crystallin transgenesis marker), raised to adulthood and subsequently outcrossed to Tubingen lines to generate F1 with germline transmission. Positive F1 embryos were further selected and raised to adulthood.

For mRNA rescue experiments, a similar protocol is carried out with a few variations. Different concentrations of mRNA were optimized to obtain a suitable dose for study and minimize toxicity effects. Common non-specific effects of toxicity includes cell death (usually in the brain) and developmental delay (Ekker and Larson, 2001). Additionally, 300 pg of nontoxic injection solution such as GFP-encoding RNA is injected in conjunction with the mRNA of interest to monitor the injection success. Yolk injections rather than blastomere-targeted injections for mRNA rescues resulted in fewer toxic side effects and did not alter the zebrafish development (Ekker and Larson, 2001).

2.2.10. Quantitative reverse transcriptase polymerase chain reaction (qPCR)

2.2.10.1. RNA extraction

This protocol describes the extraction of RNA from a pool of embryos. Adjusting the volume of reagents appropriately allows for single embryo extraction. Following tricaine-treatment, 50-100 embryos were thoroughly washed with 1X PBS and transferred to a fresh 1.5ml microcentrifuge tube. 1ml of Trizol® (Invitrogen) was added and embryos homogenized using either a hand-held homogenizer with an attached plastic rod or using a 20G needle and syringe by pipetting until the embryo is fully dissociated. Trizol® is a monophasic solution of phenol and guanidine isothiocyanate that enables isolation of RNA, DNA and proteins from cells and tissue samples. 200µl of chloroform was then added and the tube shaken vigorously for 15 seconds and incubated at RT for 3-5 minutes (until layers start to appear). The tube was then centrifuged at 12,000 rpm for 15 minutes at 4°C. The chloroform results in the separation of the aqueous and organic phases of the Trizol mixture with the RNA being held in the upper aqueous layer. The supernatant (upper) layer was then transferred into a fresh RNAse-free tube, precipitated by adding 70% ethanol and left on ice for at least 10 minutes (or in certain circumstances, overnight at -80°C.

To obtain clean RNA, an additional RNA clean up step was performed using a Qiagen RNAeasy MinElute Cleanup Kit (Cat 74204). The precipitated sample (approximately 700µl) was then aliquoted into the spin column (Qiagen) available in the kit and centrifuged for 15 seconds at 8000xg. 700µl of wash buffer (Qiagen) was added to the column and centrifuged for 15 seconds at 8000xg. An additional DNAse step was performed. Following the wash buffer, 80µl of DNAse I solution (79254, Qiagen) was added to the column and incubated for 20 minutes at RT. A further 350µl of wash buffer (Qiagen) was performed and columns centrifuged at 8000xg. 500µl of 70% ethanol wash (Qiagen) was then added and centrifuged again at 15 seconds at 8000xg and repeated with an additional 500µl of 70% ethanol wash buffer and 2 minutes centrifugation. Centrifuging for 1 minute at maximum speed then dried the membrane. Elute RNA with 30µl RNAse DNAse free H_2O, incubate for 1 minute and spin at 8000xg for 1 minute into a fresh new 1.5ml RNAse free microcentrifuge tube. The sample was then quantified on a Nanodrop®. Only samples with a reading of approximately 1.8-2.0 (260/280 absorbance) and approximately 2.0-2.2 (260/230) were considered of quality. For further analysis, 1µl of

sample was sent to the bioanalyzer (Harvard University molecular biology core facility) for quality of the RNA obtained (aiming for a RNA Integrity Number of at least 8.0 for qPCR quality samples). RNA was then stored at -80°C.

2.2.10.2. cDNA synthesis

cDNA synthesis was performed using the iScript™ Select cDNA Synthesis Kit (BioRad 170-8896) according to manufacturer's protocol. In short, 4µl of 5X iScript reaction mix was added with 2µl of Oligo(dT)$_{20}$ primer or random primer, 1µl of iScript reverse trancriptase, at least 1µg equivalent volume of RNA and made up to 20µl with nuclease-free water. For qPCR reaction, random primers were used for synthesis. The tube was then incubated for 5 minutes at 25°C, then 30 minutes at 42°C. Finally, the reaction was stopped by incubating at 85°C for 5 minutes to heat-inactivate the reverse transcriptase. The cDNA products were then stored at -20°C, ready for qPCR analysis.

2.2.10.3. qPCR reaction

qPCR reactions were performed using the PowerUp™ SYBR™ Green Master Mix (applied biosystems A25741). 5µl of the 2X PowerUp SYBR Green Master Mix was added to 1µl of forward and reverse primers, at least 1µg of cDNA template and made up to 10µl with nuclease-free water. Triplicates were performed for each reaction with a no template control to help identify PCR contamination. The reactions were transferred to a 96-well optical plate, sealed with an optical adhesive cover and centrifuge briefly to spin down the contents and eliminate any air bubbles. The plate was then placed in the real-time PCR machine (Applied Biosystems StepOne™ Real-Time PCR system) and ran using the StepOne Software. Standard cycling mode was selected using the following program:

Table 5. qPCR program

Step	Temp	Duration	Cycles
UDG activation	50°C	2 minutes	Hold
Dual-Lock DNA polymerase	95°C	2 minutes	Hold
Denature	95°C	3 seconds	40x
Anneal/Extend	60°C	30 seconds	

The ubiquitous housekeeping genes *eukaryotic initiation factor 1A (eif1a)* and *glyceraldehyde 3-phosphate dehydrogenase (gapdh)* were used as controls. Data were analysed according to the $2^{-\Delta\Delta CT}$method on Microsoft® Excel. Primers used in this study are presented in Table 6.

Table 6. qPCR primers

Gene	primers fwd	primers rev
bip	5' – ggtcggcggctccactcgtat- 3'	5' – agccggttctggtcgttggtaatg – 3'
atf6a	5' – ctggaggcgctggtgaaaagtg- 3'	5' – ccggacgggagatgggaaca – 3'
ire1a	5' – atggcgtggggagtgtgc – 3'	5' – gtattctgtgcggccaaggtaaa – 3'
copa	5' – aatttgagacaaagtcggcccg- 3'	5' – gatgaacacgatggtccagtcaga- 3'

2.3. CRISPR/Cas9 gene editing

2.3.1. Introduction

Gene-editing, a type of genetic engineering tool, offers the directed ability to change the chromosomal DNA sequence of a cell (Calos, 2016). The field arose from the understanding that cells could easily manipulate DNA through various processes in diverse entities such as restriction enzymes and phage genome integration in bacteria, retroviral genome integration in vertebrates, homologous recombination in yeast and VDJ joining in jawed vertebrates' immune system to name a few. These methods have been harnessed to develop tools to help scientists unravel the mechanisms of genetic diseases at a molecular level.

The understanding of cellular genetic material repair machinery has allowed us to exploit techniques to engineer genetic manipulation (Szostak et al., 1983). This came from the recognition that cells use double stranded breaks (DSB) to initiate recombination through either homologous-directed repair (HDR) or non-homologous end-joining (NHEJ) to repair the lethal breaks in genetic material (Ciccia and Elledge, 2010). NHEJ is error prone whereby the two broken ends of DNA are stitched back with insertions or deletion of nucleotides in a stochastic manner. HDR on the other hand, uses a DNA template with end homologous to the break site supplied and used to mend the DSB with precision (Szostak et al., 1983). Therefore, this understanding has led to the discovery of several enzymes that could induce DSBs and as potential genetic engineering tools.

Microorganisms' restriction enzymes were found to have a diverse repertoire of endonucleases that recognizes specific short palindromic DNA sequences (4-8 basepair, bp) that induces a DSB with relatively high specificity (Roberts, 2005). These Type II restriction enzymes soon became essential tools for *in vitro* recombinant DNA and revolutionized the biotechnology industry. Several other meganucleases have also been employed but with great technical difficulty. In the late 80s, the new understanding of transcription factors regulating gene expression through the recognition of DNA sequence motifs uncovered zinc ion-coordinated protein structures (zinc fingers, ZFN) (Kim et al., 1996, Horton et al., 1989). Coupled with a Type II restriction enzyme *Fok I*, these ZFN could bind to specific sequences and the endonuclease would induce the DSB. However their unpredictability in efficacy and laborious protein engineering led to a quick shift in focus to the newly identified transcription activator-like effectors (TALE), discovered in pathogenic bacteria of plants (Moscou and Bogdanove, 2009). TALE contained repetitive modules that are specific in recognizing one basepair each. They were easier to engineer and had more predictable efficacy. TALEs were also fused to *Fok I* nuclease (like ZFNs) to generate cutting domains thereby termed TALENs (Miller et al., 2011, Urnov et al., 2005). However, the engineering of TALE protein was again laborious and technically difficult, dampening its popularity in functional genomics. The advent of clustered regularly interspaced palindromic repeats (CRISPR)/CRISPR-associated-9 (Cas9) changed the field completely (Jinek et al., 2012).

CRISPR/Cas9 has generated a wave of excitement in the medical and scientific community in the last few years, carrying much promise in effective genome manipulation both *in vivo* and *in vitro* (Jinek et al., 2012, Doudna and Charpentier, 2014). This system stemmed from studies aimed at understanding how bacteria and archaea fend off invading nucleic acids. A single-guide RNA (sgRNA) binds and directs the Cas9 endonuclease to the paired DNA sequence the complementary DNA sequence it recognizes with an added recognition to a 2- to 4- base-pair conserved sequence named the protospacer-adjacent motif (PAM). This predictable Watson-Crick base pairing makes these sgRNA easier and quicker to engineer, thus eliminating the need for any complex protein designs. This ease and efficacy in virtually all cell types are the driving forces that led to an exponential rise in labs using CRISPR/Cas9 genome editing in medical breakthroughs and giving unprecedentedly rapid access to study gene function and its regulatory components.

2.3.2. CRISPR design and protocol

The protocol is adapted from previous works in zebrafish (Auer and Del Bene, 2014, Hwang et al., 2013, Irion et al., 2014):

2.3.2.1. Identification of efficient CRISPR target sequences in the gene of interest

2-3 target sequences as close to 5' UTR region or targeting exon 1 with zero potential off-targets were selected in the gene of interest using available online tools: zifit.partners.org, www.crispr.mit.net, www.chopchop.com. Multiple target sequences were used to allow one to act as a positive control for the other when assessing for the phenotype. Oligonucleotides specific to the target sequence with the appropriate overhangs were obtained. For *copa* CRISPR generation, a target site was selected and modified oligonucleotides were ordered as follows:

Forward: 5' - **TA**-target sequence (20 bases) – 3'
Reverse: 3' – **AAAC** – reverse complement of target sequence (minus last 2 nt) – 5'

When annealed together, they will create a double-stranded targeting sequence flanked by 4 bp single-stranded overhands, compatible with the overhangs generated by Bsa1 digestion of pDR274 plasmid (**Figure 10**).

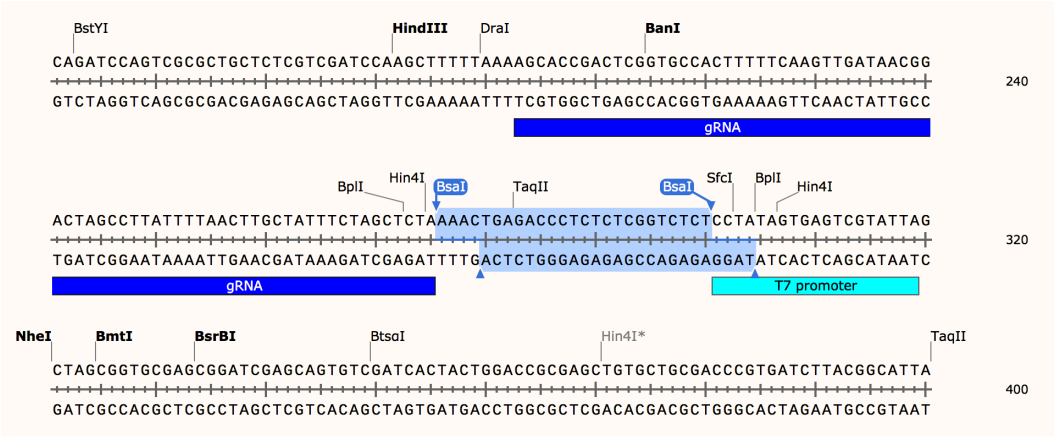

Figure 10. A section of the pDR274 plasmid map.
Dark blue bars shows the gRNA scaffold followed by the Bsa1 cut sites and the small portion removed during linearization. This leaves 4 bp overhangs that allows orientated ligation of the annealed gRNA oligo.

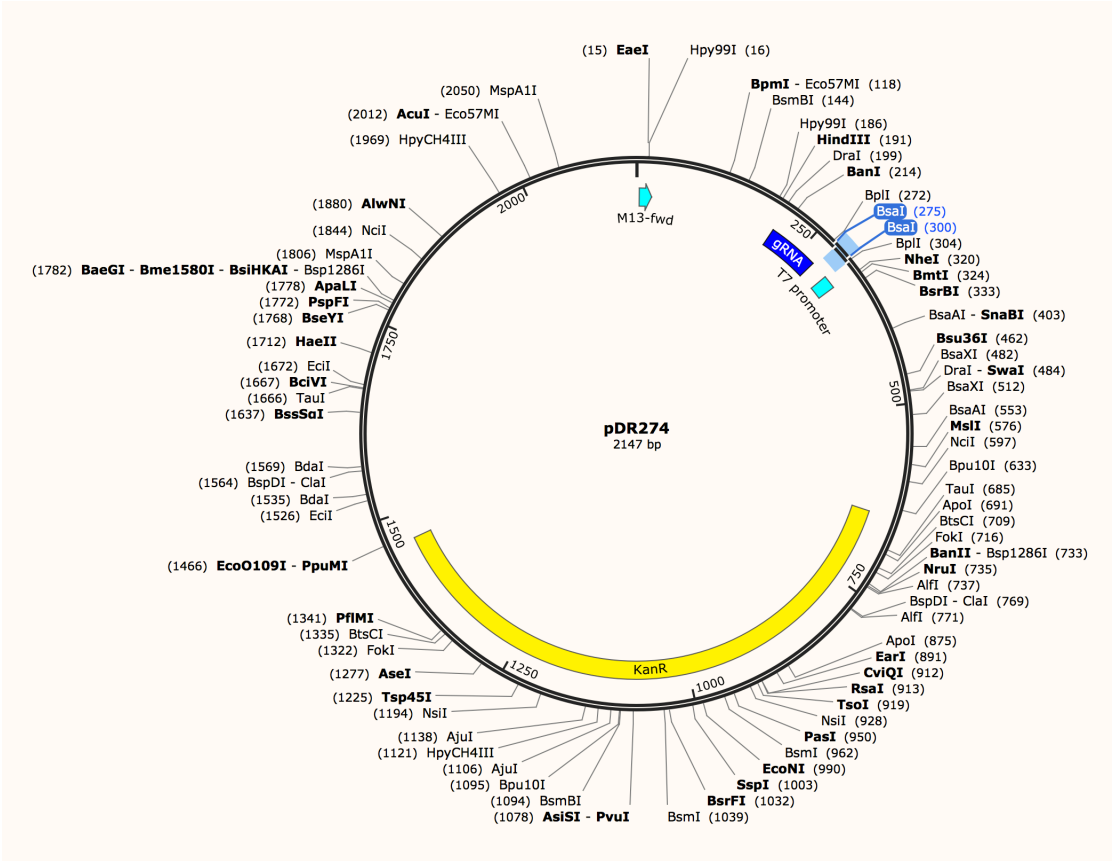

Figure 11. pDR274 plasmid map. Highlighted are the Bsa1 cut sites.

Table 7. copa gRNA sequence and oligos

	Target sequence	Oligo 1	Oligo 2
1	ggctgagtttccatccaaagcgg	TAggctgagtttccatccaaagcgg	AAACccgctttggatggaaactcag

2.3.2.2. Annealing of the gene specific oligonucleotides

The insert oligos were resuspended in DNase RNase free H_2O to create a 100µM (1000x) stock solution. Then mix 10µl insert-Oligo 1 and 10µl insert-oligo 2 100µM stocks in 80µL H_2O to generate a 10µM F/R stock. The two oligo-inserts were then annealed by boiling a mixture containing both oligos to 95°C for 5 minutes in a heatblock together with a T4 DNA ligase buffer and the removing the heatblock and letting it cool on the bench top overnight.

2.3.2.3. Ligation and cloning of the annealed oligos

Annealed oligos were ligated into pDR274 plasmid (**Figure 11**) that has been linearized with Bsa1-HR restriction enzyme using a T4 DNA ligase enzyme with its buffer.

Table 8. Ligation mix.

Component	Volume
Linearized pDR274	5µl
T4 ligase (New England Biolabs M0202S, 400 U/µl)	1µl
10x T4 ligase buffer	2µl
10 µM annealed insert-oligos	10µl
ddH_2O	4µl
Total	20µl

The ligation mix was incubated at RT overnight. Following ligation, 2µl of the mix was added to thawed competent bacteria cells and left on ice for 15-30 minutes. The mix was then subjected to heat shock at 42°C for 30 seconds and then subsequently plated on Kanamycin LB plates and left to incubate overnight at 37°C. Positive clones were sent for sequencing following DNA extraction from a further culture of bacterial stock to ensure correct sequences.

2.3.2.4. Transcription of the single guide-RNA and Cas9 mRNA

Plasmid containing the ligated gRNA was linearized with Dra1 (**Figure 12**) and RNA transcribed with T7 mMessage mMachine (Ambion) kit, purified with the Qiagen RNeasy Mini Kit and ethanol precipitated. Approximately 5µg of the T3T9pCSCas9 plasmid were linearized with Xba1 restriction enzyme and PCR purified after incubating at 37°C overnight.

Figure 12. Linearization of pDR274 with Dra1.

Highlighted in blue is the portion of plasmid cut out by Dra1 allowing transcription of the gRNA.

2.3.2.5. Injection of the sgRNA and Cas9 mRNA in zebrafish embryos

Injection protocol of gRNA and Cas9 are described previously in Section 2.2.9. Embryos are grown to 24hpf. A pool of 5 embryos per injection cohort were pooled, DNA extracted and using FAM PCR to determine efficiency of gRNA. Indel mutations were identified via multifragment DNA analysis and stable mutant lines were propagated and maintained.

2.4. Tissue specific CRISPR/Cas9 using multisite Gateway Cloning

2.4.1. Identification of target sequence

Only target sequence (sgRNAs) that have shown effective targeting (generated using protocol 2.3 are chosen for further tissue specific CRISPR. The following oligonucleotides were ordered for the *copa* tissue specific CRISPR:

Forward: 5’ - target sequence (20 bases)-GT – 3’
Reverse: 3’ – reverse complement of target sequence-GA – 5’

When annealed, the insert oligos will generate a 2 bp overhang on both ends corresponding to the BseR1 cut sites in the destination vector (**Figure 13**).

Table 9. Tissue specific copa CRISPR oligos sequence

	Target sequence	Oligo 1	Oligo 2
1	ggctgagtttccatccaaagcgg	ggctgagtttccatccaaagcggGT	ccgctttggatggaaactcagccGA

The oligos were annealed following protocol 2.3.2.

2.4.2. Tissue-specific CRISPR vector assembly

The *pcmlc2*:GFP;U6:gRNA;Prom:Cas9 (**Figure 14**) destination vector was used for this study. The vector was digested with BseRI restriction enzyme and purified on a 1% agarose gel. The annealed oligonucleotides from section 2.4.1 were then ligated into the BseRI digested destination vector (1:20 vector:insert ratio) (**Figure 13**) and transformed into Top10 competent ccdB bacteria, plated on LB agar and selected with ampicillin and chloramphenicol. Plasmid DNA was extracted from a few colonies and sequence checked using the following primer: CCTCACACAAACTCTGGATT. Gateway reaction was then performed with the destination vector containing the gRNA, a p5' with a *ubi*:switch promoter and *sox10* promoter, pME containing a zebrafish codon-optimized Cas9 (Ablain et al., 2015) and p3E-polyA according to protocol in section 2.2.8.5. Following LR recombination, ligated vectors were transformed into chemically competent bacteria, plated on LB Agar and selected with ampicillin. Plasmid DNA from a few colonies were extracted and checked for correct recombination by sequencing.

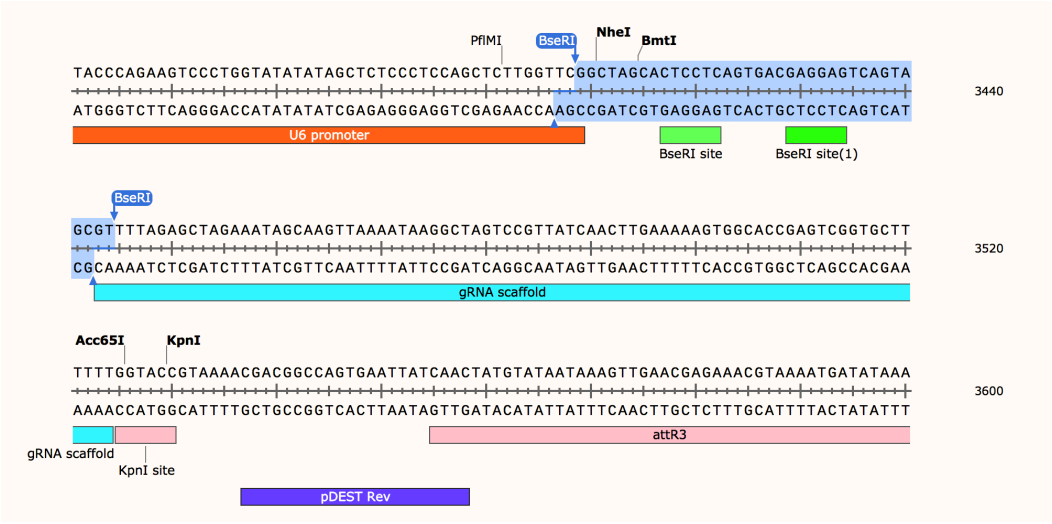

Figure 13. pDestTol2U6gRNA sequence map showing BseR1 cut sites.

Followwing BseR1 diggestion, it leaves a 2 bp overhang for ligating annealed oligos next to the gRNA scaffold and U6 promoters

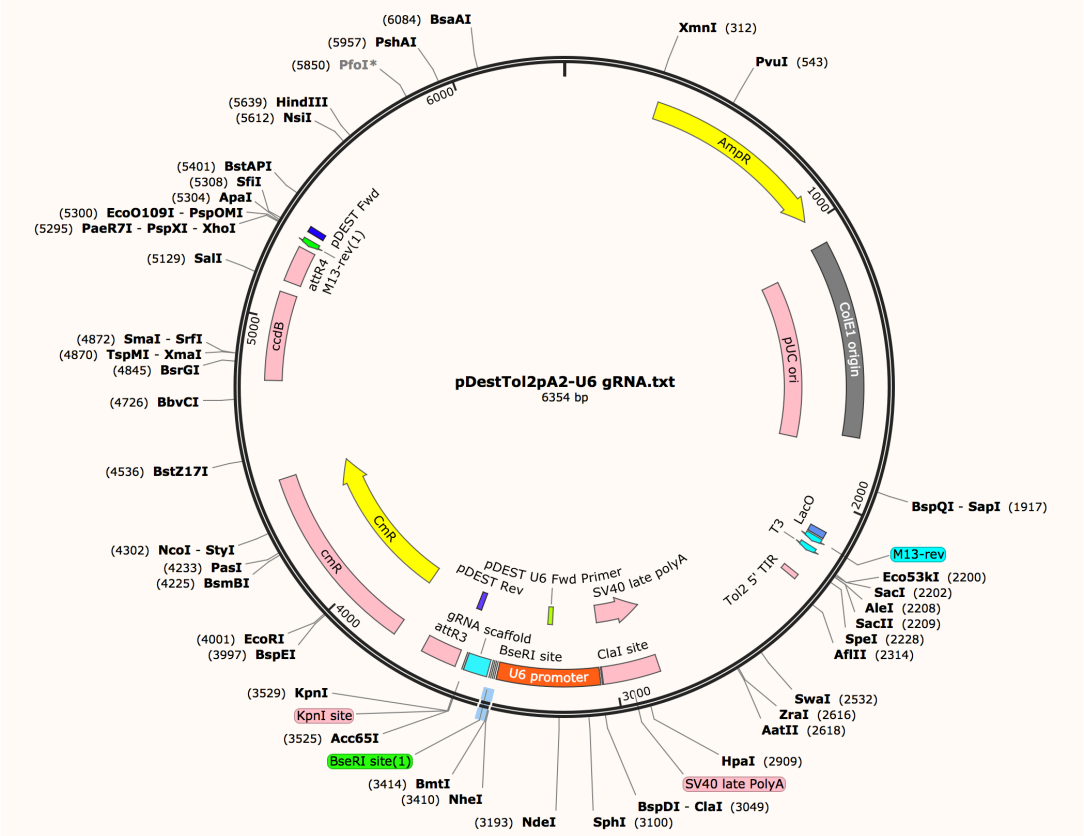

Figure 14. Plasmid map of pDestTol2pA2-U6gRNA.

2.4.3. Injection of tissue-specific CRISPR construct in zebrafish embryos

20-30pg of CRISPR vector with 20pg of Tol2 mRNA were injected into one-cell stage WT embryos. For the CRISPR vector with *ubi*:switch as the promoter, the vector mix was injected into one-cell stage embryos from a *sox10*:Cre zebrafish transgenic line. Embryos were allowed to develop at 28.5°C. F0 embryos were sorted based on expression of the transgenesis marker (i.e. *cmlc*:GFP – green heart). To generate stable lines, positive F0 fish were raised to adulthood and backcrossed to WT Tübingen strain and positive F1 embryos were selected and raised to adulthood. This is to ensure germline transmission and overcome the mosaic pattern of expression at F0 generation.

2.5. Whole-mount RNA *in situ* hybridization

2.5.1. DNA template

DNA template for *in situ* hybridization was prepared either from cDNA PCR amplification with a T3 anchor attached to the reverse primer or from a linearized expression plasmid

containing the cDNA clone of interest. For the project, probes were generated using the former method to allow for higher throughput analysis.

2.5.2. Digoxigenin labelled RNA probe synthesis

For probe synthesis, PCR generated or plasmid linearized DNA template was added with 5X transcription buffer, DIG-RNA labelling mix (UTP), RNAse inhibitor, T3 RNA polymerase (20U/µl), and incubated for at least 2 hours in a 37°C water-bath. 2µl of RNAse free DNAse I and Xµl of RNAse free H2O were then added and incubated for a further 30 minutes at 37°C. The mix was then put on ice and 5µl was run on a 1% agarose gel to quickly assess quality of transcription.

The RNA was then precipitated with 1/10 volumes of 3M NaOAc pH5.2 and 2 volumes of 100% ice cold ethanol at -20°C for at least 2 hours. The RNA was then centrifuged for 20 minutes at 4°C, washed once with 2:1 volumes of 70% ethanol and re-centrifuged for 5 minutes at 4°C to pellet the RNA. The ethanol was then removed and pellet left to air-dry and subsequently resuspended in 100µl ddH_2O and stored at -20°C.

2.5.3. Whole-mount RNA *in situ hybridization (WISH)*

WISH was performed as previously described on appropriately staged embryos with minor modifications (Thisse and Thisse, 2008). Embryos were collected at the desired stages, fixed in 4% PFA/PBS, bleached with 1.5% H_2O_2/1.5% KOH and stored in methanol at -20°C until further used.

Embryos were placed in appropriate wells and rehydrated in a progressively decreasing concentrations of MeOH:PBST and subsequently washed 3 times in 1X PBST for at least 5 minutes prior to digestion with 10µg/ml Proteinase K for 30 minutes. After a short rinse in pre-heated pre-hybridization transfer solution (HYB-), pre-hybridisation was performed at 70°C for at least 4 hours in pre-hybridisation solution (HYB+) (50% formamide, 5X SSC, 50µg/ml heparin, 200µg/ml torula yeast type VI RNA (Sigma R6225) and 0.1% Tween-20). Digoxigenin-labeled anti-sense riboprobes (Roche Applied Science, Penzberg, Germany) were then added and allowed to incubate overnight at 70°C.

Post-hybridisation washes were performed the following day at 70°C in solutions of 55% Formamide and 2X SSC/0.1% Tween-20 followed 55% Formamide and 1X SSCT, then by

1 x30 minutes washes in 1X SSCT and then by 2 times 30 minutes washes in 0.2XSSCT. Embryos were transferred in 1X MABT (0.1M maleic acid, 0.15M NaCl, pH 7.5 with 0.1% Tween-20) before blocking in 1XMABT/10%BSA/2%FCS for at least an hour. After pre-blocking, embryos were transferred to the anti-digoxigenin-alkaline phosphatase conjugated F_{ab} fragments (Roche) (1:10,000) in blocking solution and incubated overnight at 4°C with gentle rotation. The following day, embryos were extensively washed in 1X MABT and then equilibrated in alkaline phosphate buffer with 0.1% Tween-20 (NTMT; 5M NaCl, 1M Tris-Cl pH9.5, 1M $MgCl_2$) solution (60mM Tris-HCL pH 9.5, 60mM NaCl, 30mM $MgCl_2$ and 0.1% Tween-20) for at least 15 min. Nitro blue Tetrazolium Chloride (NBT) and 5-Bromo-4-chloro-3-ondolyl phosphate (BCIP) were used at a concentration of 4.5mg/ml and 3.5mg/ml respectively dissolved in NTMT to achieve staining. During the colour reaction, embryos were kept from light exposure and monitored for staining. Rinsing with 1X PBST stopped the reaction. After staining, embryos were refixed in 4% PFA and dehydrated in 100% MeOH and stored in 70% glycerol. When assaying for differences in expression, the development of the staining reaction was monitored carefully and stopped at the same time. PFA fixed embryos were then dehydrated in 100% MeOH and either stored at -20°C or transferred unto glycerol 85% for RT storage and imaging. For imaging of ventral cartilage structures, the head was removed at the level of the pectoral fin, mounted on a cover slip with 100% glycerol and imaged using a Nikon Eclipse FN1 upright compound microscope.

Table 10. Hybridization minus solution (HYB-)

Component	Volume
50% formamide	250ml
20X SSC	125ml
Tween-20	2.5ml
ddH_2O	120ml

Table 11. Hybridization plus solution (HYB+)

Component	Volume
HYB-	500ml
Torula Yeast tRNA	2.5g
Heparin (50 µg/ml)	2.5mls

2.5.4. Probes used for in situ hybridization

Probes were generated from PCR with a T3 anchor (ggatccattaaccctcactaaaggg) to the 5' end of the reverse primer.

Table 12. Primer pairs for *in situ* hybridiation PCR reaction

Gene	Forward 5'-3'	Reverse 5'-3'
wls	attgcggatggagcttcgatc	tgccttcttcactggcatctat
wnt9a	cagcaactcaggacgaacgaaatg	cacgaaattggcaagcagctca
wnt5b	aagtgtcatggcgtctcag	ggttccaacagagggttttt
gpc4	actgctggagcgcatgtttcgac	cagtgtgtgttggagaaaggatcg
sox9a	ccgatgaacgcgtttatggtgt	ctcctcccaccaccccgaaaa
col2a1a	Synthesized from plasmid with T3 RNA polymerase (ZDB-GENE-980526-192)	
col10a1a	tggacttaaaggagacactggtgc	gtcctcaaggtgcaaagggttt
col1a2	tggataaccgtattaccgcc	cactagtcataccaggatc
runx2a	agtggaagaggaaagagcttcacg	cctcatccgggtcataccaatt
bapx1	gtgttgtgggtcagtttcag	ctcgtgtttggaaagctctg
copa	Synthesized from plasmid with T7 RNA polymerase	

2.6. Immunohistochemistry

2.6.1. Antibodies and concentrations used

Table 13. Antibodies and working concentrations

Antibody	Concentration	Catalog number
Monoclonal anti-acetylated tubulin mouse	1:200	Sigma T7451
Monoclonal anti-BrdU mouse	1:400	Sigma B8434
Donkey anti-mouse IgG secondary, Alexa Fluor® 568 conjugate	1:400	ThermoFisher A11004
Rabbit IgG anti-GFP, Alexa Fluor® 488 conjugate	1:400	ThermoFisher A21311
Alexa Fluor® 647 Phalloidin	1:400	ThermoFisher A22287
Alexa Fluor® 594 Phalloidin	1:400	ThermoFisher A12381

2.6.2. Whole-mount antibody staining

For antibody staining, embryos at the desired stage were fixed with 4% PFA for 1-2 hours at RT with gentle agitation and then washed at least 3 times in PBST for 5 mins each. Embryos were then permeabilized with 100% ice-cold acetone for 7 minutes followed by 3 further PBST washes. Embryos were then washed in multiple changes of PBS/1% dimethylsulfoxide (DMSO)/0.1% Triton-X (PBSDTx). Embryos were then blocked in PBSDTx with 10% goat serum (blocking solution) for at least 1 hour at RT. The embryos were incubated in the primary antibody diluted per published concentrations in blocking solution overnight at 4°C. The following day, the embryos were washed with multiple changes of PBSDTx the whole day to remove the primary antibody. The embryos were blocked again for at least 1 hour in blocking solution and secondary antibody added and allowed to incubate overnight at 4°C. The next day, the embryos were rinsed extensively in PBSDTx before storing in 35% glycerol/PBST at 4°C prior to confocal imaging.

2.6.3. BrDU labelling

BrDU incorporation was performed as previously described with some modifications (Verduzco and Amatruda, 2011). 6dpf embryos were pulsed with 15mM of BrDU (Sigma B5002) /15% DMSO E3 on ice for 20 minutes and chased for 4 hours in warm E3 at 28.5°C. Embryos were then fixed in 4% PFA and stored in methanol at -20°C. Following rehydration in graded Methanol:PBST series, the embryos were digested in 10µg/mL Proteinase K for 30 minutes, washed in PBS/0.1%Triton-X (PBSTx) and refixed in 4% PFA for 20mins. Embryos were then incubated in 2N HCL for 1 hour to denature the double-strand DNA and free the BrDU epitopes, rinsed with PBSTx and incubated in blocking solution (10% donkey serum, 1X PBSTx) for at least 1 hour before incubating in mouse anti-BrDU (1:400 Sigma) overnight at 4°C. Embryos were then washed all day with multiple changes of PBSTx and then incubated in secondary antibodies (donkey Alexa-Fluor-594 1:400 and conjugated anti-GFP Alexa Fluor 488 1:400) overnight. Following multiple PBSTx washes, embryos were stored in 35% glycerol/PBST at 4°C. BrDU positive chondrocytes (yellow cells – *sox10*:GFP positive and BrDU red positive) were counted from confocal Z-stacks.

2.7. Sodium dodecyl sulfate Polyacrylamide gel electrophoresis (SDS-Page) Western blotting and Chemilluminuscent detection of proteins

2.7.1. Protein extraction

To determine protein levels in *copa*, *wnt9a* and *wls* mutants, embryos displaying the phenotype were collected for western-blot analysis. Yolks of individual embryos were carefully removed by manually separating it using forceps. Protein was extracted by adding 500µl of RIPA buffer (ThermoFisher, 89900) to at least 50 mg of embryos (pooled) (or 1:10 weight:buffer ratio). Using a needle and syringe, embryos were physically broken apart and then further sonicated for 5 seconds with a 1 second rest per 1 second pulse and immediately put on ice. The samples were then centrifuged for 20 minutes at 13,000 rpm to pellet any remaining debris. The suspensions were transferred to a fresh tube and stored at -80°C.

2.7.2. Protein quantification

Protein quantification was performed using the Pierce™ bicinchoninic acid (BCA) protein assay kit (ThermoFisher 23225) per the manufacturer's protocol. A spectrophotometer set to 562nm was used to measure the absorbance of the samples. A standard curve was plotted using a BSA standard concentration and protein concentration determined. At least 3 replicates of the sample were used and an average obtained for the final concentration measurement.

2.7.3. SDS-PAGE electrophoresis (Western blotting)

20µg/ml of protein per sample was mixed with appropriate volume of Laemli buffer with Beta mercaptanol and boiled to 95°C for 5 minutes and cooled on ice prior to loading onto a pre-cast 4-12% gradient Bis-Tris gel (Invitrogen-NUPAGE® Novex gels). Gels we ran using NuPAGE MES® running buffer (Invitrogen) at 150V for around 1-2 hours (following the dye front). Next, the proteins were electrotransferred to PVDF membrane sandwiched between sponges in the Invitrogen transfer cassettes, transferred at 15V at RT for 2 hours. Following transfer, the membrane was blocked in 5% skim milk/PBST for at least 1 hour and then incubated with primary antibody overnight at 4°C with gentle rotation (anti-*copa*, anti-*wnt9a*, anti-*wls*). The following day, the membrane was

extensively washed with multiple changes of PBST. The secondary antibody (in this case an anti-rabbit IgG conjugated with HRP, 1:5000) was diluted in blocking solution and incubated with the membranes at RT for at least 1 hour. The membrane was then washed extensively in PBST. Proteins were visualized using the ECL chemilluminescence detection kit (Thermo Scientific) and exposure on a film. For loading control, the same membrane was then stripped off to remove the bound antibodies, washed, blocks and counter probed with anti-β actin monoclonal antibody (Abcam) and visualized again with ECL and exposed on a separate film.

2.8. Cartilage and bone staining

2.8.1. Alcian blue cartilage stain

Alcian blue dyes stain the proteoglycan components of chondrocyte extracellular matrix that can then be used to visualize cartilage patterns in zebrafish embryo or adults (Goldstein and Horobin, 1974, Walker and Kimmel, 2007). Cranial cartilage structures are best stained after 72hpf. Zebrafish embryos at the appropriate stages were fixed in 4% PFA/PBS at RT for at least 2 hours or 4°C overnight with gentle agitation. Embryos were then washed with 1X PBST to completely remove any trace of PFA. Then they were dehydrated in 50% Ethanol for at least 10 minutes prior to being transferred into a 0.04% solution of Alcian blue staining solution and incubated overnight with gentle rotation. The following day, the Alcian blue staining solution was removed, embryos rinsed with H2O briefly and bleached with 1.5% H2O2/1.5% KOH for 1 to 3 hours depending on stage of the embryos. The reaction was carefully monitored and stopped once eye pigmentation has completely cleared. The embryos were then rinsed in 1X PBST briefly and then their tissues were cleared with 0.1% trypsin/PBS for 10-30 minutes at RT. Trypsin digestion was stopped once brain tissue has cleared and embryos were then rinsed extensively in 1X PBST and stored in 75% glycerol at RT.

Table 14. 0.4% Alcian Blue stock solution (100 ml)

Component	Volume
100% EtOH	70ml
ddH_2O	30ml
Alcian blue powder	0.4g

Table 15. Alcian Blue staining solution (100 ml)

Component	Volume
95% EtOH	70ml
ddH_2O	6ml
1M $MgCl_2$	19ml
0.4% Alcian Blue stock	5ml

2.8.1.1. Microdissection and mounting of stained cartilage

Following staining of larval skeleton with Alcian blue, stained cartilage elements were dissected out and mounted on a slide for further imaging. Forceps were used for dissections. First the eyes were carefully removed and discarded. Then, scraping the brain dorsal of the neurocranium and gently lifting the brain away helped removed the brain tissue. Next, one forcep is placed at the base of the notochord and the skull to stabilize the head. The ventral cartilage structures were removed by carefully pulling the quadrate process of the palatoquadrate away from the ethmoid plate and the hyposplenium away from the posterior neurocranium.

For lateral jaw preparation, once the ventral cartilage structures are successfully detached from the neurocranium, the two ceratohyals are detached to split the posterior arches at the midline. Gently pressing down and cutting the midline then separate the Meckel's cartilage halves. The remaining structures were then flat mounted on a slide containing a small droplet of pure glycerol and a 18x18mm coverslip placed on top and moved to achieve ideal orientation and placement of the structures.

2.8.2. Alizarin red bone stain

Alizarin red stains the calcified matrix associated with bone (Walker and Kimmel, 2007). It can be used as whole-mount preparations or live staining. Alizarin (1,2-dihydroxyanthraquinon) emits a red signal under fluorescent green light and from personal experience, produced a more sensitive and specific method of visualizing the development bone compared to whole-mount staining. For live Alizarin red stain, live larvae were incubated in a 0.005% Alizarin Red S (Sigma) /0.01M HEPES buffer in E3 overnight at 28.5°C. The following day, larvae were extensively washed with E3, anaesthetized with tricaine and mounted on a coverslip prior to confocal imaging. Alizarin red fluorophore

was excited at 580 nm. To distinguish cartilage and bone structures, alizarin red stain was performed in embryos with a Tg(*sox10*:GFP) background.

2.9. Chondrocyte measurements, cell count and statistical analysis

Meckel's cartilage width (W) was measured from the distance between opposing retroarticular processes and the length (L) was measured from the midline to the tip of the retroarticular process. At least 10 different fish Meckel's cartilage was used for measurement. Chondrocyte cell count was calculated by adding the total number of cells on one-half of the Meckel's cartilage obtained from a flat-mounted Alcian blue image in 10 different embryos. A one-way ANOVA test was used to compare means of representative groups and where the p-value is significant, a Bonferroni's multiple comparison tests were performed to compare means of mutant to wild-type embryos. Where numbers were small, Kruskal-Wallis test with Dunn's multiple comparisons test was used to compare medians across various groups. Rose plots were generated from Oriana Statistical program.

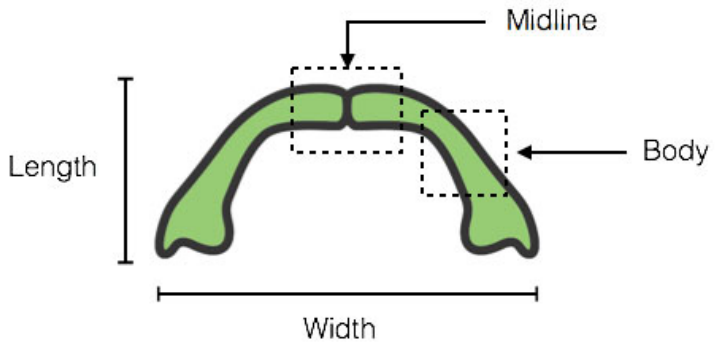

Figure 15. Graphics showing measurement points.

2.10. Live imaging

Tg(*sox10*:GFP) background embryos were imaged using Nikon Ai scanning confocal microscope, mounted in 3.5% methylcellulose-0.013% Tricaine. Multiple embryos were imaged and traced till 4dpf when they reveal their phenotype. Embryos were additionally genotyped for confirmation.

2.11. Acridine orange staining

Apoptosis detection by acridine orange was performed as previously described (Verduzco and Amatruda, 2011). 6dpf embryos were incubated in 2μg/mL solution of acridine orange (Sigma, A6014) in E3 for 30 min at room temperature. Embryos were subsequently washed extensively in E3, tricaine treated and mounted prior to confocal imaging.

Chapter 3: Distinct roles of *wls*, *wnt9a*, *wnt5b*, *gpc4* in endochondral ossification

Published in Developmental Biology Jan 2017 15;421(2):219-232, PMID 27908786 (with cover image Vol 421 Issue 2)

Work presented here overlaps with the work published but offers more detailed insight into some of the experiments, additional data, further hypothesis and data analysis.

3.1. Introduction

During craniofacial development, CNCC are assembled into cartilaginous structures that prefigure development of the bony cranial skeleton (Olsen et al., 2000, Kague et al., 2012, Eames et al., 2012, Hammond and Schulte-Merker, 2009, Paul et al., 2016). After migrating into the first (mandibular) and second (hyoid) pharyngeal arches, CNCCs give rise to a series of cartilaginous anlage (Mork and Crump, 2015). Meckel's cartilage is a first pharyngeal arch derivative that is considered a scaffold and template for mandibular development. As a recap to craniofacial development and anatomy in Chapter 1, the mandible develops in two distinct steps; first through intramembranous ossification supported by the body of the Meckel's cartilage followed by endochondral or perichondral ossification of the distal and proximal regions (hereafter referred to as endochondral) (Frommer and Margolies, 1971, Savostin-Asling and Asling, 1973, Eames et al., 2013). In zebrafish, the mentomeckelian (distal midline) and retroarticulars (proximal jaw joint) forms through endochondral ossification while the dentary bone (body) forms through intramembranous ossification (Eames et al., 2013). These bones all later fuse together to form bony sutures. Other craniofacial bones that also undergo endochondral ossification include the ceratohyal and the ceratobranchials (Schilling and Kimmel, 1994, Schilling and Kimmel, 1997, Hammond and Schulte-Merker, 2009, Paul et al., 2016).

Most craniofacial bones, including the mandibular bone are CNCC-derived compared to the limbs and trunk where they are mesoderm-derived. Bones that lie more posteriorly such as the cleithrum, occiput or parietal bones of the skulls have mixed origins from CNCC as well as mesodermal derived (Kague et al., 2012). Despite appearing histologically similar, CNCC-derived bones show distinct gene expression signatures, higher alkaline phosphatase activity, higher proliferation and greater regenerative capabilities (Quarto et al., 2010, Ichikawa et al., 2015, Hochgreb-Hagele et al., 2015, Heuze et al., 2014). Due to these differences, further work is required in understanding and characterizing their cellular mechanisms. Identifying the role of local signalling pathways that help to properly develop these cartilage structures is critical to understanding how craniofacial bones acquire their shape and size. Additionally, how the cartilage anlage supports endochondral ossification during mandibular development remains to be explored. The Wnt signalling pathway has long been implicated in bone development. Studying this pathway may shed light into the link between Meckel's cartilage and mandibular ossification.

The Wnt family proteins are important in regulating acral bone formation, maintenance and remodelling (Olsen et al., 2000, Rodda and McMahon, 2006). Canonical Wnts have been extensively studied in mesoderm-derived bone biology and is important for mesenchymal precursor cells to differentiate into chondrocyte or osteoblast lineages during skeletogenesis (Rodda and McMahon, 2006). Loss- and gain- of function studies have highlighted the requirement for β-catenin to repress chondrogenesis by favouring osteogenesis and play a vital role in bone homeostasis by regulating osteoblastic and osteoclastic activity (Hill et al., 2005, Day et al., 2005). Many other Wnts can also act through a β-catenin-independent (non-canonical) pathway, which regulates cell polarity and migration during embryonic development (Semenov et al., 2007). In chick, ectopic *Wnt5a* expression led to a delay in chondrocyte differentiation while ectopic *Wnt4* promoted differentiation (Hartmann and Tabin, 2000). Overexpression of *Wnt14* in chick limbs led to ectopic joint formation (Hartmann and Tabin, 2001). In murine long bones, endogenous *Wnt5a* and *Wnt5b* in chondrocytes of long bones regulate endochondral skeletal development through coordinating cell proliferation (Yang et al., 2003). In zebrafish, non-canonical Wnts (Wnt4a, Wnt11r, Wnt5b, Wnt11) play a key role in early and late craniofacial patterning from the formation of pharyngeal pouches to the patterning and shaping of cartilaginous-structures (Curtin et al., 2011, Choe et al., 2013, Heisenberg et al., 2000, Sisson et al., 2015). These studies highlight the importance of non-canonical Wnt in skeletal development. However, how non-canonical Wnt ligands exert their function during cartilage maturation and how this may affect endochondral ossification remains to be explored.

To determine the role of non-canonical Wnt in craniofacial development, we analysed mutants in different steps of Wnt signalling; *wls*, *gpc4* (Wnt trafficking proteins) and *wnt9a* and *wnt5b* (ligands identified as non-canonical ligands) (Sisson et al., 2015, Topczewski et al., 2011). These Wnt mutants are described in Chapter 2 (Methods and Materials). In short, the *wls* mutant (*c186*) was a gift from Marnie Halpern laboratory and previously used to study habenular development (Kuan et al., 2015). The mutant was developed used ENU mutagenesis. The *gpc4* and *wnt5b* mutants are viral insertional lines obtained from ZIRC and our *wnt9a* line (with a -4bp deletion) was generated using CRISPR/Cas9 gene editing technology (Rochard et al., 2016).

We focused our study on detailed cellular events in Meckel's cartilage morphogenesis and ossification by asking these questions:

1) Does the non-canonical Wnt pathway affect Meckel's cartilage development? And if so, how does it affect chondrogenesis and why do their shape differ?

2) Do defects in Meckel's cartilage preclude defects in mandibular ossification? And if so, what is the mechanism and what role does the non-canonical pathway play during zebrafish mandibular endochondral ossification?

Our data suggests that different Wnt genes have site-specific requirements during Meckel's cartilage development and this affects timely cartilage maturation and the onset of the endochondral ossification program.

3.2. Results

3.2.1. wls, wnt9a, wnt5b and gpc4 are expressed in discrete regions of the ventral craniofacial structures

To first determine if Wnt signalling are important during craniofacial development, we sought to observe their expression patterns. Previous studies have showed that *wls, wnt9a, wnt5b* and *gpc4* are expressed in ventral cartilage elements at an early time-point of 55hpf (start of palatogenesis) and 72hpf (Meckel's cartilage formation) (Rochard et al., 2016, Curtin et al., 2011, Sisson et al., 2015). Sisson and colleagues showed that *gpc4* is expressed in the pharyngeal endoderm, neural crest and mesoderm while *wnt5b* is restricted to the neural crest and mesoderm (Sisson et al., 2015). To understand the role of these genes in early ossification, we analysed their gene expression at a later craniofacial developmental stage by performing whole-mount RNA *in situ* hybridization (WISH) at 96hpf, which is when ventral craniofacial cartilage structures have formed and ossification is initiated (forming the dentary, ceratohyals, ceratobranchial 5, opercle, cleithrum, maxilla, quadrate and one pair of brachiostegal rays).

Here we show that *wls*, *wnt9a* and *gpc4* transcripts were detected in the mesenchyme surrounding the chondrocytes of the ventral cartilage structures, with *wls*, *wnt9a* and *wnt5b* transcripts localized anteriorly. Clear expressions of *wls*, *wnt5b* and *gpc4* were observed at the jaw joint (**Figure 16**A, C, D, arrowhead). *wnt5b* and *wls* transcripts co-localized to the oral epithelium (**Figure 16**A, C, black arrowhead) while *wnt9a* showed a discrete region of expression at the midline of Meckel's cartilage (**Figure 16**B, arrowhead). *wnt5b* expression was observed within the ceratobranchials and mouth opening epithelium (**Figure 16**C). These detailed delineations of gene expressions supplements previously published gene expression patterns and provided us with greater insight into the craniofacial phenotype observed. 40X images shows detailed areas of expression described above.

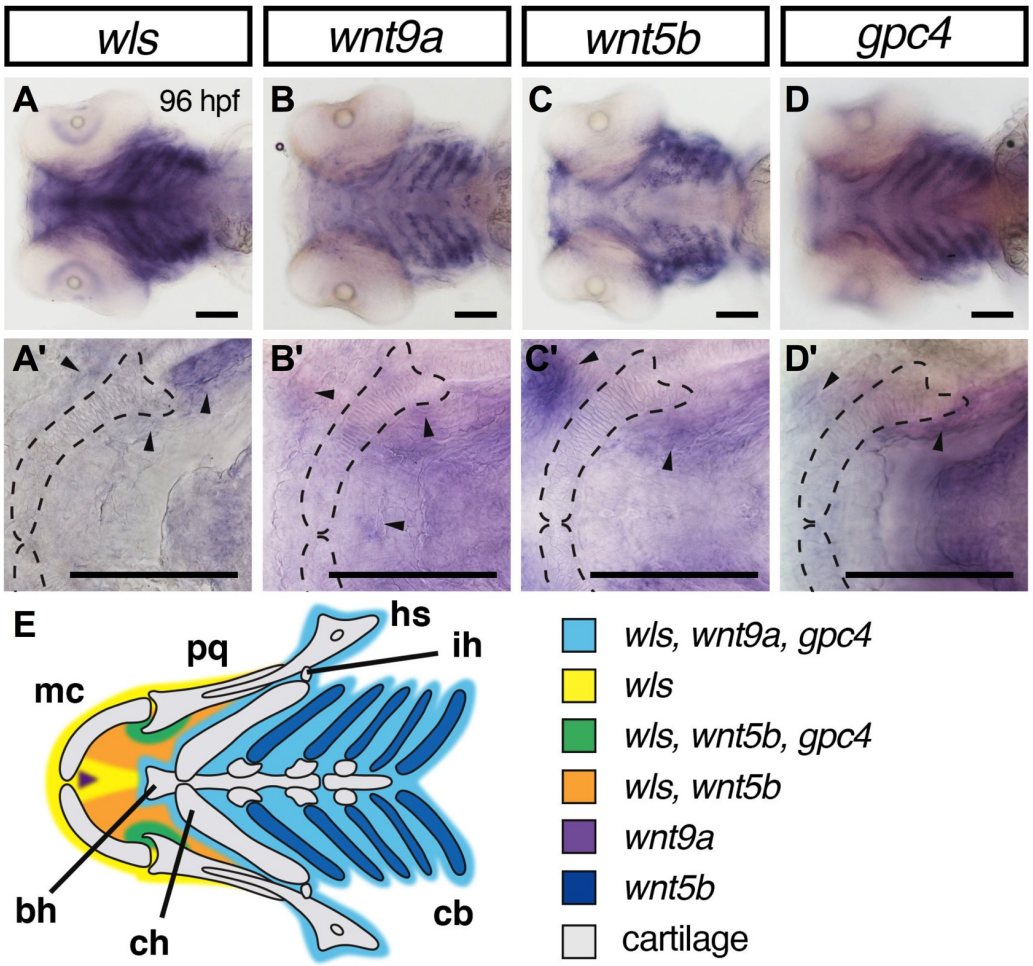

Figure 16. Overlapping domains of gene expression of *wls*, *wnt9a*, *wnt5b*, and *gpc4* in ventral craniofacial cartilages.

(A-D) Whole mount RNA *in situ* hybridization with ventral views and 40X views focusing on Meckel's cartilage in A'-D'. At 96hpf, *wls* (A) is expressed in the surrounding tissue including the Meckel's cartilage and co-expressed with *wnt9a* (B) and *gpc4* (D) in the posterior ceratobranchials (light blue) in contrast to *wnt5b* (C) that appeared to be expressed in the chondrocytes of the ceratobranchials and the blood vessels surrounding them. *wls, wnt5b* and *gpc4* co-localized to the surrounding mesenchyme around the jaw joint (green). *wnt5b* is expressed in the oral epithelium with *wls*. There is discrete expression of *wnt9a* in the anterior midline (purple) adjacent to the intermandibulare anterior muscle. Annotation: Meckel's cartilage (mc), palatoquadrate (pq), hyosymplectic (hs), interhyal (ih), ceratobranchial (cb), ceratohyal (ch), basihyal (bh). Scale = 50 μm.

3.2.2. Loss of Wnt signaling leads to abnormal Meckel's cartilage chondrocyte arrangement

Prior analyses by our group and others have shown that there is gross shortening of Meckel's cartilage in *wls, wnt5b* and *gpc4* mutant lines and *wnt9a* morphants showed a complete loss of Meckel's and ventral cartilages (Curtin et al., 2011, Wu et al., 2015, Sisson et al., 2015). To gain better understanding of the cause of Meckel's cartilage shortening, we performed a systematic and detailed analysis of Meckel's in each of these existing mutants. Alcian blue was used which stains for the proteoglycans within the extracellular matrix secreted by chondrocytes. 96hpf was chosen as most cartilage structures have formed in WT and the full arched shape can be appreciated. A ventral view (**Figure 17**A) provides details of the ventral cartilage elements where the Width (W) of Meckel's cartilage from both ends of the retroarticular can be calculated as well as the length (L) from the midzone of Meckel's cartilage to an imaginary line between the retroarticulars. A lateral view (**Figure 17**F) allows for assessment of the ventral cartilage structures in relation to the neurocranium above (including the ethmoid plate and middle ear structures). Microdissection of the ventral cartilage structures is necessary to allow flat mounting and clearer visualization of the chondrocytes during imaging (**Figure 17**K, P). Zoomed in (40X) images of Meckel's cartilages were used for cell count (**Figure 17**U).

In *wls* mutants, obvious shortening of every cartilage element is observed with a smaller Meckel's cartilage (**Figure 17**B, G, L, Q, V). *wnt9a* mutant display an obvious opened-mouth phenotype by 96hpf. This can be appreciated on the lateral view where the Meckel's cartilage is inverted (**Figure 17**H). Additionally, there is slight shortening of the ceratobranchials observed in the *wnt9a* mutant (**Figure 17**C, H, M, R, W). *wnt5b* mutants' phenotype appears similar to *wls* mutants with shortening of all cartilage elements (**Figure 17**D, I, N, S, X). Like *wnt5b* and *wls* mutants, *gpc4* mutants also display marked shortening of all cartilage structures, having a more severe defect compared to *wls* (**Figure 17**E, J, O, T, Y).

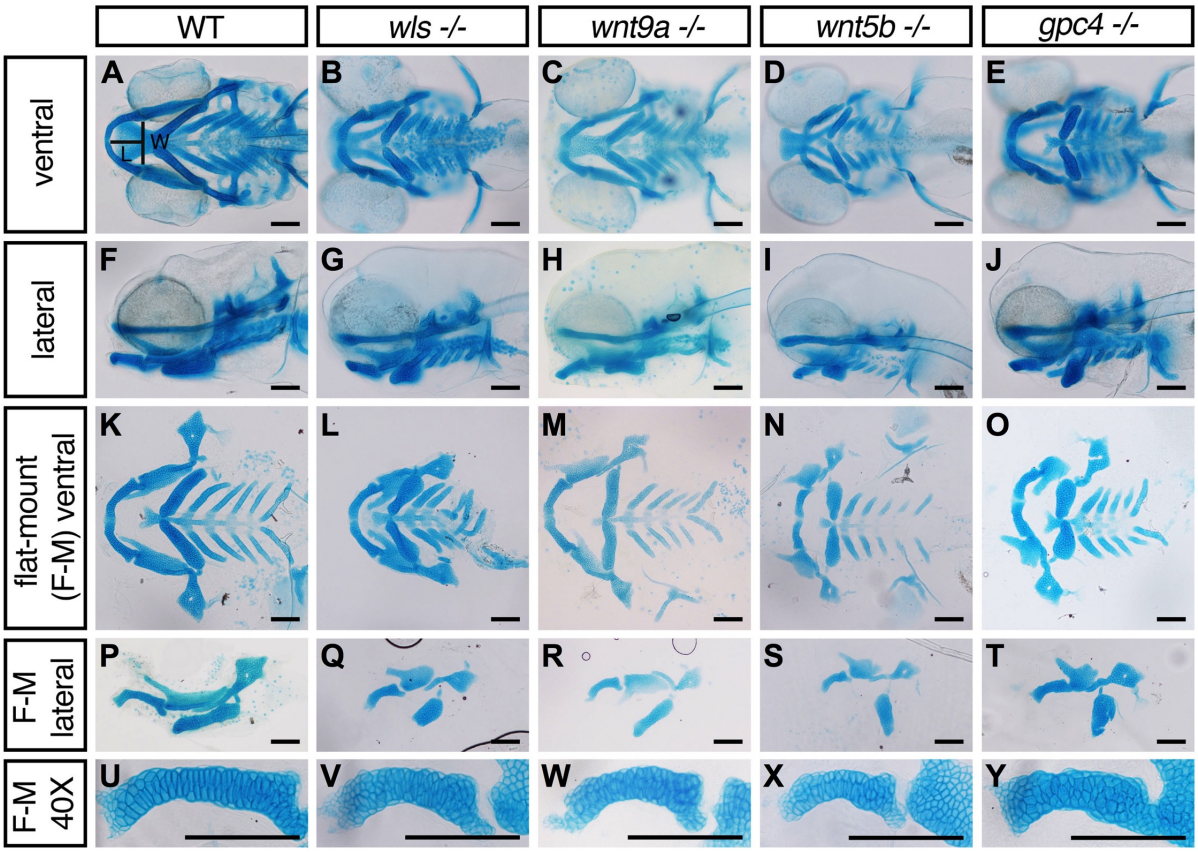

Figure 17. Alcian blue showing cartilage defects in *wls, wnt9a, wnt5b* and *gpc4* mutants.

(A-E) Ventral and lateral (F-J) view of whole-mount 96hpf Alcian blue stain

(K-O) Dissected flat-mounted ventral and lateral (P-T) image of ventral cartilages

(U-Y) 40X image of the Meckel's cartilage lateral view. Length (L) calculated from the midline tip of the Meckel's cartilage to the middle of the imaginary line (width (W)) between the retroarticular processes. Scale = 50 µm.

Length/width (L/W) ratio of Meckel's cartilage was then measured (**Figure 18**A) to allow appropriate assessment of the cartilage elements. At 96hpf, wild-type (WT) embryos have a larger mean L/W ratio of 0.804 ± 0.019 which was statistically significant compared to *wls*, *wnt5b* and *gpc4* mutants; 0.566 ± 0.033, 0.447 ± 0.029, 0.542 ± 0.048 respectively (L/W ± standard deviation; $p < 0.01$ Kruskal-Wallis test with Dunn's multiple comparisons test; **Figure 18**B, D, E, P). We did not observe a statistical difference in *wnt9a* mutants (0.756 ± 0.104; n=10, $p = 0.125$) but a prominent open-mouth phenotype prompted us to examine differences in the cause of this phenotype across the Wnt mutants.

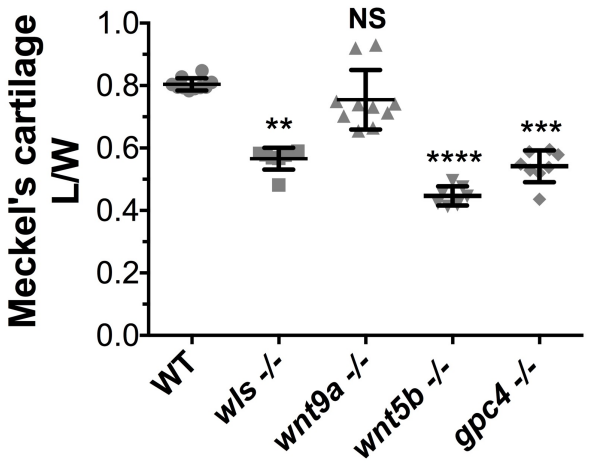

Figure 18. Meckel's cartilage length/width ratio

A clutch of 10 embryos imaged separately was used during calculation (**p<0.01, ***p<0.001, ****p<0.0001; Kruskal-Wallis test with Dunn's multiple comparison test. Significance level at p<0.05).

It is important to note that these morphological differences were not due to cell number differences, as chondrocyte count was not statistically significant amongst the different mutants (p = 0.1151, One-way ANOVA; **Figure 19**Q). These results, coupled with the gene expression data illustrate that Wnt signalling is essential for development of ventral craniofacial cartilages during zebrafish embryogenesis.

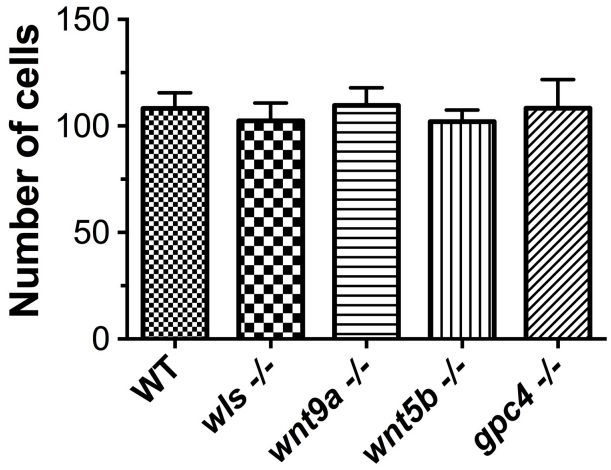

Figure 19. Number of cells from one-half of Meckel's cartilage

Numbers was counted from figures 2U-Y from 10 different embryos. No statistically significant difference in cell number across *wls*, *wnt9a*, *wnt5b* and *gpc4* (p=0.1151, NS; One-way ANOVA).

3.2.3 Cellular organization reveals two distinct zones in Meckel's cartilage: midzone and body

Now that we have established a significantly mishapened Meckel's cartilage in our Wnt mutants, we sought to understand the morphologic phenotype displayed by these Wnt gene mutants. To achieve this, we measured the L/W of Meckel's cartilage and the individual cell sizes during Meckel's cartilage morphogenesis at different time points. We performed live confocal imaging of each mutant using the Tg(*sox10*:GFP) line and tracked the L/W measurement from the earliest time Meckel's cartilage forms a distinguishable structure (55hpf) to the time point when the arch is fully formed (96hpf) (Eames et al., 2013) (**Figure 20**A-E).

By 55hpf in WT embryos, condensation of *sox10* positive cells are observed just anterior to the heart and appears to converge in the midline. At this stage, Meckel's cartilage has a L/W of 0.28 ± 0.01. By 60hpf, marked extension is observed with the midline protruding anteriorly and the arch of Meckel's cartilage begins to take its shape. By 72hpf, a distinct arch is observed with cells within the body of Meckel's cartilage starting to hypertrophy and form discs and stack above each other to aid within the elongation process. By 96hpf, Meckel's cartilage has a L/W ratio of 0.78 ± 0.10 and at this stage, cells within the midzone have stacked. We observed a period of accelerated extension occurring between 55-72hpf.

In *wls*, *wnt9a* and *wnt5b* mutants, the Meckel's cartilage appeared to extend at a similar rate between 55-60hpf but morphological defects in the Meckel's cartilage were evident in *wls* and *wnt5b* mutants at 72hpf (**Figure 20**F) where they appear to lose the global arch shape, and remain smaller. *gpc4* mutants displayed the slowest extension of Meckel's cartilage with defects observed as early as 60hpf (**Figure 20**E). Meckel's cartilage appears flattened throughout development and chondrocytes fail to form proper disc and stack, accounting for the alteration in global shape and size. Meanwhile, extension rate in *wnt9a* mutants appeared normal (**Figure 20**C) when compared to WT but obvious defects can be observed in the shape of Meckel's cartilage. *wnt9a* mutants formed a more 'V' shape, evident by 72hpf compared to the 'U' shape as seen in WT.

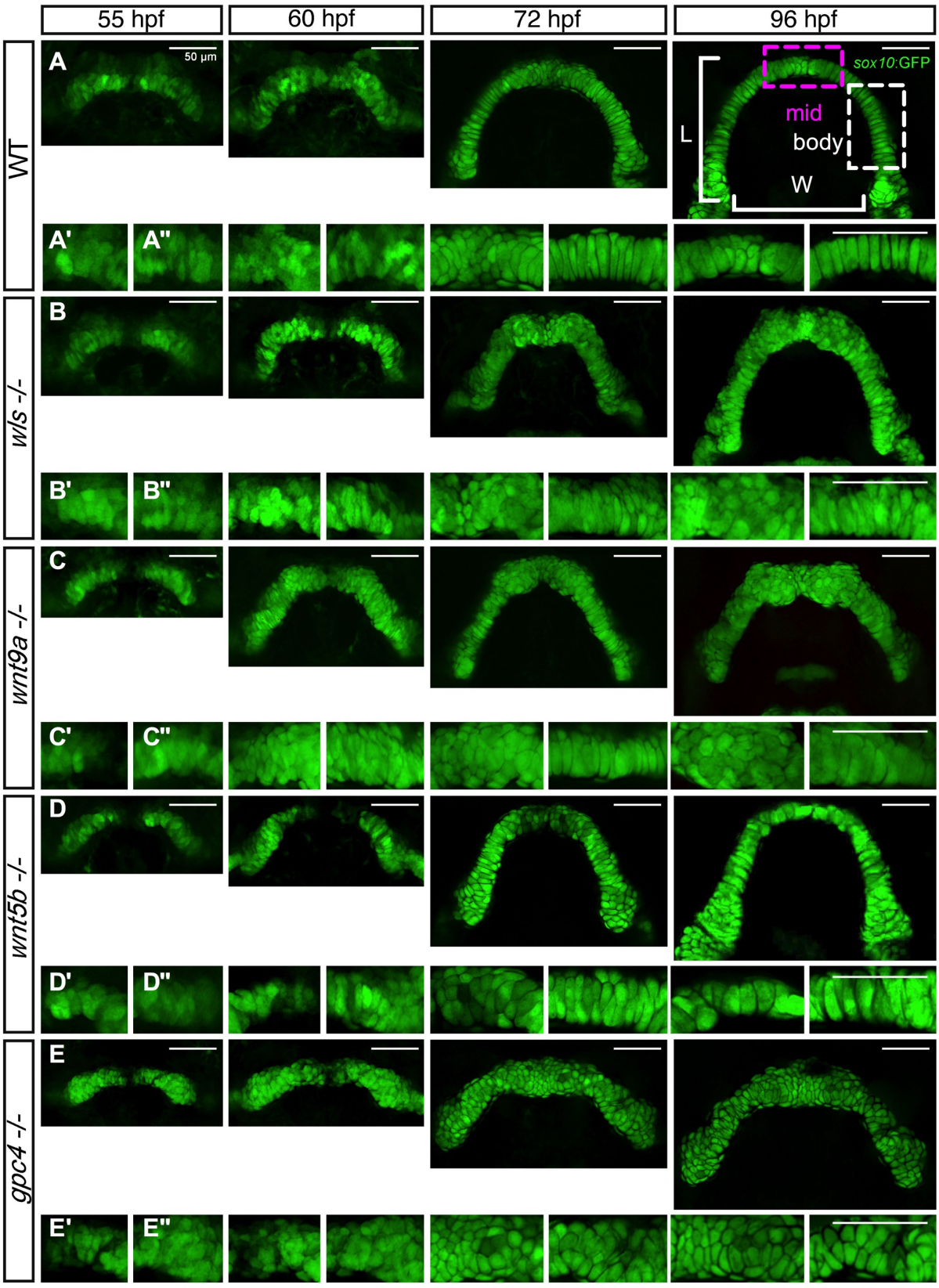

Figure 20. Time lapse imaging across various time points of Meckel's cartilage in *wls*, *wnt9a*, *wnt5b* and *gpc4* mutants

(A-E) Wnt mutants were crossed to Tg(*sox10*:GFP) transgenic line and homozygote embryos were imaged at difference time points starting at 55hpf when convergence of the Meckel's cartilage occurs until 96hpf when the arch is complete. X' 20X image of the Meckel's cartilage and X'' represents 20X image of the body of Meckel's cartilage.
Defects evident from 60hpf especially in *gpc4 -/-* and by 72hpf, obvious midline defect was seen in *wls, wnt9a* and *gpc4* and body defects apparent in *gpc4*. *wnt5b* exhibited a smaller cartilage size throughout morphogenesis.

In addition to altered global dimensions of Meckel's cartilage, we observed two morphologically distinct regions: the midzone (**Figure 20**A, 96hpf pink box) and the body (**Figure 20**A, 96hpf white box) that differed in cell size and organization. As observed in WT embryos by 72hpf, chondrocytes within the body were seen to stack (like coin discs) in a single cell layer. In contrast, chondrocytes within the midzone remained smaller, more cuboidal in shape and consist of multi layers. By 96hpf, cells within the midzone acquired a more columnar shape with a L/W of 2.53 ± 0.35 and stacked to align with cells within the body that have a L/W of 4.47 ± 0.56. This alignment completes the arch of Meckel's cartilage.

In contrast, *wls*, *wnt9a* and *gpc4* mutants display a different chondrocyte phenotype. Chondrocytes within the midzone at 96hpf did not align and the chondrocytes remained small and rounded with a L/W ratio of 1.31 ± 0.05, 1.36 ± 0.14 and 1.51 ± 0.25 respectively. Interestingly, *wls* and *wnt9a* mutants displayed more elongated cells within the body (3.74 ± 0.59 and 3.66 ± 0.34 respectively) compared with *gpc4* where cells within the body is significantly smaller and rounded (1.88 ± 0.24) (**Figure 21**A-C). In *wnt5b* mutant, there was some degree of alignment of the cells within the midzone but cells were also smaller compared to WT in both the midzone and the body (1.93 ± 0.33 and 2.90 ± 0.37 respectively) (**Figure 21**B, C). The analysis presented here suggests that there are two distinct morphologic zones in Meckel's cartilage that differ in cell shape, organization. It also suggests that these distinct zones have different responses to non-canonical Wnt signalling. As non-canonical Wnt signalling is important in cellular polarity, we then wanted to examine whether polarity differs within these zones.

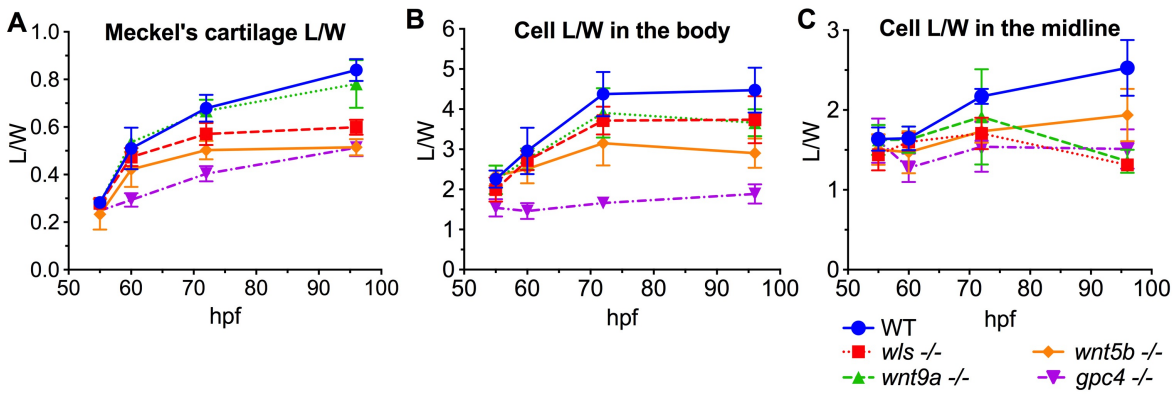

Figure 21. Global and cellular size differences between *wls, wnt9a, wnt5b* and *gpc4* mutants.

(A) L/W ratio of Meckel's cartilage of 5 different embryos were measured and plotted over time. *wls* (red), and *wnt5b* (orange) mutants showed defects from 72hpf onwards while defects in *gpc4* (purple) were evident from 60hpf and remained small throughout lower jaw morphogenesis. *wnt9a* (green) does not show any obvious Meckel's cartilage L/W defect compared to WT.

(B-C) Individual cell L/W ratio were measured and plotted over time from the body (B) and midzone (C) of Meckel's cartilage of 5 different embryos. Closer examination of the cell shape and size within Meckel's cartilage showed that cells within the body differ from the midzone area. *wls* (red) and *wnt9a* (green) both showed an almost similar cell L/W in the body compared to WT with a more cuboidal shape. *wnt5b* (orange) appeared overall smaller in L/W while *gpc4* (purple) remained smaller and rounder. In contrast, when the cells within the midzone were examined, *wls*, *wnt9a* and *gpc4* mutants all showed a significant size difference at 96hpf where cells remained small and round compared to WT.

3.2.4. Wnt signaling is required for chondrocyte polarity in Meckel's cartilage

Given the differential requirement observed for the chondrocyte morphology and organization between the midzone and body regions of Meckel's cartilage, we examined whether chondrocyte polarity is also disrupted differently between the *wls, wnt9a, wnt5b* and *gpc4* mutants. Cell polarity may hint towards cellular behaviour and interaction with extracellular cues during development Chondrocyte polarity was visualized using acetylated-alpha tubulin to mark microtubule-organizing centres (MTOC) indicative of primary cilia, at 3.5dpf, a time point when all Wnt mutants displayed distinct abnormalities between the midzone and the body (**Figure 22**) (Sepich et al., 2011).

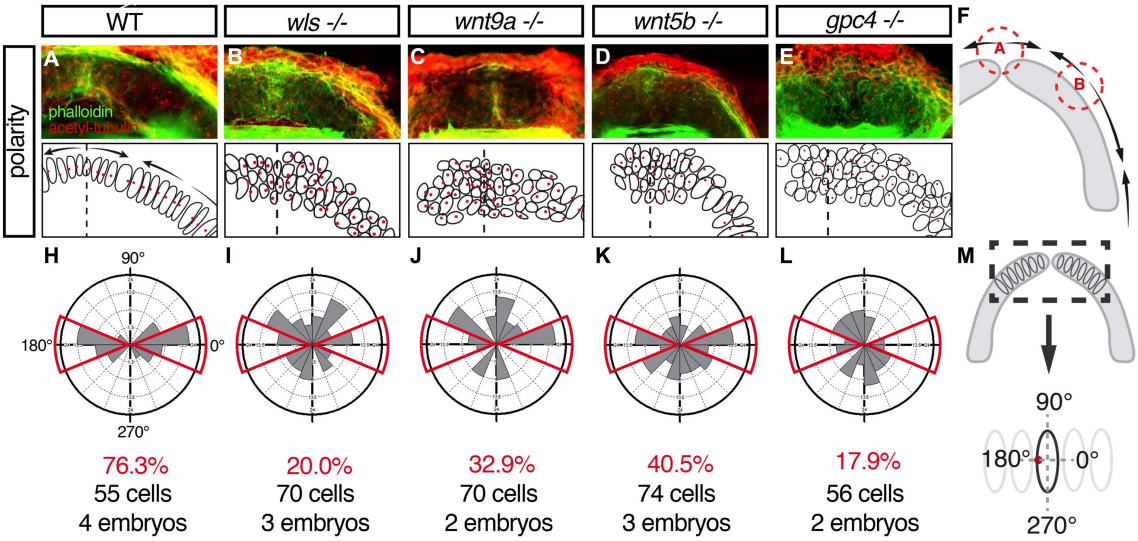

Figure 22. Cell polarity pattern within the midzone of Meckel's cartilage in *wls*, *wnt9a*, *wnt5b* and *gpc4* mutants.

(A-E) 72hpf WT and homozygote embryos were stained for actin with phalloidin (green) to delineate cell membranes and acetylated-tubulin (red) to reveal microtubule organizing centres (MTOC).

(F) Polarity pattern for Meckel's cartilage at 72hpf showing 2 inflection points; A and B; point A where the hemi-Meckel's cartilage meet in the midline and point B within the body of each hemi-Meckel's cartilage.

(H-L) Rose plots of cell polarity as indicated by MTOC measured from cells within the midzone portion of Meckel's cartilage. Red box indicates the expected distribution of the MTOC that is observed to be positioned in a narrow area along the x-axis; proximal (0°) and distal (180°). (M; black dotted box). Scale = 50µm.

In WT embryos, the primary cilia were aligned to the centre of the cell following the curve of the Meckel's arch. In addition, cell polarity staining revealed three apparent zones of uniform polarity with 2 inflection points of the primary cilia (A and B) (**Figure 22**F). Point A was observed to be at the anterior midline and Point B was located at a position that has

been observed to provide musculoskeletal attachment and pre-osteoblast condensation (**Figure 22**A, F). In contrast, all Wnt mutants displayed disorganized primary cilia arrangements in the midzone resulting in a malformed midzone and loss of the Meckel's cartilage arch shape (**Figure 22**B-E). In all mutants, chondrocyte polarity appeared randomized and we were unable to localize points A and B.

We then measured the angle at which the MTOC were positioned within the midzone of Meckel's cartilage (**Figure 22**H). In WT embryos, 76.3% of cells had primary cilia oriented in a narrow distribution along the x-axis in the proximal (0°) and distal (180°) directions (red boxes, **Figure 22**H). This distribution pattern was lost in all Wnt mutants as their chondrocytes localized primary cilia were randomly positioned without restriction about the X-axis (**Figure 22**I-L).

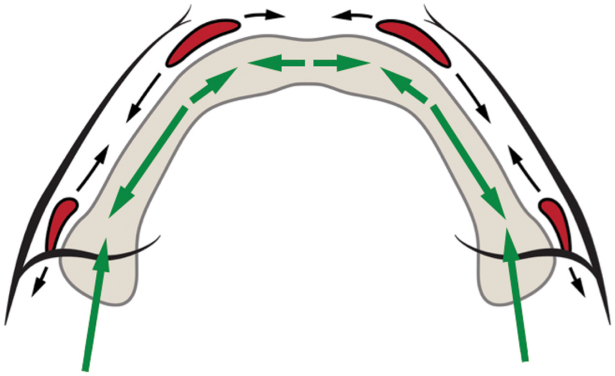

Figure 23. Cell polarity summary of Meckel's cartilage and direction of bony ossification
The figure represents a ventral view of Meckel's cartilage in beige, mental nerve in black, ossification centers in red (dentary anteriorly). The green arrows represent the direction of MTOC within chondrocytes and the black arrows represents the direction of ossification

We then observed that the anatomic location of point B coincides with the first ossification point of the dentary bone as well as mesenchymal condensation (**Figure 22**, **Figure 23**). Therefore, we next examined how loss of chondrocyte polarity affects other craniofacial structural features to shed insight into whether the underlying Meckel's cartilage development influences mandibular ossification.

3.2.5. Wnt is required for timely bone ossification

Given that cartilage structures constitute a scaffold that prefigure for ventral skeletal ossification, we studied how the loss of polarity and cartilage defects affected bone

development in *wls, wnt9a, wnt5b* and *gpc4* mutants. Early bone development occurs as early as 3dpf in zebrafish, permitting analysis of ossification events in *wls*, *wnt9a*, *wnt5b* and *gpc4* mutants that typically survive until 12-15dpf (Bird and Mabee, 2003). Bone phenotype at two time points were compared to ascertain the dynamic changes of ossification: 1) 4dpf when cartilage elements have established their structures and 2) 8dpf when most craniofacial bones (both intramembranous and endochondral) have initiated ossification, evidenced by Alizarin red staining.

At 4dpf, WT embryos started to develop intramembranous bones (red in **Figure 24**U diagram); dentary, branchiostegal rays, opercle, and cleithrum (**Figure 24**A). By 8dpf, the endochondral bones (orange **Figure 24**U); ceratohyal, mentomeckelian, retroarticular and ceratobranchial-5 initiated ossification and the previously noted intramembranous bones enlarge (**Figure 24**F). The positions of these bones correlated to the transgene expression of *osteocalcin*, a marker of mature osteoblast (green in **Figure 24**K) and *osterix*, a marker of osteoblast (red in **Figure 24**P). Focusing on the mandible, the dentary, mentomeckelian and retroarticular bones will all fuse at a later stage and a shorter Meckel's cartilage remains within the core of the ossified mandible. Comparing the bony development to the Wnt mutants, we found significant defects.

In *wls* mutant, only the opercle and cleitrium formed at 4dpf and this remained unchanged at 8dpf (n=25), arguing against developmental delay as we would expect more bones to have started to develop between these two-time points as observed in WT. The lack of ossification phenotype correlated with the loss of bone specific transgene expressions: *osteocalcin* (green in **Figure 24**L) and *osterix* (red in **Figure 24**Q). It is important to note that larvae at 8dpf were examined from confocal stacks in WT and mutants in the Tg(*ocn*:GFP;*sox10*:mCherr)y and Tg(*osx*:mCherry;*sox10*:GFP) reporter backgrounds, where it is clear that the Meckel's cartilage is developed but dysmorphic, providing additional morphologic data to support that the lack of ossification is not due to developmental delay. These results suggested that osteoblasts not only failed to secrete bone matrix as detected by Alizarin red stain, but also failed to differentiate into mature osteoblast in the *wls* mutant. Despite the opened mouth phenotype in *wnt9a* mutants, all intramembranous bones formed appropriately at 4dpf (**Figure 24**C) and enlarged like WT embryos by 8dpf (**Figure 24**H). *wnt5b* mutant also displayed a similar appearance of larval cranial bone elements as *wnt9a* mutant (**Figure 24**D, I, N, S). However, for both *wnt5b* and *wnt9a* mutants, many defects were seen within endochondral bones; mentomeckelian (n=0/18 and n=0/11), retroarticular (n=4/18 and n=0/11), ceratobranchial 5 (n=0/18 and

n=1/11) and ceratohyal bones (n=7/18 and n=6/11) (summary in graph; **Figure 24**AA). Expressions of *osterix* and *osteocalcin* expression in *wnt5b* and *wnt9a* mutants indicated a reduction in the number of mature osteoblast compared to WT in structures where endochondral bone occurs (**Figure 24**M, N, R, S). High-resolution images of Alizarin red staining in WT reveals a thin, flat perichondral bone, termed the mentomeckelian that is distinct from the thicker dentary bone (**Figure 24**K). A clear boundary at 8dpf helps differentiate the two bones, allowing quantification and analysis. *wnt9a*, *wnt5b* and *gpc4* all lack the mentomeckelian despite staining for the dentary (**Figure 24**M-O). *wls* completely lacks both the dentary and mentomeckelian (**Figure 24**L). Double transgenic line with *sp7*:GFP and *sox10*:mCherry at 8dpf shows a perichondral cell expressing *sp7* (**Figure 25**). This cell is observed directly adjacent to the perichondral cells as oppose to the *sp7* positive cells of the dentary lying above the perichondrium. In *gpc4* mutant, a similar bone phenotype as *wls* mutant was observed at 4dpf with only the opercle and cleithrum present. Interestingly, despite a more severe Meckel's cartilage shortening, all intramembranous bone formations were detected by 8dpf in *gpc4* mutants (**Figure 24**E). This correlated with the detection of *osterix* and *osteocalcin* transgene expressions (**Figure 24**J, O). However, like *wnt9a* and *wnt5b* mutants, defects were observed by the absence of endochondral bone in all *gpc4* mutant embryos imaged (n=12;

Figure 24Q). In addition, no endochondral bone developed in *gpc4* even when observed at 8dpf.

Taken together, these results showed that *wls* is required for both intramembranous and endochondral ossification while *wnt9a, wnt5b* and *gpc4* are required only for endochondral ossification as evident by the loss of differentiation of ventral chondrocytes to osteogenic progenitors. In addition, ossification can occur despite significant Meckel's cartilage dysmorphology as seen in *gpc4* mutant. When *wls* requirement for ossification is considered in the context of intramembranous ossification that are present in *wnt9a* and *wnt5b* mutants, it is likely that other ligands that requires *wls* for secretion are important for direct osteogenesis from NCC progenitors.

Discovering the bony defects in our Wnt mutants we then sought to elicit why these defects come about. We then considered whether the cartilage joint (jaw and hinge joints) plays a role in providing the chondrocyte defects as this was previously thought to be the growth centres of the mandible. Additionally, we examined whether muscle structure contributes to these defects.

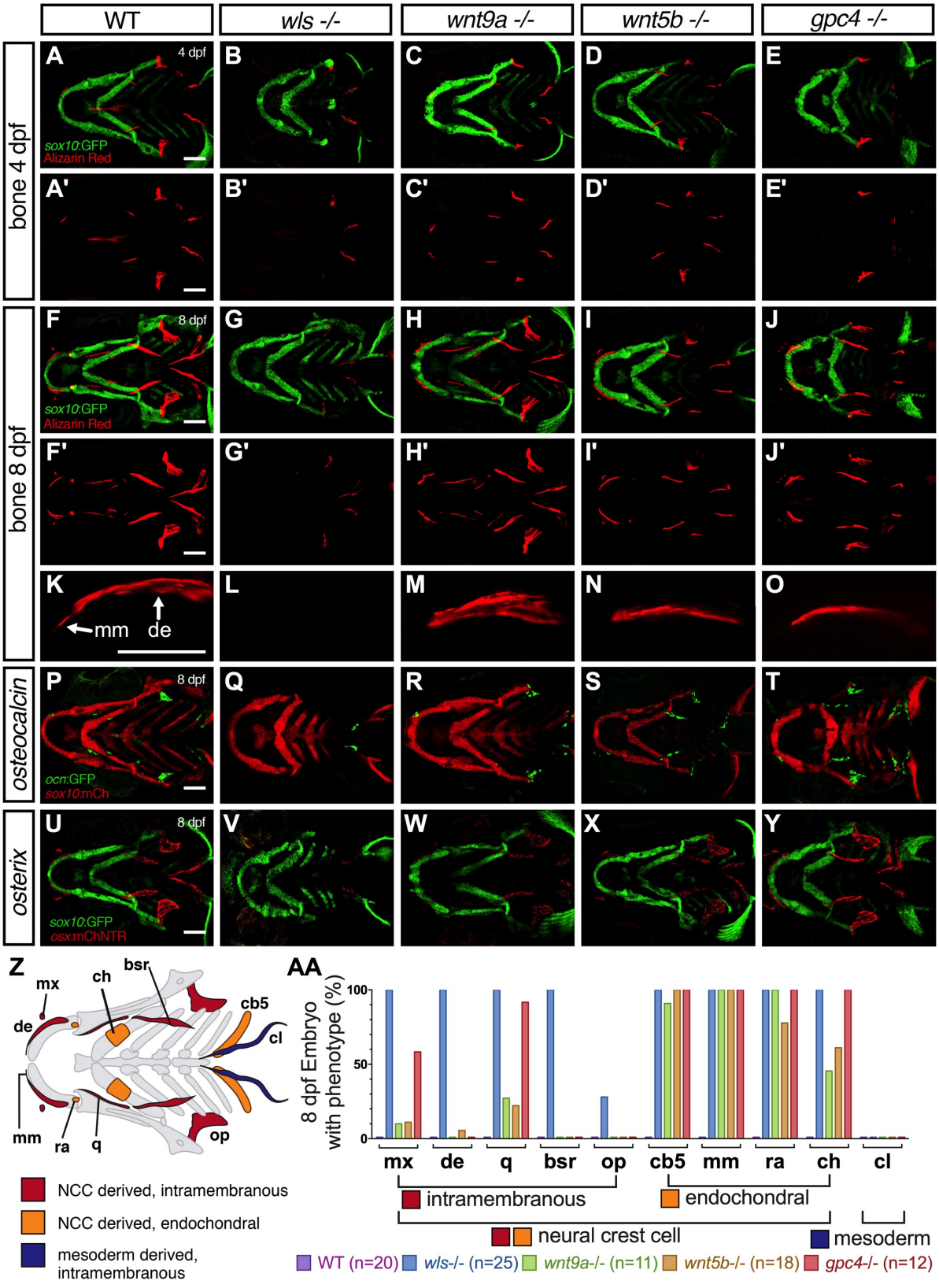

Figure 24. Bone defects in *wls*, *wnt9a*, *wnt5b* and *gpc4* mutants.

(A-J) Maximum intensity projections of live confocal imaging stacks of 4dpf (A-E) and 8dpf (F-J) Wnt homozygotes in Tg(*sox10*:GFP) background stained with Alizarin Red S.

(K-O) 40X confocal maximum intensity projections of alizarin red stain focusing on the dentary bone (de) and mentomeckelian (mm). The mentomeckelian is a flatter bone attached to the distal end of the dentary that is thicker and broader.
(P-T) Confocal maximum intensity projections of *osteocalcin* transgene expression in Wnt mutants in a Tg(*sox10*:mCherry) background.
(U-Y) Confocal maximum intensity projections of *osx* transgene expression in Wnt mutants in a Tg(*sox10*:GFP) background.
(Z) Graphical map of neural-crest cell (NCC)-derived bone (red; intramembranous ossification and orange; endochondral ossification) and mesoderm derived bone (blue). Dentary (de), retroarticular (ra), quadrate (q), ceratohyal (ch), branchiostegal rays (bsr), opercle (op), ceratobranchial 5 (cb5), cleithrum (cl).
(AA) Percentage of mutant with bony phenotype of different bones in the craniofacial region where 100% indicates that all mutant embryos do not have that bone. Scale = 50μm.

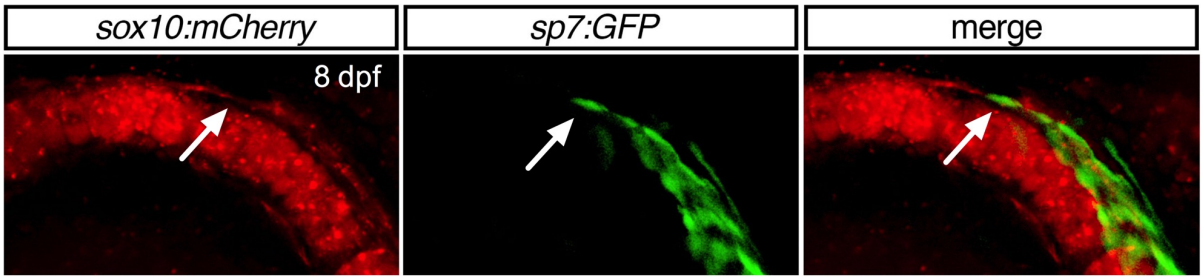

Figure 25. *Osterix*-expressing cells in 8 dpf WT embryos.
40X Confocal maximum intensity projection images of 8 dpf Meckel's cartilage. Osterix expressing cells are observed at the position of the dentary adjacent to the body of Meckel's above the perichondrium. A single osterix-expression cell (arrow) is observed at the level of the perichondrium indicating the differentiation of perichondral cells to osteoblast to form the future mentomeckelian perichondral bone.

3.2.6. Cartilage joint and muscle defects in wls, wnt9a, wnt5b and gpc4 mutants

In addition to cartilage formation, shaping the craniofacial structures requires properly formed joints and muscles. In zebrafish, the jaw and hinge joints are the two major joints in the craniofacial region. We examined the retroarticular and coronoid process of Meckel's cartilage that articulates with the palatoquadrate to form the jaw joint and the interhyal that forms a sesamoid-like bone between the ceratohyal and hyosymplectic.

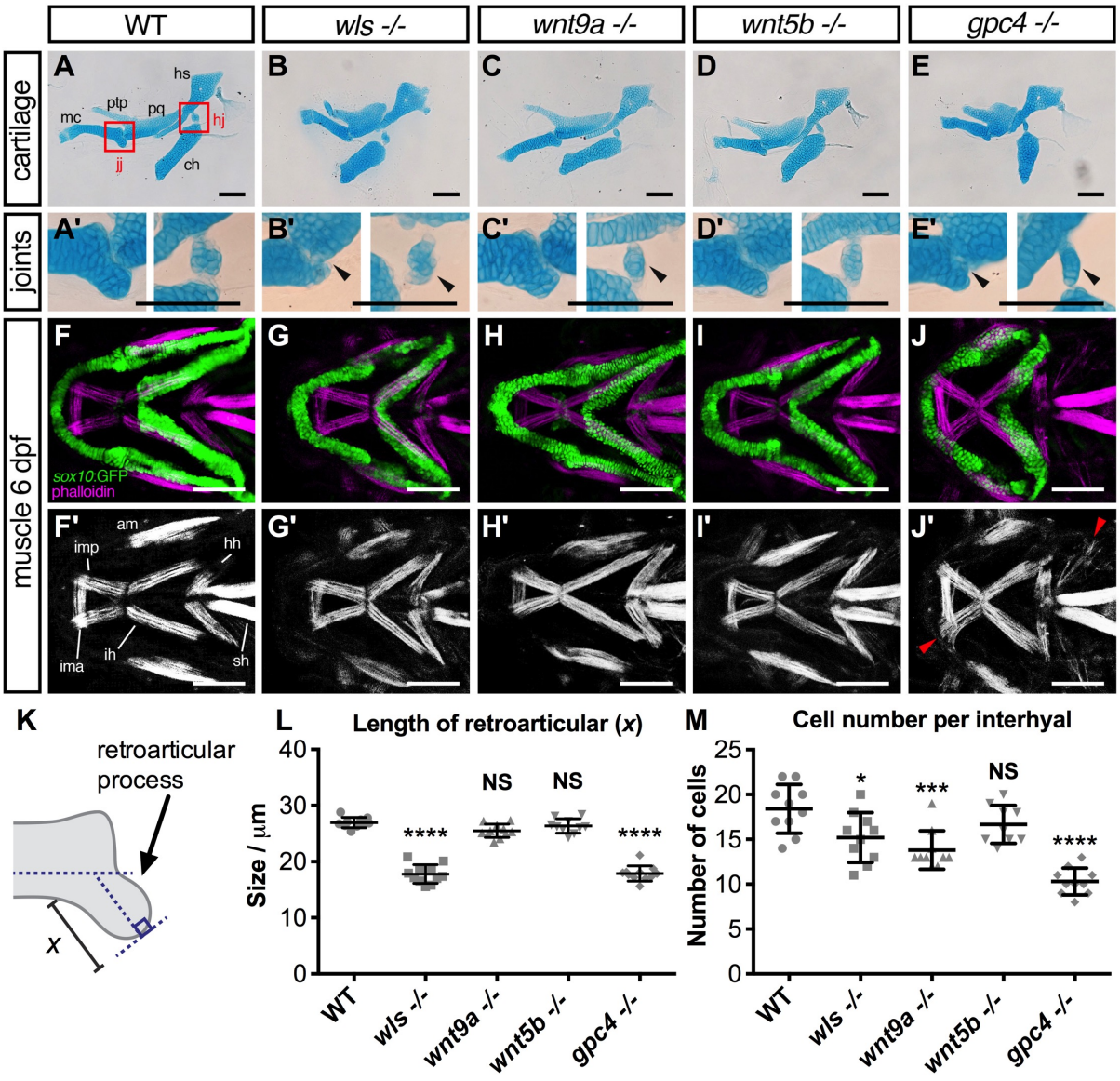

Figure 26. Joint and muscle defects in *wls*, *wnt9a*, *wnt5b* and *gpc4* mutants.

(**A-E**) Alcian blue stained ventral cartilage lateral whole-mounts of 8 dpf embryos and 40X zoomed image in **A'-E'** of the jaw joint (jj; left) and hinge joint (hj; right). Meckel's cartilage (mc), pterygoid process (ptp), palatoquadrate (pq), hyosymplectic (hs), and ceratohyal (ch). Jaw joint defects evident in *wls* and *gpc4* mutant whilst *wnt9a* exhibited a slightly malformed retroarticular process. *wls* displayed a clump of cells within the hinge-joint compared to the neatly stacked layered chondrocytes in wild-type. In contrast, *wnt9a, wnt5b* and *gpc4* were only a single cell layer in thickness

(**F-J**) Maximum intensity projections of 20X zoom confocal stacks showing muscle stain with phalloidin (purple) and anti-GFP (green) for cartilage elements. Muscle length defects apparent in all *Wnt* mutants with *gpc4* displaying disorganized intermandibularis posterior (imp) invading the gaps in Meckel's cartilage. Adductor mandibulae (am), intermandibularis anterior (ima), intermandibularis posterior (imp), hyohyoideus (hh), interhyoideus (ih), sternohyoides (sh) F'-J'' Single channel phalloidin fluorescence.

(K) Graphical representation of retroarticular measurement

(L) Measured length of retroarticular process and **(M)** cell count per interhyal in WT and Wnt mutants of 10 embryos per mutant line. (*p<0.01 ***p<0.001, ****p<0.0001; Kruskal-Wallis test with Dunn's multiple comparison test. Significance level at p<0.05). Scale = 50μm.

For the interhyal bone, alcian blue staining at 8dpf shows a two-cell layer structure attached by ligaments to the palatoquadrate and the ceratohyal, forming a rounded sesamoid-like cartilaginous structure. The magnified view showed that in *wls*, *wnt9a* and *gpc4* mutants, there is a significantly reduced number of chondrocytes within the interhyal bone at the hinge joint (**Figure 26**B'-E' right). In addition, the retroarticular process in *wls* and *gpc4* mutants were significantly malformed and shortened (**Figure 26**L) compared to WT ($p < 0.0001$ for both). Even though there was no evidence of fusion of the cartilage structure, chondrocytes within the interhyal were more rounded and not properly stacked in *wls* mutants. *wnt9a*, *wnt5b* and *gpc4* mutants displayed a single-cell layer thick interhyal bone. While functional assessment of the joint has not been examined, we theorized that this defect would impinge on ventral cartilage movement during respiration. For the Meckels-palatoquadrate joint (jaw joint), the retroarticular process and coronoid process forms a disc to accommodate the palatoquadrate process. In *wls* and *gpc4* mutants, the retroarticular processes were malformed and shortened indicating a defect in jaw joint which may perturb mouth opening. Interestingly, we did not observe any overt jaw joint defects in *wnt9a* considering the opened mouth phenotype nor in *wnt5b* mutants.

Due to evidence highlighting the role of muscles in maintaining joint integrity, the craniofacial muscles in our Wnt mutants were observed (Shwartz et al., 2012). For this, we stained Wnt embryos in *sox10*:GFP background with phalloidin (**Figure 26**F-J). The staining revealed that *wls* and *wnt5b* mutants have normal muscle appearance and pattern, although both exhibited some muscle shortening potentially secondary to the craniofacial cartilage dysmorphologies (**Figure 26**G - I). Interestingly *wnt9a* mutants did not appear to have any muscle defects, which was surprising since we expected that muscle defects would affect mouth opening. The most severe muscle defect was observed in *gpc4* mutant where the intermandibularis posterior muscle that normally attaches to the Meckel's cartilage appeared disorganized and invaded ectopic gaps between the chondrocytes (**Figure 26**J, red arrows). The muscle defect in *gpc4* mutant may explain the more severe Meckel's cartilage length/width ratio and cell shaped compared with *wls* mutant. These data also suggest that cranial muscles were properly patterned in *wls*, *wnt9a,* and *wnt5b* mutants and they do not contribute to the cartilage morphology phenotypes. It also

suggests that Wnt mutants may have a greater effect on NCC-derived tissues since the craniofacial muscles are head paraxial mesoderm-derived.

3.2.7. Loss of wls leads to decrease chondrocyte proliferation

Our data showed that abrogation of the Wnt signalling led to Meckel's cartilage malformations and that *wls*, *wnt9a*, *wnt5b* and *gpc4* have distinct roles in shaping the ventral cartilage structures. For endochondral bone formation, following condensation of NCC cells to sites of future skeletal structures, subsequent proliferation of chondrocytes is key for their expansive linear growth and enlargement. Therefore, we wanted to determine on a cellular level whether growth through proliferation is affected in our Wnt mutants. To achieve this, chondrocytes undergoing mitotic division were assayed with BrDU in 6dpf mutants to determine if Wnt mutants also affect chondrocyte proliferation. We assayed at 6dpf as this is the time point in previous studies when chondrocytes start dividing to extend the jaw (Eames et al., 2013).

In WT larvae, chondrocytes at 6dpf were noted to be actively proliferating in Meckel's cartilage and the surrounding mesenchyme, consistent with previously report findings in zebrafish (**Figure 27**A) (Hammond and Schulte-Merker, 2009). However, chondrocyte proliferation was severely affected in *wls* mutants ($p<0.0001$; **Figure 27**B) compared to *wnt9a*, *wnt5b* and *gpc4* mutants. Since proliferation was decreased in *wls* mutants at 6dpf, we examined if NCC condensation surrounding Meckel's cartilage at 60hpf was also affected. We found no difference in positive BrDU cell in *wls* mutants compared to WT (**Figure 28**). Moreover, 96hpf *wls* mutant embryos had the same number of cells within Meckel's cartilage (**Figure 27**L, Q) indicating that *wls* has a more important role later in chondrocyte proliferation, maturation and differentiation for endochondral ossification. The data also suggest that *wnt9a*, *wnt5b* and *gpc4* are dispensable for chondrocyte proliferation but may be required later in chondrocyte maturation.

Given that proliferation defect may be associated with cell survival, we next performed live acridine orange assay to visualize cell apoptosis. There was no increase in the number of apoptotic chondrocyte or mesenchymal cells in *wls* mutant to account for the severity of the bone phenotype displayed (**Figure 27**C, D).

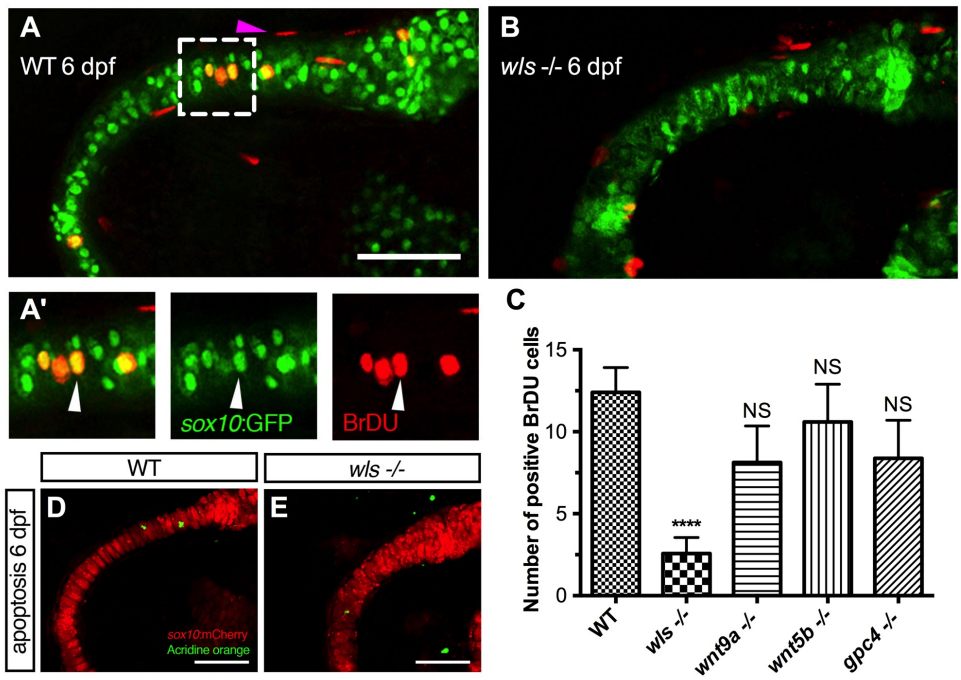

Figure 27. Chondrocyte proliferation defect in *wls* mutant precludes differentiation defects

(A, B) Representative BrDU assay confocal stacked image in WT 6dpf (A) and *wls* -/- (B) embryo with zoomed views of WT BrDU (red) colocalizing with chondrocytes (A') in the Meckel's cartilage (green). Arrowhead points to a representative chondrocyte that expressed both *sox10* and BrDU and used for quantification

(C) Quantification of BrDU positive cells in Wnt mutants taken from 5 different embryos per mutant line and imaged separately. Proliferation significantly differed in *wls* -/- compared to WT (****p < 0.001; Kruskal-Wallis test and Dunn's multiple comparison test, NS = not significant)

(D, E) No difference in chondrocyte apoptosis as showed with Acridine orange live staining at 6dpf in *wls* -/- . Scale = 50µm

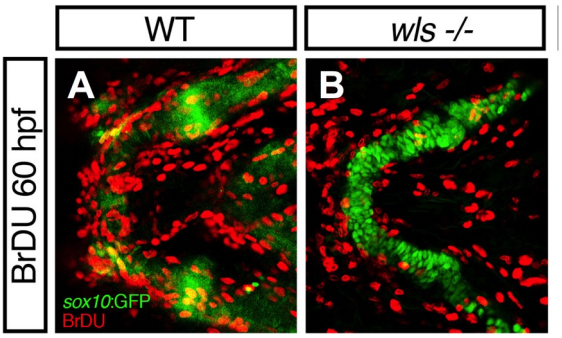

Figure 28. No difference in cell proliferation between WT and *wls* mutants at 60hpf.

Maximum intensity projections of confocal Z-stacks for BrDU assay in WT larvae *sox10*:GFP at 60hpf (A) and *wls* -/- (B)

These data suggest that the gross shortening of Meckel's cartilage in mutants is not due to cell death in chondrocytes or surrounding tissues. However, these works seem to point

towards the requirement of Wnt signalling for late proliferation of chondrocytes in Meckel's cartilage but not for cell survival. Indeed, mesenchymal expression of *wls* is necessary for the expansion and differentiation of chondrocytes to enable growth of Meckel's cartilage (Rochard et al., 2016). The data underlines the spatiotemporal regulation of Wnt signalling in ventral cartilage development.

3.2.8. Endochondral ossification requires non-canonical Wnt

To examine downstream effects of Wnt pathway perturbations, WISH analysis was performed in 4dpf embryos to examine the key steps of chondrogenesis (*sox9a*), extracellular matrix remodelling (*col2a1, col10a1a, col1a2*), osteoblast differentiation (*runx2a*) and joint patterning (*bapx1*) (Flores et al., 2004, Miller et al., 2003, Eames et al., 2012, Yan et al., 2002, Schilling and Kimmel, 1997). WISH images are presented in **Figure 29** and summarized in Table 16.

By 4dpf, *sox9a* expression, a key gene in chondrocyte differentiation, was observed throughout the ventral cartilages with increased expression at the distal edges of the cartilage elements. Normal *sox9a* expression was found in *wnt9a, wnt5b* and *gpc4* mutants (**Figure 29**A, C-E). However, *wls* mutant seemed to display enhanced *sox9a* expression throughout the craniofacial structures (**Figure 29**B). Since *sox9a* is necessary for *col2a1* expression (Yan et al., 2002), we examined *col2a1* expression and found no overt difference in staining or ectopic expression across the different Wnt mutants (**Figure 29**F-J).

We then examined the expression of *col10a1a* that indicates the maturation step of hyaline cartilage chondrocytes. In contrast to tetrapods, zebrafish osteoblast has also been found to express *col10a1a* (Eames et al., 2012). At 4dpf, *col10a1a* expression was observed in most craniofacial NCC-derived osteoblast, mesoderm derived osteoblast (parasphenoid, cleithrum) and chondrocytes in the ceratohyal adjacent to the ceratohyal bone (**Figure 29**K). In *wls* mutant, only expression within the parasphenoid, opercle and cleithrum was observed (**Figure 29**L). A similar pattern was observed in *wnt5b* mutant (**Figure 29**N). However, *wnt9a* and *gpc4* mutants exhibited expression in many the facial osteoblast but loss of expression in the ceratohyal (**Figure 29**M, O).

To examine whether mineralization occurred in *wls*, *wnt9a*, *wnt5b* and *gpc4* mutants, we looked at *col1a2* expression patterns that is expressed in mineralized bone and perichondrium, tendons and epidermis but not the chondrocytes (Eames et al., 2012). At 4dpf, *col1a2* expression was observed in the dentary, opercle and cleithrum, the only bones that stained for Alizarin red at 4dpf (**Figure 29**P) (Eames et al., 2013). No staining of the dentary was detected in *wls* or *wnt5b* mutants (**Figure 29**Q, S) but expression was present in *wnt9a* and *gpc4* mutants (**Figure 29**R, T). Meanwhile, tendon development appeared intact since the expression of *col1a2* in the sternohyoides tendon, palatoquadrate ligament, and intermandibularis posterior tendon appeared normal in all Wnt mutants.

runx2a (runt-related transcription factor) expression was then used to indicate osteoblast differentiation (Eames et al., 2004, Flores et al., 2004). By 4dpf, *runx2a* was expressed in all craniofacial dermal osteoblast as well as perichondral-osteoblast within the ceratohyal (**Figure 29**U). This marker was misexpressed in *wls* mutant but normal levels observed in *wnt9a*, *wnt5b* and *gpc4* (**Figure 29**V-Y).

Due to the joint defects observed in the Wnt mutants, we examined the expression levels of *bapx1* (*bagpipe*-related transcription factor), involved in joint specification (Miller et al., 2003, Nair et al., 2007). *bapx1* transcripts localized to the jaw joint (**Figure 29**Z), a pattern that is strongly expressed in *wls* and *wnt5b* mutants in addition to a smaller ventral midline domain (**Figure 29**AA black arrowhead) in the hyoid arch of *wls* mutants indicating a potential delay in joint specification (**Figure 29**AA, AC). Interestingly, jaw joint *bapx1* expression was completely lost in *gpc4* mutants indicating a failure in patterning the joint (**Figure 29**AD). *wnt9a* mutant showed a weaker expression that may indicate defective joint integrity (**Figure 29**AB).

In summary, in all *wls* mutants observed, we noted the enhanced expression of *sox9a* and *runx2a* with concurrent loss of *col10a1a* and *col1a2* expression. In *wnt9a*, *wnt5b* and *gpc4* mutants, there was a loss of *col10a1a* in endochondral bones. Altogether, our data showed a defect in the differentiation process of chondrocytes in the absence of Wnt signalling, a process required for its maturation and subsequent initiation of the endochondral ossification process.

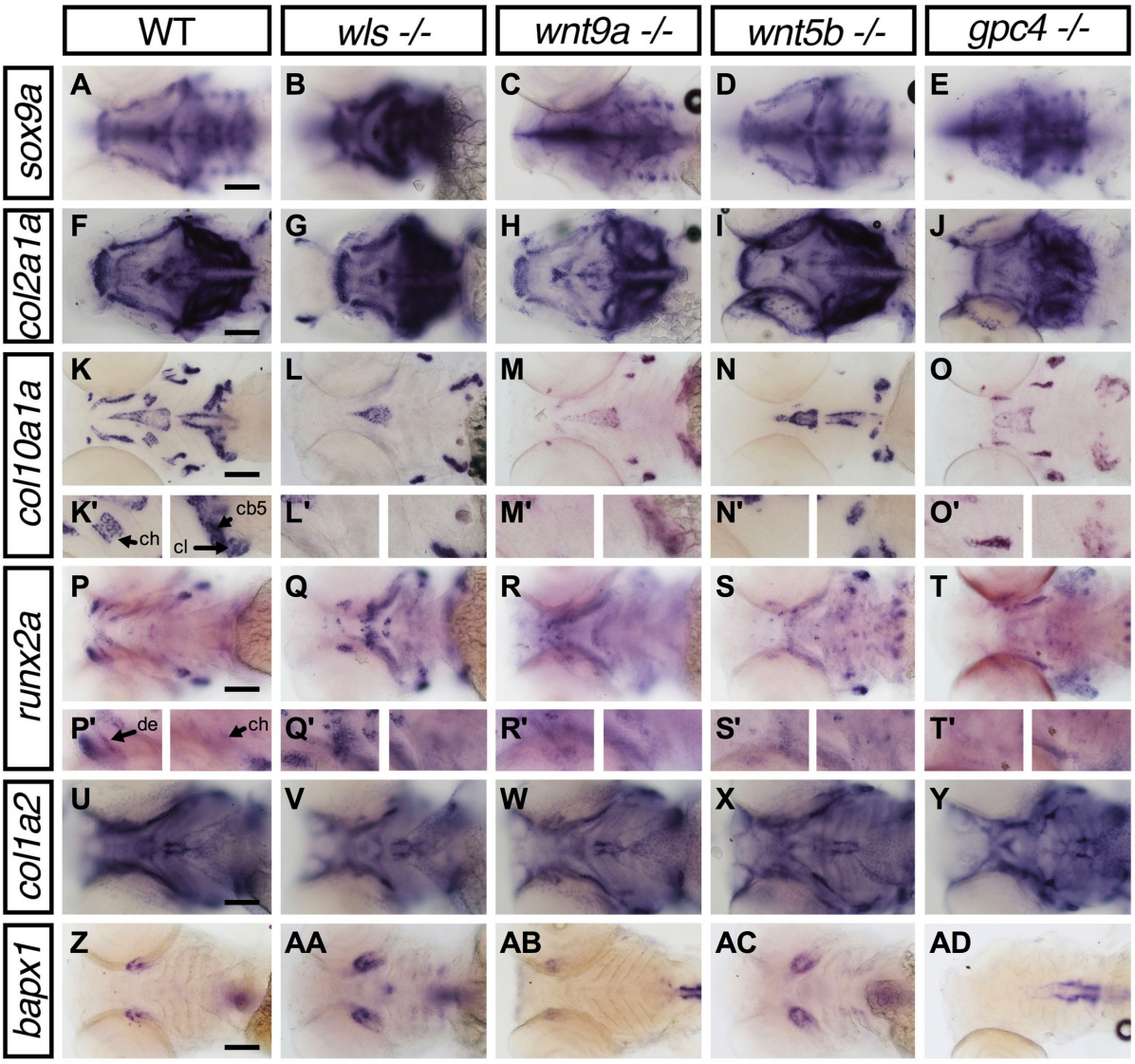

Figure 29. Lower jaw gene expression pattern of chondrocyte and bone markers in wls, wnt9a, wnt5b and gpc4 mutants.

Whole-mount RNA *in situ* hybridization of chondrocyte differentiation markers; *sox9a* (A-E) and chondrocyte matrix; *col2a1* (F-J). Hypertrophic chondrocyte marker; *col10a1a* (K-O), Bone and tendon marker; *col1a2* (P-T), osteoblastic progenitor marker; *runx2a* (U-Y) and joint marker; *bapx1* (Z-AD). Apparent increase in *sox9a, runx2a* expression pattern in *wls -/-* with concomitant loss of *col10a1a*. Arrow points to the position of Meckel's cartilage. Scale = 50 μm.

Table 16. Summary gene expression comparison within Meckel's cartilage

Markers in ventral cartilage structures		*wls -/-*	*wnt9a -/-*	*wnt5b -/-*	*gpc4 -/-*
Chondrogenesis	*sox9a*	++	+	+	+
ECM remodeling	*collagen type 2a1*	+	+	+	+
ECM remodeling	*collagen type 10a1a*	-	+	-	+
ECM remodeling	*collagen type 1a2*	-	+	-	+
Osteogenesis	*runx2a*	++	+	+	++
Joint patterning	*bapx1*	++	+/-	+	-

Qualitative scoring of whole-mount RNA *in situ* hybridization expression patterns compared with their WT sibling within a given clutch. Annotation: '++' = high detectable expression, '+' = normal expression, '+/-' = low detectable expression and '-' = undetectable expression.

Table 17. Summary gene requirements in ventral cartilage development.

Processes	*wls*	*wnt9a*	*wnt5b*	*gpc4*
Chondrocyte polarity and orientation	✔	✔	✔	✔
Chondrocyte proliferation	✔	×	×	×
Chondrocyte maturation/hypertrophy	✔	✔	✔	✔
Articular cartilage	✔	✔	✔	✔
Endochondral ossification	✔	✔	✔	✔
Intramembranous ossification	✔	×	×	×
Muscle	×	×	×	✔

✔ = required, × = not required

3.3. Discussion

Wnt signalling plays important roles in craniofacial cartilage and bone development. Once chondrocytes form distinct cartilage structures, differentiated chondrocytes can then either maintain their chondrogenic state to form articular cartilage or undergo hypertrophic maturation in the process of endochondral ossification (Kronenberg, 2003). The canonical Wnt/β-catenin pathway is key in promoting chondrogenesis, initiating chondrocyte hypertrophy and regulating osteogenesis (Day et al., 2005, Glass et al., 2005, Hill et al., 2005). The non-canonical pathways, both the PCP and Ca^{2+} have been shown to induce cytoskeleton reorganization, chondrocytes stacking and axial patterning (Fanto and McNeill, 2004, Le Pabic et al., 2014, Rochard et al., 2016, Sisson et al., 2015). Here we showed that *wls*, *wnt9a*, *wnt5b* and *gpc4* each have distinct requirements in chondrogenesis and osteogenesis during craniofacial ventral cartilage development.

3.3.1. wls, wnt9a, wnt5b and gpc4 are required for proper craniofacial cartilage and joint development

In ventral cartilage development, Wnt signalling is required for early CNCC induction and later in CNCC migration, specification and proliferation by participating in a gene regulatory network with *Edn1* and *Bmp* (Alexander et al., 2014). Heat-shock studies inhibiting Wnt through the overexpression of *dkk1, a Wnt* antagonist and *dntcf3,* a dominant negative form of the Tcf3 transcription factor, showed ventral patterning defects in the mandibular arch (Alexander et al., 2014). Recent studies using *Wls* to manipulate Wnt signalling, implicated its role in skeletal development by regulating osteogenesis and chondrogenesis (Maruyama et al., 2013, Zhong et al., 2012, Rochard et al., in press). In zebrafish, a previous study suggested that *wls* modulates *fgf3* expression to direct cell proliferation (Wu et al., 2015). We recently highlighted the importance of *wls* in mediolateral and dorsal-ventral patterning during palate morphogenesis (Rochard et al., 2016). Despite differences in upper and lower jaw development, we showed that *wls* affected ventral cartilage elements, like the ethmoid plate, where Meckel's cartilage appeared shorter and their chondrocytes were smaller and rounder. Cartilage analysis of *gpc4* and *wnt5b* mutants also recapitulated previously published work (Sisson et al., 2015). However, we noted that a later expression analysis of *gpc4* appeared in the tissues surrounding cartilage structures as opposed to an earlier expression found within the NCC and chondrocytes. This may suggest a more dynamic modulation of *gpc4* during craniofacial development as previously published by Sisson and colleagues (Sisson et al.,

2015) with earlier requirements in chondrogenesis and later in development of surrounding structures such as muscles.

When we examined cartilage structures at 8 dpf, we observed more profound articular cartilage phenotypes across our Wnt mutants with the loss of joint integrity and extension of the retroarticular process. Wnts have all been implicated in joint development through a role in articular cartilage formation (Hartmann and Tabin, 2001, Spater et al., 2006). In mice, *Wnt9a* has been shown to maintain joint integrity by suppressing chondrocyte differentiation within the joint interzones (Spater et al., 2006). *Wnt4* and *Wnt16* are also expressed in joints (Guo et al., 2004, Hartmann and Tabin, 2001) and mice double mutant *Wnt9a -/-;Wnt4 -/-* developed bony fusions and synovial chondroid metaplasia or acral bones(Spater et al., 2006). Here we showed that *wls* and *gpc4* displayed the most severe joint defects but through two different mechanisms. Both show opposite *bapx1* expression pattern with *gpc4* showing a complete loss and *wls* an exaggerated expression pattern. *bapx1* is a downstream target of *edn1*, specifying the jaw joint by shaping and maintaining articular cartilage through the activation of *chordin* and *gdf5* (Miller et al., 2003, Nakayama et al., 2004, Storm and Kingsley, 1999). The loss of expression in *gpc4* and the strong expression seen in *wls* may imply that either under or over-expression of *bapx1* can both result in jaw joint issues.

Studies from mouse model determined that mammalian *Wnt9a* loss-of-function mutation was lethal at birth (Spater et al., 2006). *Wnt9a* mutant embryos displayed partial joint fusion of the carpal and tarsal joints, shortened appendicular long bones. In contrast, they showed that ectopic activation of *Wnt9a* resulted in joint induction. We previously showed that zebrafish *wnt9a* morpholino knockdown resulted in the loss of ventral cartilage structures by affecting NCC migration (Curtin et al., 2011). Here, we found that *wnt9a* mutation is embryonic lethal as well but the phenotype appeared less severe than in mouse. Our *wnt9a* mutants develop craniofacial structures but were unable to close their mouth, an anteriorly displaced Meckel's cartilage, which resulted in an inability to feed properly. Interestingly, *wnt9a's* anteriorly displaced Meckel's appears very similar to the phenotype of the *spitzmaul*^{m636} mutant previously described in a large scale mutagenesis screen that has not yet been characterized (Neuhauss et al., 1996). Further analysis shows that cells within the midzone of Meckel's cartilage were smaller, rounder and less stacked compared to WT, suggesting a distinct midline anterior role of *wnt9a* in craniofacial development compared to other Wnt mutants. Additionally, we found that although *wnt9a* mutants have

a similar L/W of Meckel's cartilage and cell L/W in the body of Meckel's compared to WT, the cell L/W at the midline is disrupted and significantly smaller. This resulted in an elongated lower jaw that is abnormally arched due to the ventral displacement of Meckel's cartilage. Indeed, previous mutants with elongated lower jaw also displayed a ventrally displaced ceratohyal, such as the *doolittle*^{m636} mutant resulting in abnormal mastication and respiration (Neuhauss et al., 1996). While we have not directly assessed for movement of the lower jaw, we observed distinct patterning differences of the interhyal in *wnt9a* and together, with low *bapx1* expression levels in *wnt9a* mutants, we believe that joint integrity may explain this malocclusive jaw phenotype that plays a crucial role in feeding.

3.3.2. Shaping Meckel's cartilage by Wnt

For proper shaping and patterning of Meckel's cartilage, chondrocytes must first undergo convergence, intercalation, elongation and proliferation. Thereafter, cells are required to align, stack and polarize to maintain the organ structure. Previous work done in the laboratory focused on palate development in the context of cleft lip and palate disorders. Using lineage tracing and photoconversion experiments with the *sox10*:kaede line, it was shown that: first, the ethmoid plate in zebrafish is a homologous structure to the hard/primary palate of mammals and second, that the development of the palate undergoes distinct steps whereby the lateral maxillary prominences converge with the middle frontalnasal prominence (Dougherty et al., 2013, Dougherty et al., 2012). Thereafter, chondrocytes are seen to intercalate with each other and then soon after begin elongating to extend the palate further. Failure in the convergence of the prominences has been shown to result in clefting defects (Rochard et al., 2016). Like the ethmoid plate in zebrafish, the Meckel's cartilage and the ventral cartilage structures are also seen to undergo a similar development process. It has been documented that the condensation of NCC around the future lower jaw can be seen at around 55hpf where the two hemi-Meckel's cartilage fuses in the midline. Thereafter, the cells within the body of Meckel's cartilage stack like "disc of coins" to extend the lower jaw further. However, we have been interested in how the lower jaw acquires its unique shape and how cells behave.

Our study identified two regions within Meckel's cartilage with distinct cell behaviours; the midzone and the body. In all our Wnt mutants, the cells within the midzone remained smaller and rounded throughout cartilage development. This affected the shaping and length of Meckel's cartilage. When we analysed cell polarity within this midzone, we

found that in our Wnt mutants, cells in the midzone were disorientated and lose the directional polarization we observed in WT. Our study extended the polarity map of Le Pabic et al. and found that these opposing points of polarity (Points A and B, **Figure 22**) is what gives Meckel's cartilage its unique arched shape and rounded midline pattern (Le Pabic et al., 2014). When polarity is lost, as in our Wnt mutants, the Meckel's cartilage remains shortened and misshapen.

Interestingly *gpc4* displayed the most severe Meckel's cartilage with rounded cells observed in the midzone and body. We reasoned that the intermandibularis posterior muscle defect prevented cell intercalation and extension. Indeed, previous studies on chemically paralyzed mice, chick and zebrafish showed defects in cell convergence-extension and intercalation (Kahn et al., 2009, Nowlan et al., 2008, Shwartz et al., 2012). However, *wls* mutation did not recapitulate the *gpc4* mutant phenotype with some degree of stacking within the body of Meckel's cartilage and less severe AP shortening. One reason as argued before could be due to the defective muscle phenotype. Another hypothesis could be that *gpc4* integrates several other signalling pathways. Therefore, *gpc4* mutant phenotype could be a consequence of the loss of several other signalling pathways and not just Wnt signalling alone (e.g. Fgf), while *Wls* to date has only been shown to be necessary for the secretion of some Wnt proteins. There is also the existence of possible Wls-independent Wnt secretion that may contribute to Wnt signalling and result in the less severe phenotype compared to *gpc4*.

In this section, I eluded to the role of muscles in craniofacial development. While I have not explored it in greater detail, an interesting project might uncover the role of mechanosensing and tension in maintaining the arch of Meckel's cartilage as well as the integrity of the ventral cartilage structures. Below is an illustration of the ventral cartilage structures (**Figure 30** in thick black lines) and muscles/ tendons/ ligaments (in thin black lines). The intermandibularis anterior provides tension to keep the arch narrower anteriorly (**Figure 30**, red arrows) while the intermandibularis posterior and interhyoideus provide traction to allow movement of the lower jaw (for mastication) as well as the ceratohyals (for respiration) (blue arrows). The large adductor mandibularae, as its name suggests, helps with the adduction of the posterior ventral cartilage structures during respiration but at the same time, probably aid with limiting lateral growth of the structures and directing the chondrocyte proliferation towards the midline and anteriorly. This overall interplay of muscles allows the Meckel's cartilage to maintain its arch with an overall growth in a

catenary curved manner (green arrows). Therefore, it comes as no surprise that muscle paralysis or hypotonia in patients may result in micrognathia (Kahn et al., 2009, Shwartz et al., 2012). In fact, a mutation in *CAPZB*, an actin-caping protein resulted in a patient with micrognathia (Mukherjee et al., 2016).

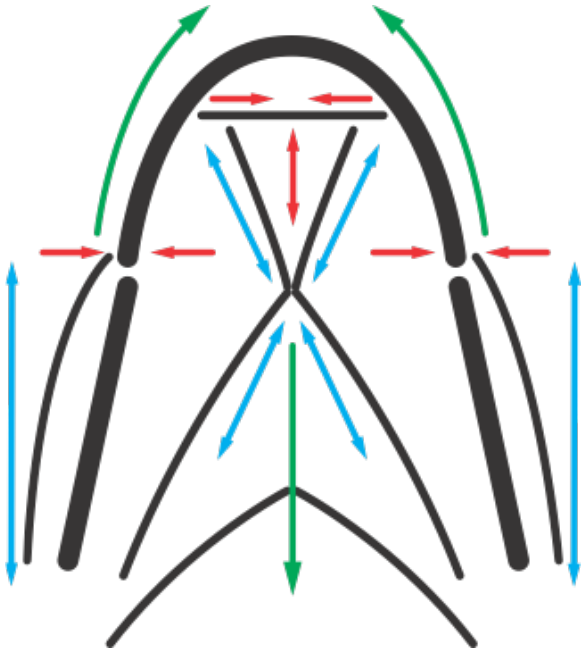

Figure 30. Diagram of potential forces imparted by craniofacial muscles to help shape ventral cartilage structures.

Thick black lines represented the cartilage structures. Thin black lines represent muscles/ligaments/tendons. Red arrow represents the forces acting on Meckel's cartilage to maintain the arched shape. The blue arrows represent the forces the muscle potentially creates. Green arrows represent the overall force directions to aid in the extension of the face.

Another idea regarding the midzone of Meckel's cartilage is that this area acts a keystone for the arch. Without proper signals, chondrocytes in this zone fail to differentiate and thereby the resulting shape of Meckel's cartilage becomes flattened anteriorly (as observed in all Wnt mutants) and losing the convex shape anteriorly. In other words, the loss of the keystone results in the collapse of an arched structure. The next logical question might be what regulates the length of Meckel's cartilage resulting in such diverse sizes and length across species.

Lower jaw or bird's beak patterning have been studied in the past with many different secreted factors such as SHH, FGFs, WNTs and BMPs emanating from surrounding tissues to play a crucial role in mediating the shape and outgrowth of the ventral cartilage structures (Eames and Schneider, 2008, Merrill et al., 2008, Schneider and Helms, 2003).

Using a quail-duck chimeric system (quck), regional regulation of NCC have illuminated events involved in mediating the size of the lower jaw, in particular, the number of progenitors destined to form the jaw skeleton (Ealba et al., 2015, Eames and Schneider, 2008). The chimeric 'quck' embryos, which are duck hosts with quail donor cells, will form quail-like beaks and jaw joints and vice versa. The molecular mechanisms have been shown to involve the surrounding mesenchyme heavily influencing stage-specific and species-specific size and shape by exerting precise control over gene regulatory programs.

A recent study by Schneider's group has now shown that osteoclast bone resorption is another determinant thrown into the equation that regulates species-specific jaw length (Ealba et al., 2015). To maintain skeletal homeostasis, osteoclast work alongside osteoblast to regulate growth of skeletal structures. The study showed that when NCC destined to form the jaw skeleton transplanted from quail to a duck host (i.e. osteoclasts from donor NCC and osteocytes from host mesoderm), they observed an increase in tartrate-resistant acid phosphatase (*Trap*), *Matric metalloproteinase 13 (Mmp13)* and *Mmp9*. They further blocked bone resorption, which resulted in a significant lengthening of the jaw. On the contrary, activating resorption shortens the jaw. This interplay between NCC-derived osteocytes and mesoderm-derived osteoclasts adds another dimension to the regulation of the lower jaw by shedding light on the role of bone resorption in regulating size and shape of the jaw. What determines this species-specific NCC variation and what are the genetic regulatory networks involved remains an interesting question in this evolutionary biology.

From out study, further work looking closely at the regulation of Meckel's cartilage may add another component to size and shape determinants. Indeed, work done by over and underexpressing BMP showed variations in the size of the retroarticular cartilage (Parsons and Albertson, 2009). Given the different response of the midzone and body of Meckel's cartilage, we hypothesize that WNTs may play a crucial role in the anterior extension of Meckel's cartilage. Indeed, work on Lake Malawi cichlids by expanding Wnt signalling (using a Wnt agonist LiCL and a Wnt antagonist IWR-1) resulted in variation in skull morphology (Parsons et al., 2014). Due to the importance of WNT in craniofacial development (Liu et al., 2010), here I find that Wnt have precise control of not only specific regions of Meckel's cartilage that may have an importance in jaw size and shape but also in bone development.

3.3.3. Non-canonical Wnt is required for proper spatiotemporal control of endochondral bone formation

Perturbations in Wnt signalling have been studied extensively. The role of the canonical Wnts in bone biology has been better defined in the literature (Clevers and Nusse, 2012, Logan and Nusse, 2004, Zhong et al., 2012, Hartmann, 2006, Krishnan et al., 2006). Compared with mammals, endochondral bone formation (e.g. mentomeckelian or ceratohyal) occurs first by transdifferentiation of perichondral cells into osteoblasts that then forms a shell of bony mineralization (Eames et al., 2012, Hammond and Schulte-Merker, 2009, Jing et al., 2015, Paul et al., 2016). Here, we extended previous work in zebrafish by highlighting the role of the non-canonical Wnt signalling in temporal regulation of the endochondral ossification process.

Cartilage maturation and hypertrophy is the principal engine of endochondral bone formation. It requires chondrocytes to mature, proliferate and then produce collagen type 10 (Noonan et al., 1998). Here, we showed that chondrocyte proliferation that occurs at around 6 dpf is severely affected in *wls* compared to the other mutants studied, concordant with mice studies (Maruyama et al., 2013). We then observed a failure in differentiation in *wls* mutant, marked by the loss of *col10a1a* expression in the clear majority of craniofacial bones and cartilage. This is confirmed by the loss of *osterix* expression. Interestingly, we observed a high expression of *sox9a* and *runx2a* in *wls* mutant suggesting that cells remain in a pre-cartilage and pre-osteoblast stage but do not exit the cell cycle to undergo cell division. Together, this indicated that chondrocyte failed to proliferate and osteoblast failed to differentiate leading to a severe loss of bone formation. This points towards the essential role of *wls* regulating Wnt activity which is independent of *wnt9a* and *wnt5b* to direct chondrocyte proliferation, maturation and differentiation as well as osteogenesis.

While we did not observe any significant difference in proliferation in *wnt9a*, *wnt5b* or *gpc4* mutants, we did observe a loss of *col10a1a and osx* expression in the ceratohyal. This suggests that timely maturation and differentiation of chondrocyte is more prominent in the non-canonical Wnts. Previously published work on *gpc4* have noted that a small proportion of *gpc4* mutants survive to adulthood with robust formation of endochondral and dermal bones (LeClair et al., 2009). However, they noted the failure to form the symplectic bone and that other zebrafish mutants also affecting the biosynthesis of heparin sulfate proteoglycans, *dackel* (*dak*) and *pinscher* (*pic*) failed to form bones (Clement et al.,

2008). Since we did not observe the formation of the ceratohyal, mentomeckelian or retroarticular in *gpc4* mutants at 8 dpf, a delay in chondrocyte maturation may be a contributory factor to the delay in endochondral ossification. The loss of endochondral bones in our *wnt5b* mutant is like *Wnt5a* and *Wnt5b* knockout mice where both have been shown to inhibit hypertrophic maturation by down regulating *Runx2* (Bradley and Drissi, 2010, Bradley and Drissi, 2011).

Along with the results of our study, we showed that *wls, wnt9a, wnt5b* and *gpc4* are all required for: 1) proper chondrocyte organization to shape the cartilage anlage and 2) timely chondrocyte maturation to initiate endochondral ossification. In contrast to the endochondral ossification process, *wls* additionally plays a key role in intramembranous ossification where osteoblasts directly differentiate from NCC-derived progenitors and do not require a pre-cartilage anlage (Table 17). Since intramembranous bones are not affected in *wnt9a*, *wnt5b*, and *gpc4* mutants, it is likely that another ligand, perhaps *wnt14* acting through the β-catenin canonical Wnt pathway that requires *wls* for its secretion is essential for the commitment of NCC precursor cells to osteoblastic lineage. Therefore, the non-canonical Wnts acting through *wls* results in the loss of cell polarity and a delay in chondrocyte maturation, as seen in *wnt5b* and *wnt9a* mutants and confirmed with *gpc4* mutants. On the other hand, it is possible that the canonical Wnts acting through *wls* may account for the chondrocyte proliferative defect and severe loss of both endochondral and intramembranous bone.

In summary, we report the combined roles of *wls, wnt9a, wnt5b* and *gpc4* during zebrafish craniofacial cartilage and bone development by highlighting the interaction of these genes in juxtaposed cell types to regulate jaw morphogenesis.

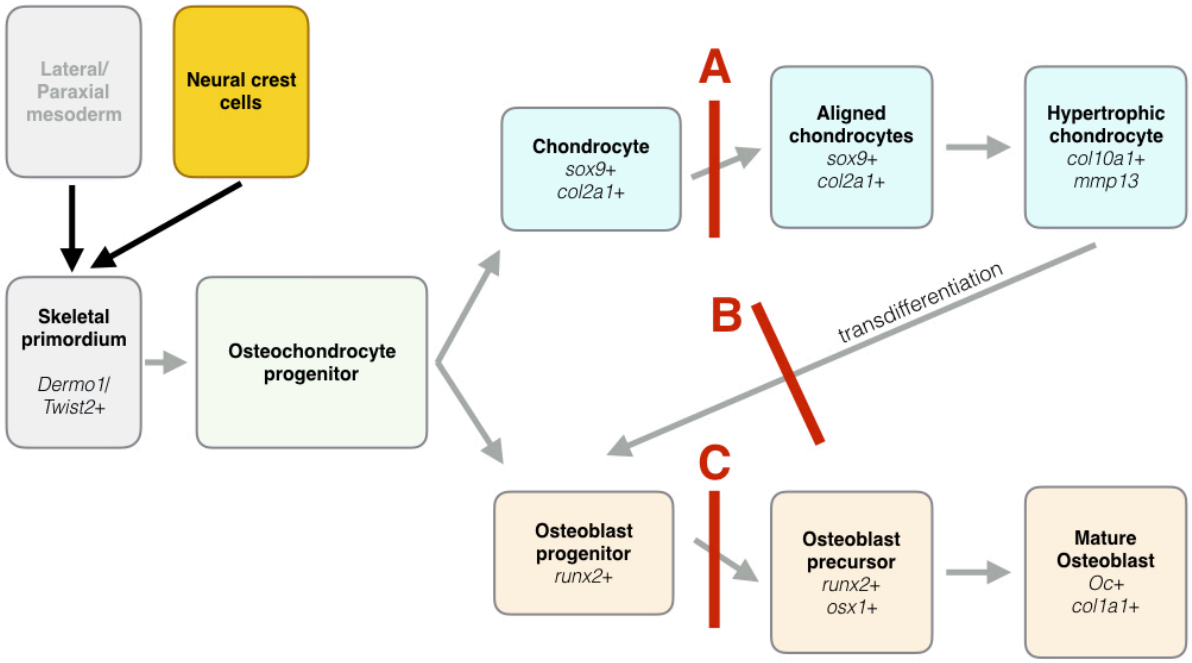

Figure 31. Summary diagram indicating role of Wnt signaling in endochondral and intramembranous ossification process

Skeletal primordium can be formed from both the lateral/paraxial mesoderm and neural crest cells. Focusing on neural crest derived bones, they will then form osteochondrocyte progenitor population is bipotential into a chondrogenic (blue) or osteogenic (light orange) fate. Once fated to become chondrocytes, they are required to align prior to maturing and hypertrophying. In the classical endochondral ossification model, these hypertrophic chondrocytes apoptose to leave behind a matrix for osteoblast protenitors to invade and deposit bone. In a newer concept, these hypertrophic chondrocytes can transdifferentiate into osteoblast progenitors. In our study, *wls* (and therefore Wnt signalling) is a key gatekeeper at points A and C for both chondrocyte and osteoblast progenitors to mature. *gpc4*, *wnt9a* and *wnt5b* (non-canonical Wnt) appears to act at point A and B (i.e. a more promiment role in the endochondral process as well as the transdifferentiation of hypetrophic chondrocyte into osteoblast progenitors).

3.4. Conclusion

We highlighted the combined roles of *wls, wnt9a, wnt5b* and *gpc4* during craniofacial cartilage and bone development. Moreover, we demonstrated the interdependence of various surrounding tissues to appropriately shape and form the facial architecture. Generating mutants harbouring double knockouts of different genes will promise insight into the different Wnt requirements, redundancies, rescues and interactions to properly shape and size cartilage structures. In addition, further investigation focusing on the role of both the canonical and non-canonical Wnt signals in the gene regulatory networks that differentiates the midzone and body of Meckel's cartilage will promise new insights into the diverse jaw lengths and sizes across species as well as insights into mandibular malformations and diseases. Understanding chromatin remodelling in NCC will provide a comprehensive understanding of how genes are being regulated during craniofacial development. A wider question might address the issue of environmental interactions in influencing not only the phenotype but also the genetic changes. Future directions for this project will help answer the question: What are the broader roles for Wnt in shaping the jaw? How does modulating this signal affect the regulatory networks and how does the spatiotemporal regulation influence jaw length? Additionally, further work is required understanding the transdifferentiation process will provide insight into the role of various crosstalks and signals during endochondral ossification. To help address these questions, we are developing the use of the confetti zebrafish transgenic line, termed Zebrabow (like the Brainbow mice) which will be discussed in the next chapter.

Chapter 4: Visualization of chondrocyte dynamic cell behaviour

Published in Journal of Visualized Experiments, 2015 Oct 21; (104): 52935, PMID: 26555721

Work presented here overlaps with the work published but offers more detailed insight into some of the experiments, additional data, further hypothesis and data analysis.

4.1. Introduction

CNCCs migrate and populate the first pharyngeal arch, then form paired mandibular processes that extend to form the Meckel's cartilage, which prefigures the mandible. Morphogenesis of the Meckel's cartilage requires chondrocyte arrangements via directional proliferation, cell polarization and differentiation (Dougherty et al., 2013, Le Pabic et al., 2014). However, the intricacy of chondrocyte organization in the growth and extension of the Meckel's cartilage remains unclear. Understanding dynamic cell behaviour is critical to understanding congenital malformations affecting mandibular size, such as hypoplastic mandible phenotypes (Ricks et al., 2002). Zebrafish embryos offer many developmental and genetic advantages for detailed study of Meckel's cartilage morphogenesis. Their genetic tractability, transparency, *ex vivo* and rapid development are powerful advantages lending it well for observation of cell movement and organization by live imaging (McCollum et al., 2011). Using lineage-tracing tools, such as *sox10:*kaede transgenic line, others and we have delineated the neural crest origins of the embryonic craniofacial skeleton (Gfrerer et al., 2013, Dougherty et al., 2013). Using the *sox10:*ERT2-Cre with the *ubi:*Zebrabow transgenic line, it is now possible to explore details of cellular movements during craniofacial development. The Zebrabow-M, is a transgenic line engineered with the ubiquitin promoter driving the expression of different fluorophores, each flanked by Lox sites (Pan et al., 2013). The Zebrabow default fluorophore is Red, expressing RFP. After induction of Cre expression, the Zebrabow construct recombines and cells express a combination of different fluorophores (RFP, CFP and YFP) creating multi-spectral expression in the embryo. All the daughter cells that divide from the labelled cells after the recombination event are then clonally labelled, so that cell populations that derive from different juxtaposed progenitors are clonally labelled. By this cloning cell labelling, cells proliferation and migration with clonal resolution can be followed.

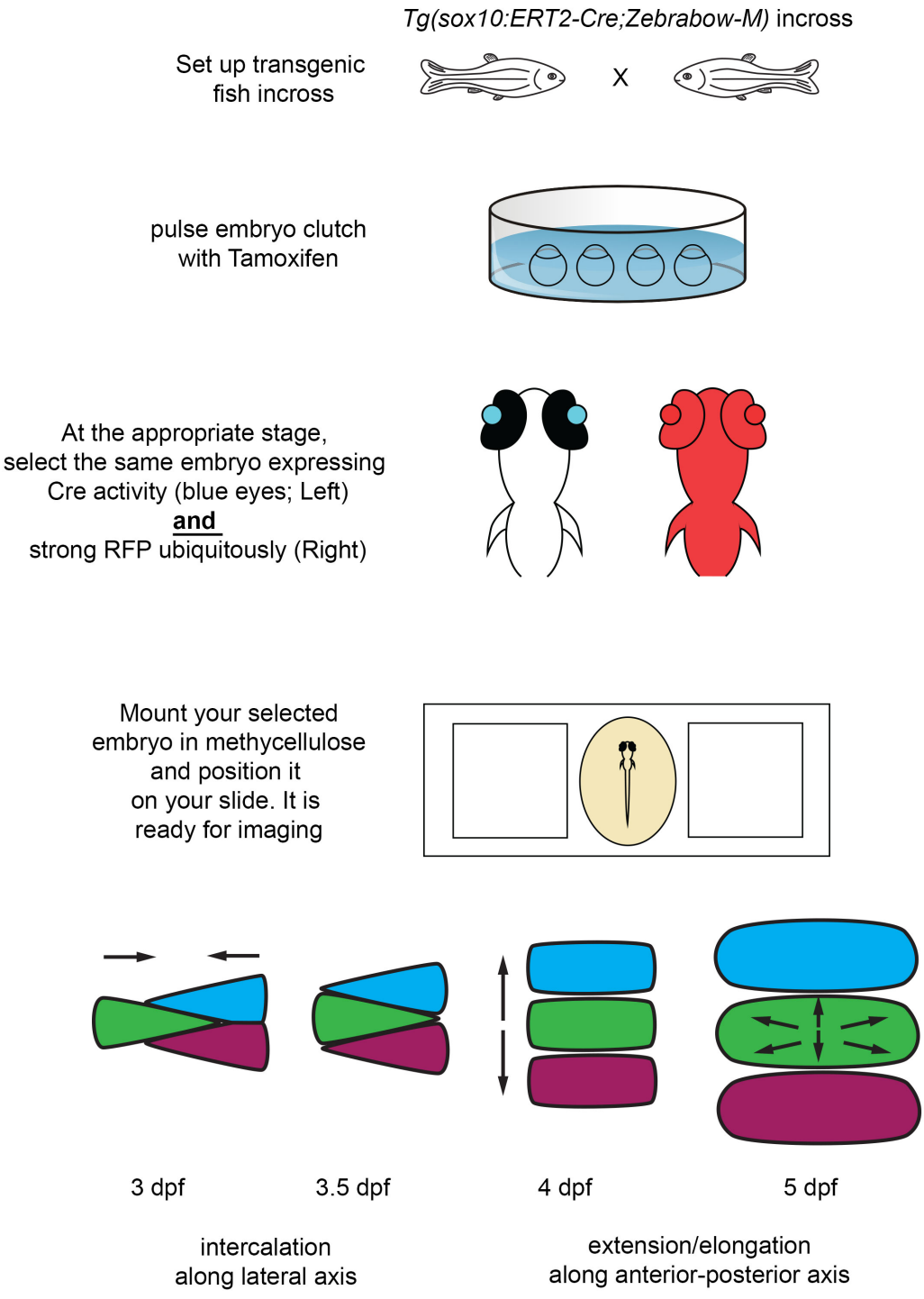

Figure 32. Methodology for inducing multispectral colour in Zebrabow transgenic line.

A double transgenic line with sox10:CreERT2 and Zebrabow are set up, embryos collected and induced with tamoxifen. Embryos are then mounted with methylcellulose and imaged with the confocal.

4.2 Results

Traditional cartilage visualization by whole mount Alcian blue stains has been invaluable in observing the developing Meckel's cartilage (Javidan and Schilling, 2004). To further analyse the developing chondrocytes over time, lineage tracing using *sox10:*Kaede transgenic lines has enabled us to study cell migration, convergence and extension (Dougherty et al., 2013, Javidan and Schilling, 2004). However, the organization of chondrocytes in the craniofacial skeletal structure remains poorly understood. The Zebrabow-M transgenic line can reveal, in live imaging, the chondrocytic intercalation and elongation process that mediates extension and growth of the Meckel's cartilage (**Figure 33**).

4.2.1. Generation of Tg(ubi:zebrabow;sox10:creERT2) transgenic line

The Tg(*ubi*:zebrabow-M) line was a generous gift from Alex Schier's laboratory, Harvard University (Pan et al., 2013). The Tg(*sox10*:creERT2) was generated in the laboratory. The targeting vector pDESTTol2-*sox10*:creERT2 was constructed using standard molecular cloning methods and Gateway technology (Invitrogen, CA). A p5' containing a 7.2kb clone of the *sox10* promoter along with a gateway middle clone pME-creERT2 and a p3' containing a polyA tail were combined in a LR reaction with a lens destination vector pDestTol2-α-*crystallin*:YFP. The final pDest-Tol2-*sox10*:creERT2 construct was then co-injected with Tol2 transposase mRNA into WT 1-cell stage Tubingen embryos. F0 adult founders were screened for germ-line transmission based on the YFP lens marker.

Stable Tg(*sox10*:creERT2) line was then crossed to the Tg(ubi:zebrabow-M) line to generate a double transgene fish identified by a ubiquitous RFP signal and a YFP lens marker (**Figure 32**).

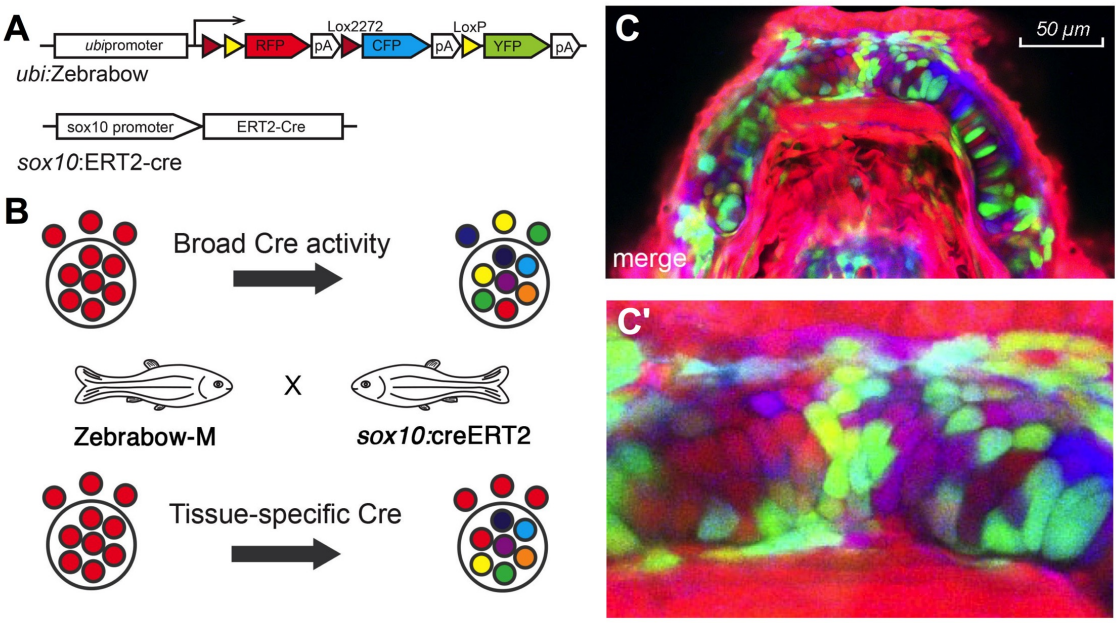

Figure 33. Zebrabow construct and recombination

(A) Diagrammatic scheme of the Zebrabow construct driven by a ubiquitous promoter (above) and the sox10 promoter driving the ERT2 inducible Cre (below).

(B) With broad Cre activity (using an *ubi*:Cre or Cre mRNA injection into Zebrabow for example), will result in recombination in every cell. Using a *sox10* promoter driving an ERT2 inducible Cre, only *sox10* derivatives will be labelled.

(C) Meckel's cartilage at 72hpf showing all *sox10* derivatives labelled with the surrounding non-neural crest cells expressing the default RFP colour

(C') Zoomed in of the midzone of Meckel's cartilage showing at least 10 colours following tamoxifen induction.

4.2.2. Cell recombination

*ubi:*Zebrabow-M*;sox10:*ERT2-Cre embryos were treated with tamoxifen at 10 somites and CNCC migration followed over time. Chondrocytes in the lower jaw were visualized at different time points of craniofacial structures development (from 3dpf to 5dpf). The lower jaw is best pictured ventrally to allow clear views of the Meckel's cartilage without the interference of the ethmoid plate and neurocranium dorsally. The stably maintained and inherited colours allow easy lineage tracing and CNCC cells fate mapping as indicated by the black arrows in (**Figure 36**). The single blue cell appears to migrate and intercalate with its neighbouring cells. It then elongates along the anterior-posterior axis to form a uniformly shaped chondrocyte thus maintaining the global shape of the Meckel's cartilage as it extends anteriorly. This technique allows the study of lower jaw growth malformations at the cellular and organ level in conditions such as Robin sequence where

micrognathia is one of the prominent features described. Failure in proliferation, extension or intercalation can be effectively visualized in the growing chondrocytes over time.

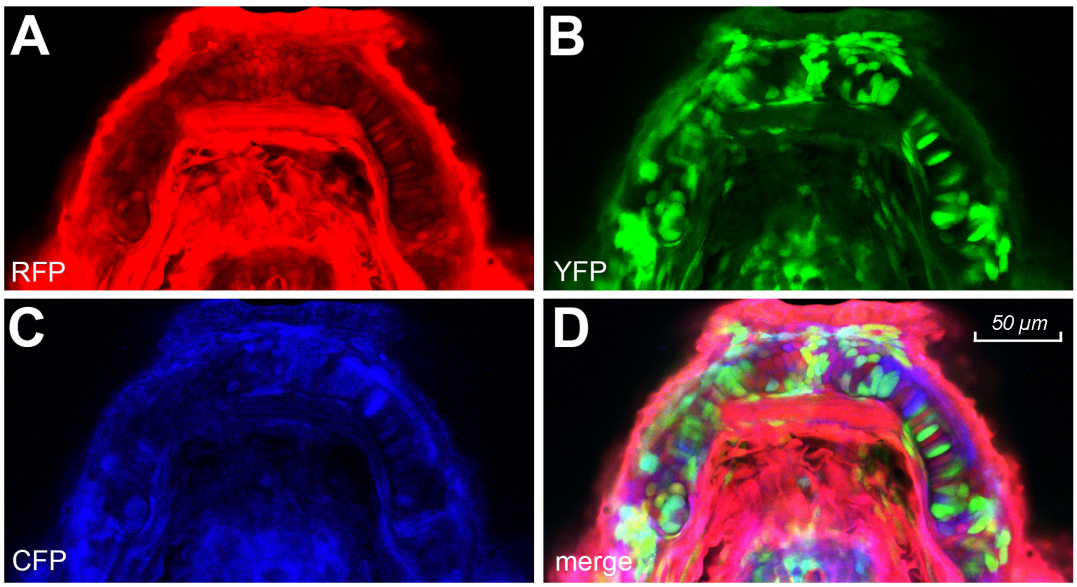

Figure 34. Zebrabow recombination with sox10:creERT2.
(A-D) Split channels of a representative image of Meckel's cartilage at 72hpf. Channels were imaged separately and excitation optimized to minimize bleed through, especially between the YFP and RFP channels. Colour diversity can be observed (D) after image processing of the individual channels in either Image J or Photoshop.

4.2.3. Zebrabow as a technique to analyse clonal population

Addition of tamoxifen to the double transgenic fish (Tg(*ubi*:zebrabow) and Tg(*sox10*:creERT2) during embryogenesis generates recombination in all cells derived from neural crest cells, as the *sox10* promoter is NCC specific. Since craniofacial cartilage and bone structures are all NCC derived, the generation of the Zebrabow fish allows assessment of clonal relationship between chondrocytes. At 55hpf, osteochondrogenic progenitors from NCC are seen to be labelled and undergone recombination (**Figure 35**). Other tissue structures such as the intermandibularis anterior/posterior (paraxial mesoderm derivative) or the epidermis are not labelled (remained default RFP). Subsequent imaging at different time points (72, 96, 120hpf) will allow tracking of a single cell (black arrow head) to examine localized clonal analysis (**Figure 35**B, C, D). In this case, there does not appear to be any expansion of chondrocytes between these time points, supporting the argument that proliferation of cells within ventral cartilage structures occur at a later stage (>6dpf).

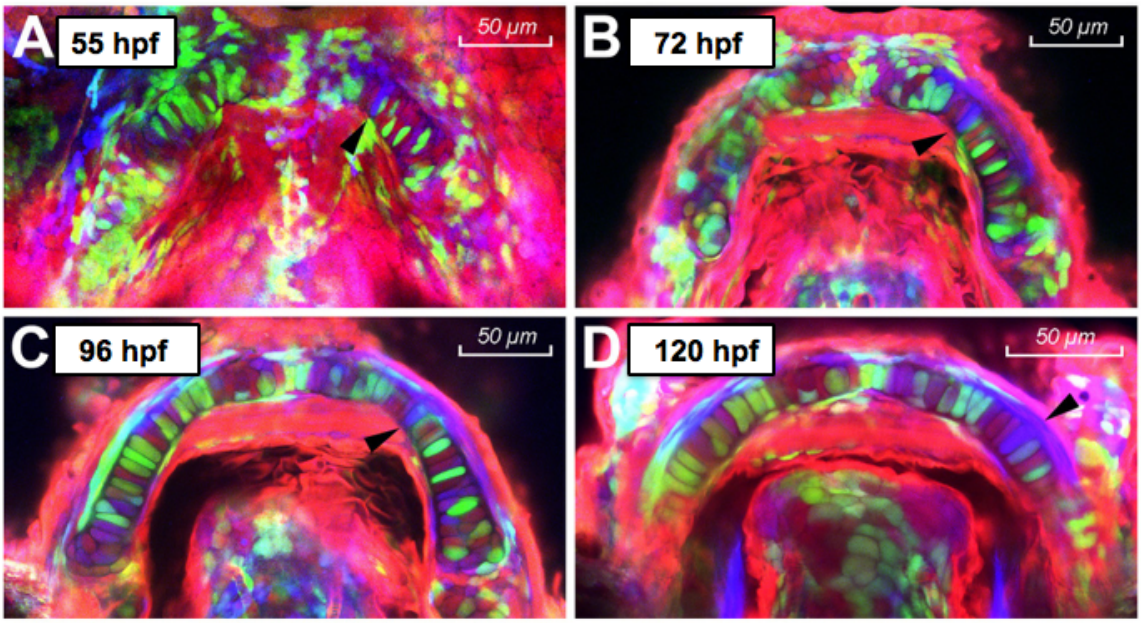

Figure 35. Clonal analysis using Zebrabow.

(A-D) Following Cre induction with tamoxifen at the 10 somites stage, Meckel's cartilage of a single embryo was imaged at different time points, 55 (A), 72 (B), 96 (C) and 120 (D) hpf. Following a single blue cell (black arrow), one may be able to observe any expansion of a certain cell clone over time. In this case, no cell division or clonal expansion was observed.

4.2.4. Zebrabow as a technique to visualize dynamic cell behaviour

In addition to the ability to trace the clonal population of a single cell using the cell's hue, an added advantage of the stochastic nature of the recombination allows us to study the dynamic behaviour of each cell over time. Analysing a group of cells (**Figure 36**A-C; dotted circle), we observed that at 55hpf, the group of cells appear as a 2-3-cell layer thick within Meckel's cartilage. By 72hpf, cells have appeared to intercalate and stack on top of each other. By 96hpf, cells are then seen to grow in dimension to further extend the cartilage structure. This intercalation process is key in defining an organ shape and this technique has given us unprecedented ability to study cell behaviour.

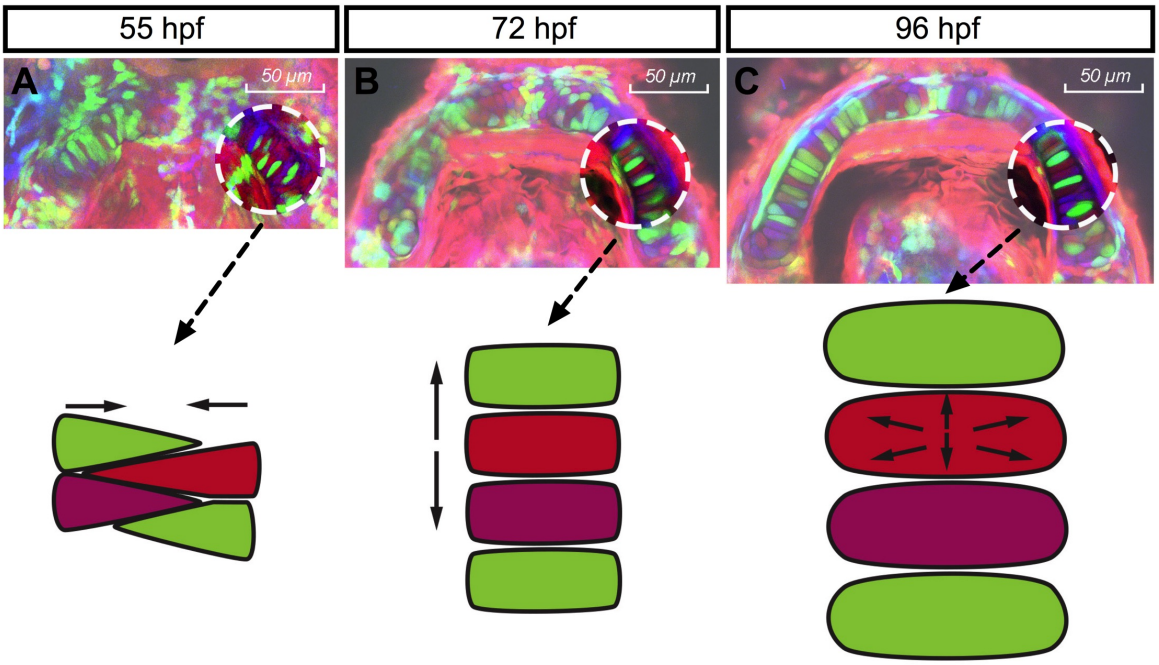

Figure 36. Dynamic cell behaviour using Zebrabow illustrates cell intercalation within Meckel's cartilage.

(A) At 55hpf, cells within the body of Meckel's cartilage appear to be in a 3-4 cell layer thick. By 72hpf (B), cells have intercalated and stack on top of one another like discs to extend the cartilage rod. At 96hpf (C), cells hypertrophy to enlarge the structure and subsequently undergo proliferation to further extend the ventral cartilage structures.

4.3. Discussion

Alcian blue staining has been commonly used to visualize final cellular organization of cartilage. In addition, photoconvertible transgenic lines in zebrafish such as *sox10*:Kaede allows for direct observation of cellular migration and proliferation in live zebrafish embryos (Dougherty et al., 2012). Each technique complements each other to define the intricate process of cartilage and bone development. However, live cellular migration and organization during organogenesis has long been hypothesized and indirectly demonstrated but never visualized. Zebrabow transgenic line coupled with a cartilage specific Cre permits simultaneous live observation of all these distinct events involved in bone and cartilage formation.

4.3.1. Colour diversity optimization

Optimizing Cre levels by titrating the concentration of 4-hydroxytamoxifen can control the extent of recombination and colour diversity without resulting in embryo lethality. Oestrogen is critical for normal retinal development and therefore, higher doses of tamoxifen (>25μM) can induce retina degeneration, high mortality rates (~60 to 80%), craniofacial malformations and developmental delays. In addition, 4-hydroxytamoxifen is diluted in ethanol, which is toxic during embryonic development (McCarthy et al., 2013). Therefore, it is important to determine the best concentration and duration of exposition to obtain a good recombination rate but limit the toxicity for embryos.

The desired concentration of 4-hydroxytamoxifen has been optimized in this protocol. Different concentrations (5-25μM), induction time points (10 somites, 24, 36 & 48hpf) and duration (30 min to 6hours) were tested. A low dose of tamoxifen (5 μM) produced a limited recombination while higher dose (from 10μM to 20μM) produced similar recombination and colour diversity (**Figure 37**). Doses greater than 20μM compromised normal development of embryos and therefore not suitable for studying craniofacial malformations. Induction durations less than 2 hours were not sufficient to create adequate recombination while over 6 hours of induction induced toxicity and developmental anomalies in the embryos. Induction for 3 or 4 hours did not differ in the amount of recombination and results.

Induction after the 24hpf embryonic stage did not produced desired recombination and fluorescent expression. Therefore, the best compromise between normal development and

suitable number of colours without resulting in significantly high numbers of embryonic mortality was determined to be 3 hours of induction at 10 somites with a 10μM concentration of tamoxifen. Induction in adult Zebrabow lines is not covered in this study but tamoxifen dissolved in system water may be insufficient to cause any recombination. Therefore, for later stage zebrafish, tamoxifen injections may be a more effective method to induce any Cre activity.

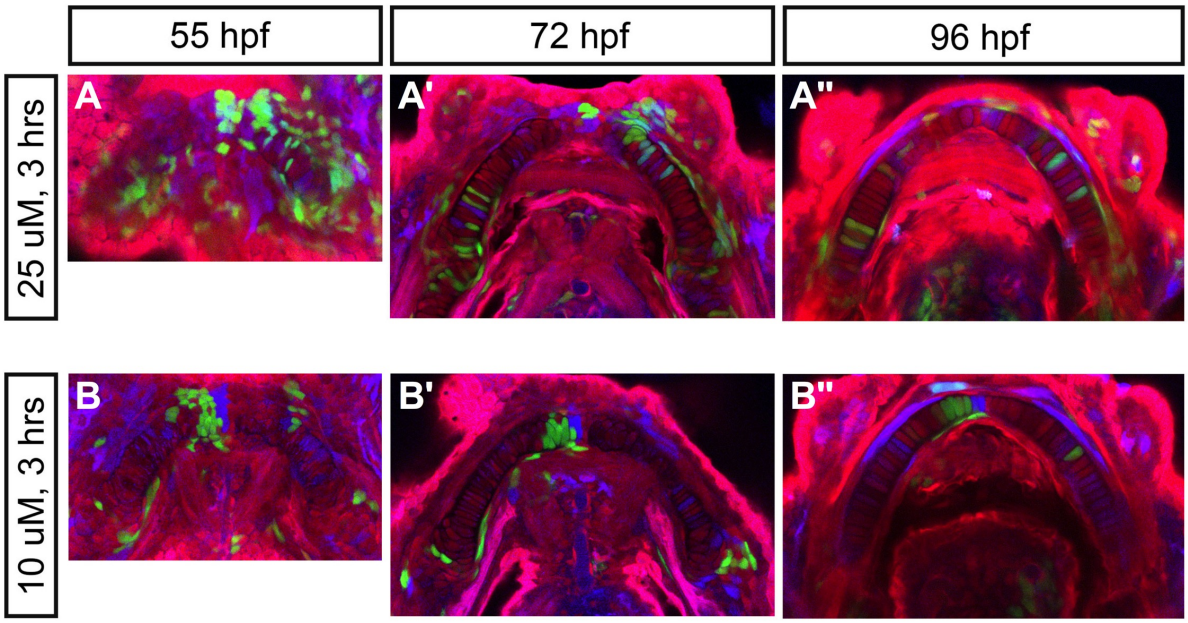

Figure 37. Different concentration of tamoxifen results in different colour diversity and labelling. (A-A'') Using 25 uM with a 3 hours pulse results in more recombination compared to a 10 uM pulse where only a small subset of cells were effectively labelled.

4.3.2. Image quality

Obtaining consistent and high quality images can be challenging. If a single field of view is unable to visualize the whole Meckel's cartilage or craniofacial structure of interest, the whole structure can be mapped by taking montage images or Z-stacks. However, obtaining Z-stacks can be challenging in live embryo imaging due to movement artefacts. Therefore, it is important to have a compromise between the quality of the Z-stack image, the amount of information required during the imaging session and prevention of laser-induced photo-bleaching during longer term laser exposure.

Fluorescent proteins do not show the same stability during imaging. For example, RFP is a stable protein but YFP can be fragile. The colour diversity in zebrabow system is a key point for lineage tracing. Therefore, during the imaging process it is important to determine

empirically the best imaging settings to detect the maximum number of colours in each embryo with suitable intensity. A limitation in confocal imaging used in this protocol is that most confocal microscopes are unable to read CFP and YFP together. This is because the emission from CFP is detected in both 470nm and 535nm channel. Also, this emission spectrum of CFP (470-535nm) and the excitation spectrum of YFP (530nm) overlap, creating fluorescence resonance energy transfer (FRET) artefact. In other words, when the CFP fluorescence is detected, it excites YFP fluorescence and therefore creates a non-specific signal. For this reason, all fluorescence channels were scanned separately in this protocol and merged separately using an imaging processing software (Image J or Photoshop). This may compromise some permutations of colour recombination. To overcome this, two-photons microscopy can be used as described in Pan et al's paper where all three fluorescence expressions can be read concomitantly allowing for more colour diversity (Pan et al., 2013). Other confocal microscope that allows for adjustable excitation ranges has also been shown to produce a spectrum of colour diversity with minimal bleed through (tested on a Leica TCS SP8 STED 3X, Zeiss LSM 800 and Olympus FV3000 confocal). In addition, Pan et al has described a large spectrum of colour diversity in their Zebrabow lines (up to 30 colours). With the conditions described in this protocol, different intensities of fluorescence were obtained, compatible with results obtained by Pan and colleagues

4.3.3. Colour inheritance and clonal analyses

Pan and colleagues have described the stably maintained colour inheritance in Zebrabow from progenitor to progeny that allows for fate mapping (Pan et al., 2013). This protocol focused on neural CNCC cells to characterize the formation of the Meckel's cartilage. The use of CreERT2 in zebrafish allows for efficient tamoxifen induced loxP cassette recombination and the ability to control the onset of CNCC lineage labelling during craniofacial development. This method can easily be adapted to visualize all neural crest derivatives besides the Meckel's cartilage. In addition, using a different transgenic reporter line for clonal analysis in various organ systems will highlight different modes of cell growth during organogenesis. The method also allows identification of other cell populations that has not been previously shown in other transgenic lines (**Figure 38**). **Figure 38** shows a panel of different transgenic lines used to visualize Meckel's cartilage ventrally. **Figure 38**A and C shows 2 different transgenic line; *sox10*:GFP showing chondrocytes and *sp7*:GFP showing osteoblast progenitors. The zebrabow:*sox10creERT2*

line shown in **Figure 38**B and induced at 10 somites revealed not only the chondrocyte population but also the osteoblast condensation (white circle). Interestingly, using a nerve specific line (*isl2*:GFP), we showed that the end of the mental nerve also coincided with this primary condensation point. Therefore, the zebrabow line is invaluable for further work looking at not only cell dynamics but also clonal analysis.

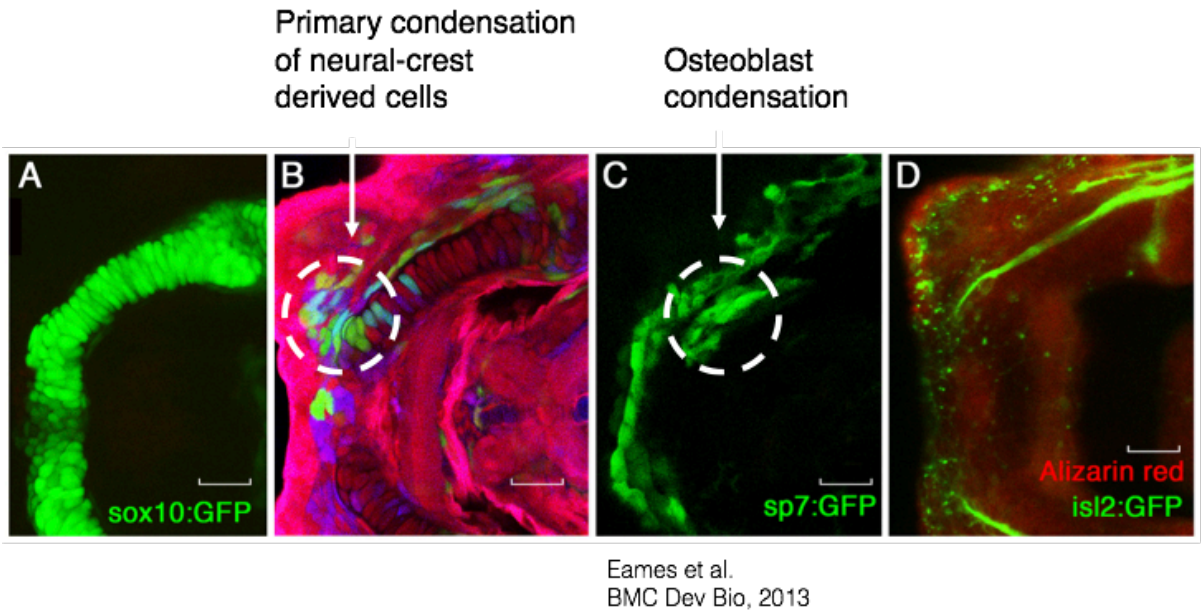

Figure 38. Zebrabow allows identification of other sox10 derived cells within ventral cartilage structure

A. Ventral view of Meckel's cartilage at 3dpf using a Tg(*sox10*:GFP) line. B. The Zebrabow line crossed to *sox10*:creERT2 and induced at 10 somites. Here we can see a clear condensation of clonal NCCs (within the dotted circle) that may be the site of osteoblast progenitor (C) as shown in the Tg(*sp7*:GFP) line.,Tthis point also coincides with the end of the mental nerve as shown in D using a Tg(*isl2*:GFP) line that highlights nerves.

4.3.4. Imaging deeper structures

Superficial structures such as ventral cartilage elements are easily imaged using a confocal/single photon microscope. However, for deeper cartilage structures such as the neurocranium in a whole-mount embryo, live imaging using a single-photon microscope can be challenging (>1 mm in depth) due to scattering of UV light by the tissues. This can be overcome by multiphoton imaging using the deep focus mode, allowing precise excitation of the fluorophores at the desired depth and minimizing scattering and over excitation of the fluorophores above and below the plane of focus (**Figure 39**). Here we imaged the ethmoid plate to determine if we can visualize the cellular intercalation

between the frontal nasal prominence and the two lateral maxillary prominence. In **Figure 39**A, we can just about make out cellular details of the chondrocytes when using the confocal but contrast this to the multi-photon microscope in **Figure 39**B where clear resolution of the chondrocytes and colour diversity can be appreciated. This provides an exciting tool to help study palate development and cellular dynamics within this complex process.

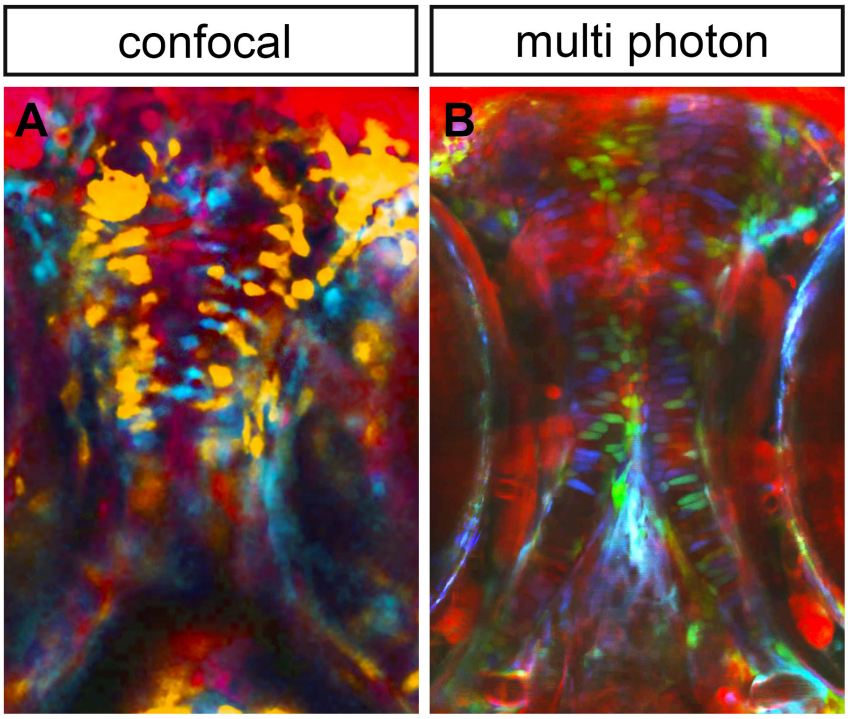

Figure 39. Zebrabow of the zebrafish ethmoid plate.

(A) Confocal image at 4 dpf showing rough outlines of chondrocytes compared with a two-photon image of the same structure (B). Cells have a clearer outline with more colour diversity. Note autofluorescence from the parasphenoid and the melanocytes within the eye.

4.4. Summary and future directions

The double transgenic Zebrabow and tissue specific *sox10* has shown to be a valuable tool in uncovering dynamic cell behaviour during craniofacial development. I am currently propagating this line into all the Wnt mutants to determine whether stacking defects are apparent in homozygote mutants. Additionally, this tool will be useful in studying cartilage regeneration. Recent studies have looked at the remarkable regenerative capability of zebrafish lower jaw (Paul et al., 2016). By utilizing Zebrabow, one would be able to trace where the regenerative cells originate, the periochondral cells, mesenchymal cells or chondrocytes within Meckel's cartilage. This will allow further transcriptomic studies to understand gene regulation during cartilage and bone regeneration. I am also using a UAS:Zebrabow line instead of the *ubi*:Zebrabow line. This will rid of the ubiquitous RFP background that hinders Z-stack confocal imaging. Preliminary study and imaging showed difficulty with the UAS promoter as the colour is sporadic and mosaic. This may be due to inefficient transgene expression within each chondrocyte likely due to the UAS promoter that tends to methylate with subsequent generation. Further characterization of the UAS:Zebrabow (terms cytabow) line is required for this to be useful in lineage tracing experiments.

Chapter 5: The role of coat protein complex mechanisms during craniofacial development

This next chapter is a parallel unpublished project we have been working on to complement not only our understanding of chondrogenesis but also Wnt trafficking during craniofacial development.

5.1. Introduction

Endocytosis and vesicle trafficking are vital processes that regulate many aspects of development and cellular homeostasis. It governs cell communication via secretion and uptake of signalling molecules, enzymes, proteins and lipids (Glick and Nakano, 2009). The secretory pathway sequentially involves the endoplasmic reticulum (ER), Golgi and the trans-Golgi network. Highly dynamic, this pathway responds acutely to specific cellular demands. It delivers newly synthesized proteins, lipids and carbohydrates manufactured from the ER to the cell surface with pre-secretory modification being made as these molecules move through the network (Glick and Nakano, 2009). Membrane traffic between the ER and the Golgi is bi-directional where forward (anterograde) and reverse (retrograde) transportation provides a fundamental gateway to the endomembrane system. Several families of coat proteins are conserved across species from yeast to mammalian systems. Three major coat proteins are: 1) clathrin/adaptor protein (AP-1 and AP-2), 2) coat protein complex I (COPI) and 3) coat protein complex II (COPII) (Schekman and Orci, 1996). These machinery are central to the transportation mechanism: coat protein complex II (COPII) operates in the anterograde (ER-Golgi) (Barlowe et al., 1994) while coat protein complex I (COPI) operates in the retrograde route (Golgi-ER) (Bednarek et al., 1995) (**Figure 40**).

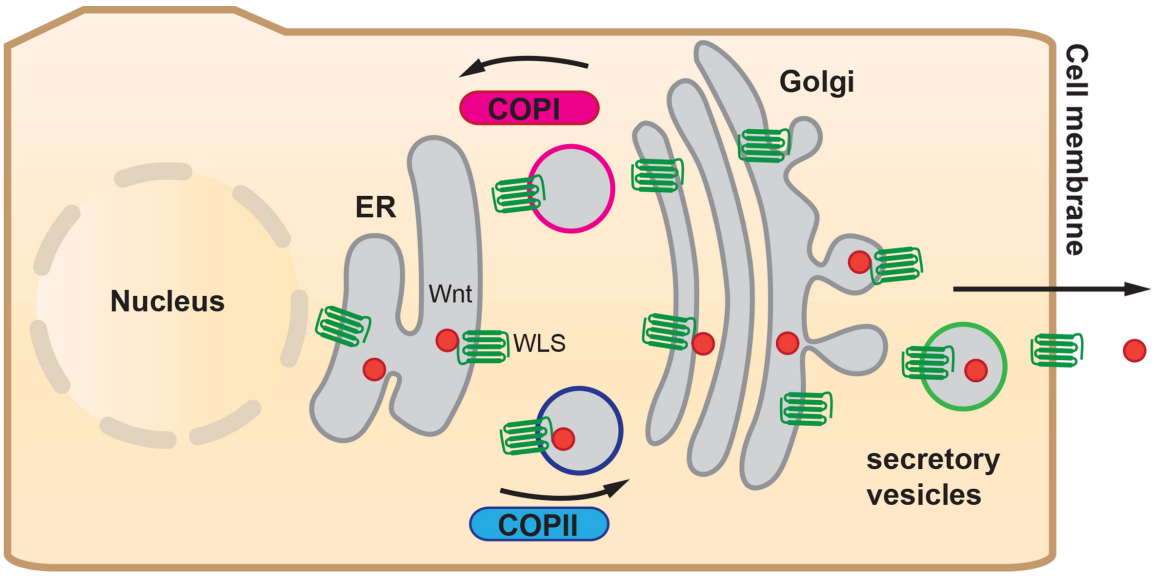

Figure 40. Secretory mechanism within a cell.

COPII (blue) represents anterograde transport from ER to the Golgi complex while COPI (pink) represents retrograde transport and recycling of WLS (green figure)

There are currently several models of secretion/trafficking within different cells; 1) vesicular transport, 2) cisternal maturation and 3) a combination of both pathways (Glick and Luini, 2011, Glick and Nakano, 2009, Luini, 2011). The vesicular transport model argues that cargo proteins are transported from late to early cisternae by COPI and COPII coated vesicles. The cisternal model is based on the concept that cargo is maintained within Golgi compartments and through a progressive series of Golgi cisternae maturation, move through Golgi stacks. This cisternae maturation work essentially as anterograde carriers for secretory protein transport. This model has been supported in the past through direct observation that large procollagen aggregates effectively move through the Golgi stacks without leaving the lumen (Bonfanti et al., 1998). More recently, a combination of both models has been proposed where large cargos progress through cisternae maturation while smaller cargos will move rapidly through vesicular transport (Martinez-Menarguez et al., 2001). However, how different cells regulate these processes and underlying molecular mechanisms remains to be answered.

COPII trafficking has been explored in the past to be highly important during craniofacial development by playing a fundamental role in chondrocyte maturation (Lang et al., 2006, Garbes et al., 2015, Fromme et al., 2007, Sarmah et al., 2010, Townley et al., 2008). More recently human mutations affecting COPI activity have also been found to result in craniofacial phenotype including micrognathia and microcephaly (Izumi et al., 2016).

COPI-coated vesicles are widely known for retrograde transportation of Golgi resident proteins. COPI coat consists of seven coatomer proteins and one small GTP-binding (G) protein, ARF (ADP-ribosylation factor). The seven COPs are termed α, β, β', ϒ, δ, ε, ζ with molecular masses ranging from 160 kDa (α) to 20 kDa (ζ) (Waters et al., 1991, Dodonova et al., 2015). COPI forms two layers the α, β' and ε subunits forming the B trimeric inner complex and β, ϒ, δ, ζ subunits forming the F tetrameric outer complex (Dodonova et al., 2015). The recent paper highlighting COPI functions in craniofacial development has added it to the complex network of mechanisms underlying the proper patterning and shaping of the head.

To further clarify the role of COPI proteins in this process, we decided to use a novel viral insertion mutant *copa*^{hi1872Tg} to study the role of COPI in craniofacial morphogenesis. We compared this mutant to existing ENU mutants and previous morpholino data and found similar phenotype involving defective notochord and melanogenesis. In addition, we sought out to develop a tissue specific loss-of-function of *copa* in zebrafish using CRISPR/Cas9 gene editing methodology to specifically dissect the role of COPI during NCC development. While further work is required to test these transgenic lines, we also aim to study retrograde transport of wls that has been previously found to be shuttled back from plasma membrane to the ER via COPI vesicles. Since wls is central to Wnt secretion, studies into this aspect will help understand how *wls* modulates Wnt activity during development and in return, understand what factors regulate wls.

5.2. Results

5.2.1. Molecular genetic nature of the copa^{hi1872Tg} mutation

The *copa* gene was identified in a craniofacial and pharyngeal arch expression analysis screen using the zfin online database as a reference. Dr. Sun Zhao at Yale University kindly provided us with the *copa^{hi1872Tg}* mutant zebrafish line. The *hi1872* fish was previously isolated in a retroviral insertion screen previously described and affects the *copa* gene (Amsterdam et al., 1999) (Figure 41). Larvae homozygous to the *hi1872* mutation produces an approximate Mendelian ratio of offsprings displaying similar phenotype; wavy notochord, dramatic loss of pigmentation and widespread degeneration by 72hpf (**Figure 41**).

A previous ENU-induced *sneezy^{m456}* mutation affecting the *copa* gene was also identified in a large-scale systematic screen affecting embryogenesis (Coutinho et al., 2004). The *m456* mutation resulted in a nucleotide substitution (G → T) in the splice donor of predicted exon 30 in the *copa* gene. This point mutation causes abnormal splicing and subsequently a frameshift mutation resulting in a premature truncation of the protein. Larvae homozygous for *sny^{m45}* are significantly shorter than WT siblings due to failure of notochord cells to differentiate and lengthen properly, fail to form pigmented melanophores in the trunk, and do not survive past 72hpf (Coutinho et al., 2004). The notochord is a rod-like embryonic structure arising from the dorsal organizer forming the chordamesoderm and is located in the midline ventral to the neural tube (Harland and Gerhart, 1997). It plays an essential role in permitting normal development by providing not only signalling cues to pattern surrounding tissues but also integral skeletal support for early locomotion (Adams et al., 1990, Cleaver and Krieg, 2001, Cleaver et al., 2000). As the notochord cells acquire large vacuoles, they exert turgor pressure against the thick perinotochordal basement membrane providing the notochord with rigidity, thus allowing proper elongation and development of surrounding tissues (Harland and Gerhart, 1997). Previous large-scale screens in zebrafish identified mutants lacking basement membrane genes such as Laminin β1 and Laminin γ1 results in failure of notochord cells differentiation (Parsons et al., 2002). Three other genes in the same study by Parsons and colleagues, affecting three subunits of the coatomer vesicular protein coat complex produces the same phenotype as the Laminin mutants resulting in dramatic reduction in pigmentation and degeneration by 2dpf (Parsons et al., 2002). The *sny^{m456}* mutant showed

failure to assemble the perinotochordal basement membrane caused by defective transport mechanism to form the axial mesoendoderm, leading to notochord cells remaining in an undifferentiated state and subsequently cell apoptosis due to disruption of the endoplasmic reticulum and Golgi networks (Coutinho et al., 2004).

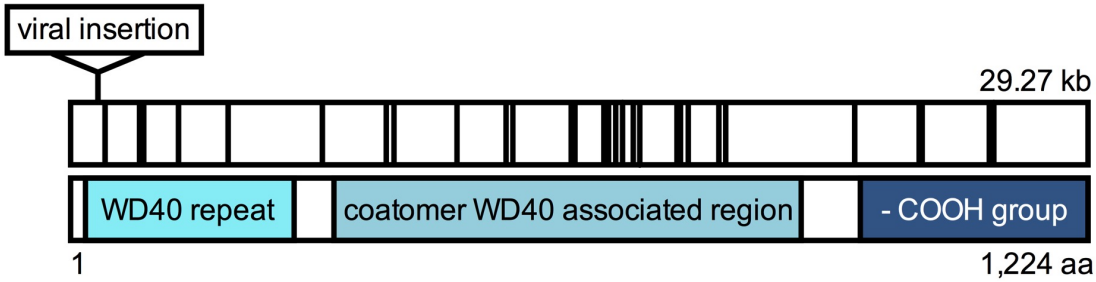

Figure 41. *copa* gene and protein domains.

Full-length *copa* gene stretches 29.27 kbs and contains 1,224 amino acids with a molecular weight of 138 kDa. Viral insertion for the *copa*^{hi1872Tg} mutant line occurs at the 5' UTR region.

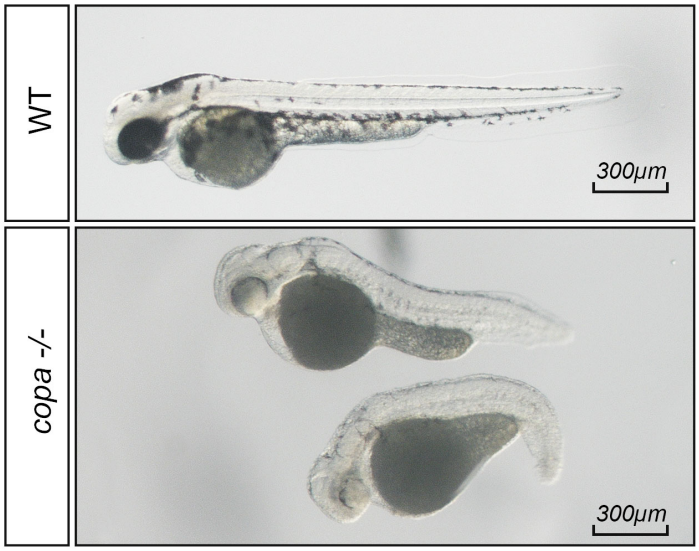

Figure 42. WT and *copa*^{hi1872Tg} mutant at 48hpf.

Bright field live imaging of WT embryo at 48hpf (top) and two separate *copa* homozygote at 48hpf.

To be sure of the genotype-phenotype correlation (**Figure 42**), we scored a clutch of heterozygote *hi1872* incrosses for their genotypes by PCR. The mutant and WT alleles were distinguished by the reverse primer 5'MSL4 which binds in the viral insertion and a second reverse primer, R2 (as shown in Table 18) which binds in intron-1. When these primers are paired with a common forward primer C1 which binds in the 5' UTR, the 5'C1/MSL4 primer pair amplified a band of 180bp with mutant genomic DNA but no band with WT DNA. The 5'C1/R2 paid gave a 350bp fragment with WT DNA and no band with

homozygote mutant DNA. Heterozygote genomic DNA will therefore produce 2 bands (**Figure 43**).

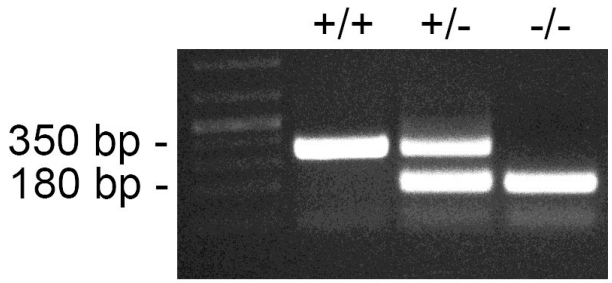

Figure 43. Genotyping of *copa*^{hi1872Tg}.

Three primer PCR used for genotyping. WT allele is at 350bp while mutant allele is 180bp. 2 bands indicate heterozygote embryos.

Table 18. Genotyping primers for *copa*^{hi1872Tg}

Primer	Sequence
1872C1 Forward	5' – gacgtggagcttgcgatgctg – 3'
R2 reverse	5' – ctgtgtggtgtatttcttgaggcc – 3'
MSL4 reverse (on retrovirus)	5' – gctagcttgccaaacctacag – 3'

5.2.2. copa^{hi1872Tg} mutation inhibits production of mature message and protein

An allele with a molecular lesion that deletes protein function would strengthen interpretation of the mutant phenotype observed. Given the position of the primers, we conclude that the viral insertion is not in the coding regions but within the 5' UTR region of the *copa* gene. The UTR regions are key in stability and the 5' UTR sequence is required for ribosomes to bind and initiate translation of the mRNA to protein. Therefore, to ensure that viral insertion within the 5' UTR in *hi1872* leads to a loss in mRNA, we prepared cDNA from mutant and WT embryos and performed real time quantitative-PCR.

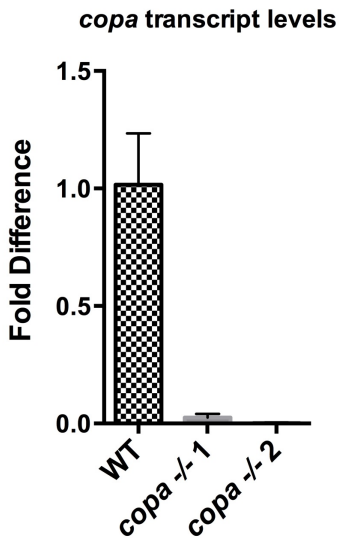

Figure 44. qPCR of *copa* transcript levels.

48hpf homozygotes were isolated and *copa* mRNA transcript levels were measured compared to a stage-matched controls (ET embryos). Two separate clutches were used. Significant downregulation of *copa* mRNA levels in both clutch.

To learn the extent to which copa message is reduced in the *hi1872Tg* homozygotes, we prepared cDNA from 48hpf mutant and WT animals. We then conducted qPCR using probes that amplifies 48bp of exon 1 and 126bp of exon 2. The ubiquitously expressed housekeeping gene, *eukaryotic initiation factor 1 alpha (eif1α)* provided an internal standard. Experiments were performed in triplicates as well as a negative control with no cDNA added to the qPCR mix. The results revealed that $copa^{hi1872Tg}$ mutants possess a drastically reduced *copa* transcript assessed in two different homozygote clutches (**Figure 44**).

To confirm whether protein function is destroyed, western blot analysis run on protein lysates of pooled homozygote $copa^{hi1872Tg}$ embryos revealed absence of protein at 138 kDa. β-actin was used as the control (housekeeping gene) (**Figure 45**). These sets of experiments allowed us to conclude that $copa^{hi1872Tg}$ disrupts *copa* gene production.

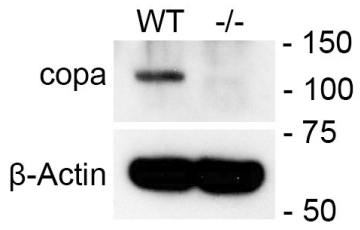

Figure 45. Western blot of *copa* protein levels.

48hpf copa homozygotes were isolated, protein extracted and subjected to SDS-PAGE analysis. WT copa protein molecular weight is predicted to be approximately 138 kDa. B-actin was used as a loading control.

5.2.3. Full-length copa mRNA rescues homozygote phenotype

Given that the genotype correlates with the phenotype and that we found that the *hi1872* mutant does not produce any *copa* mRNA and protein, we sought to determine the specificity of phenotypes observed in *copa* mutants. We injected 200pg of full length *copa* mRNA into 1 cell-stage embryos from an incross of *copa* heterozygotes. We then observe the phenotypes at 4dpf and stain for cartilage with Alcian blue. Appreciable rescue of the phenotype at 48hpf showed craniofacial structures formed, albeit defective formation of the ethmoid plate and ventral cartilage structures (**Figure 46**). Staining with Alcian blue indicates sufficient extracellular matrix is being secreted by the chondrocytes. Despite an appreciable ethmoid plate structure, defects can be observed by incomplete fusion of the frontal nasal prominence with the bilateral maxillary prominence anteriorly. Additionally, ventral cartilage structures are notably smaller and shorter compared to its WT sibling (**Figure 46**). This may be due to the depletion of the injected mRNA thereby suggesting a later essential and functional role of *copa* in proper embryonic development. Within the same clutch, overexpression of the *copa* mRNA was also observed which interestingly, displayed a similar phenotype as the *copa* homozygote mutants; loss of pigmentation and wavy notochord (**Figure 46**). Embryos survive to 96hpf, allowing analysis of the craniofacial structures. This showed severely defective craniofacial cartilage structures, rounded chondrocytes, smaller ethmoid plate, a malformed Meckel's cartilage and weak staining of the ceratobranchials. The chondrocytes within Meckel's cartilage appears in clumps and have a reduced width and length ratio. The weak staining of Alcian blue may indicate failure of sufficient ECM being excreted by the chondrocytes due to defective transport mechanism. Following Alcian blue analysis, embryos were genotyped to confirm the phenotype observed. Different concentrations of *copa* full length mRNA were injected into separate clutches of *copa* incrosses (50pg, 100pg, 200pg, 300pg, 500pg).

Concentrations lower than 200pg did not rescue the phenotype and concentrations greater than 200pg resulted in high percentage of death and toxicity (as seen by brain malformation with a dusky appearance). This further shows that a fine balance of *copa* function is required to maintain proper cellular function during chondrogenesis.

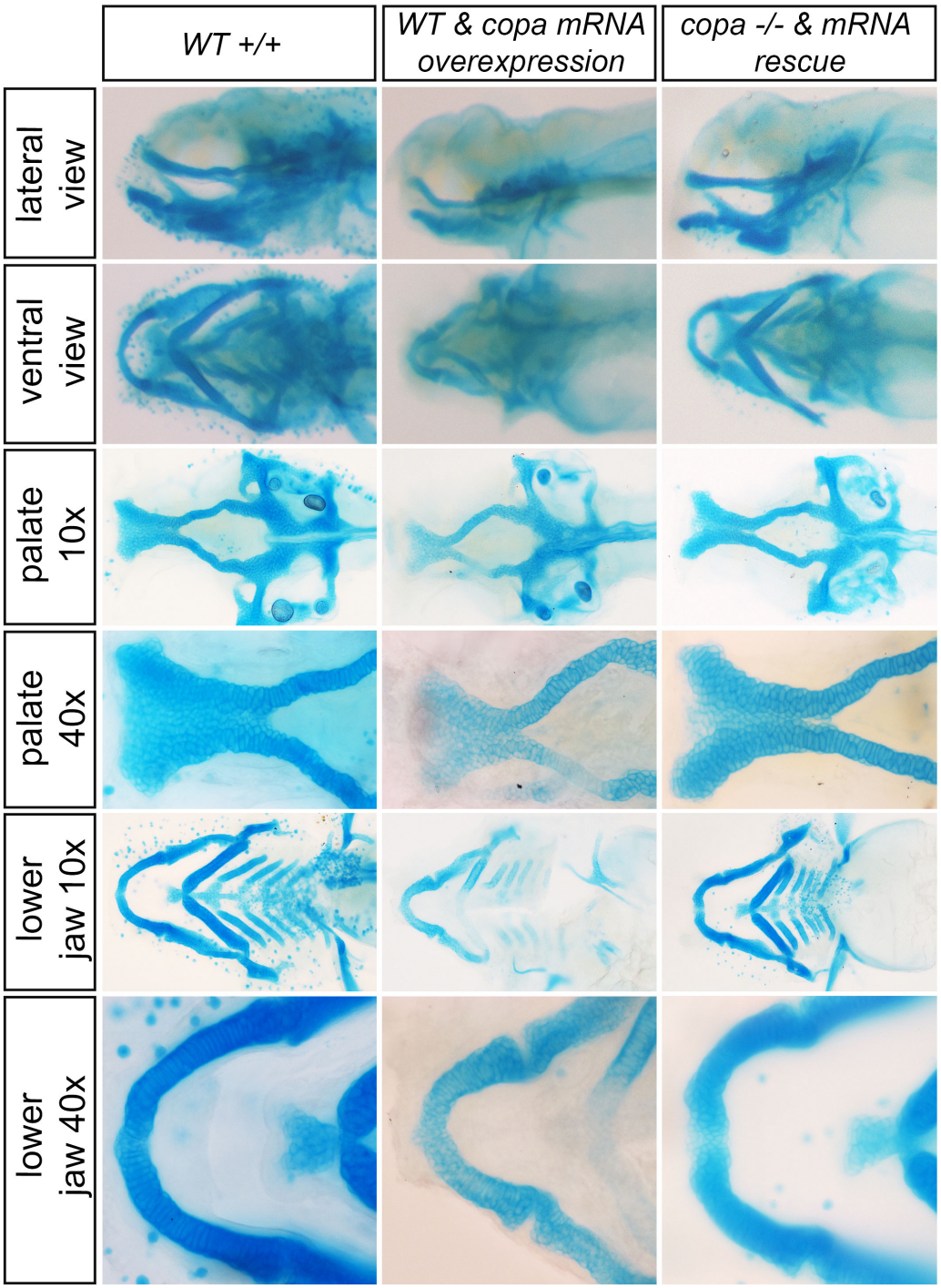

Figure 46. *copa* mRNA injection overexpression and mRNA rescue.

Injection of 200pg of *copa* full length mRNA rescues the 48hpf lethal phenotype allowing craniofacial analysis at 4dpf. Injection of 200pg *copa* full length mRNA in *copa* homozygotes at the 1 cell stage shows defect in craniofacial structures at 96hpf with a clefting defect of the ethmoid plate as well as a reduced size of the Meckel's cartilage compared to WT. A similar concentration of 200pg of *copa* full length mRNA into WT Tübingen embryos showed severe craniofacial defects with smaller, rounded chondrocytes and a misshapen Meckel's cartilage.

5.2.4. Zygotic copa activity

Whole mount RNA *in situ* hybridization was carried out to delineate the spatiotemporal requirements of *copa* during early embryogenesis. A full length *copa* probe was then used to examine the expression of *copa* in staged WT embryos; at 10 somites (onset of NCC migration), 24hpf (organogenesis), 48hpf (craniofacial morphogenesis), 72hpf (ethmoid plate fused and formed) and 96hpf (Meckel's cartilage shaped and aligned) (**Figure 47**). Previous studies have observed *copa* expression at the 32-cell stage that continues through to shield stage. This demonstrates the presence of maternal transcript early in gastrulation.

At 10 somites, strong expression is observed at the polster (forms future forebrain), throughout the notochord and mild expression within the NCCs bilaterally (**Figure 47**A-C). By 24hpf, the brain, pharyngeal arches, notochord, endoderm and blood vessels around the yolk also show strong expression of *copa* (**Figure 47**D, E). By 48hpf, expression localizes the pharyngeal arches, cranial sutures, liver bud, pectoral fin, gut, renal tract and swim bladder lining (**Figure 47**F, G). No expression observed at the notochord, somites or brain tissue. A similar pattern of expression persists at 72and 96hpf but without expression of the pectoral fins (**Figure 47**H-M). At 96hpf, embryos showed expression in the head and flat-mount of the dissected embryo head showed clearer outlines of all ventral cartilage structures. To determine if the expression is within the chondrocytes of surrounding mesenchyme, we performed sagittal sections. These sections revealed that expression underlines all craniofacial cartilage structures (**Figure 47**N-P). Further sagittal sections through the midline of the body showed strong expression within the epithelium of the swim bladder and entire length of the gut tube extending to the cloaca (**Figure 47**Q). These patterns of expressions suggest a less ubiquitous role of the coatomer trafficking complex during development and greater spatial temporal regulation in a highly coordinated timely manner.

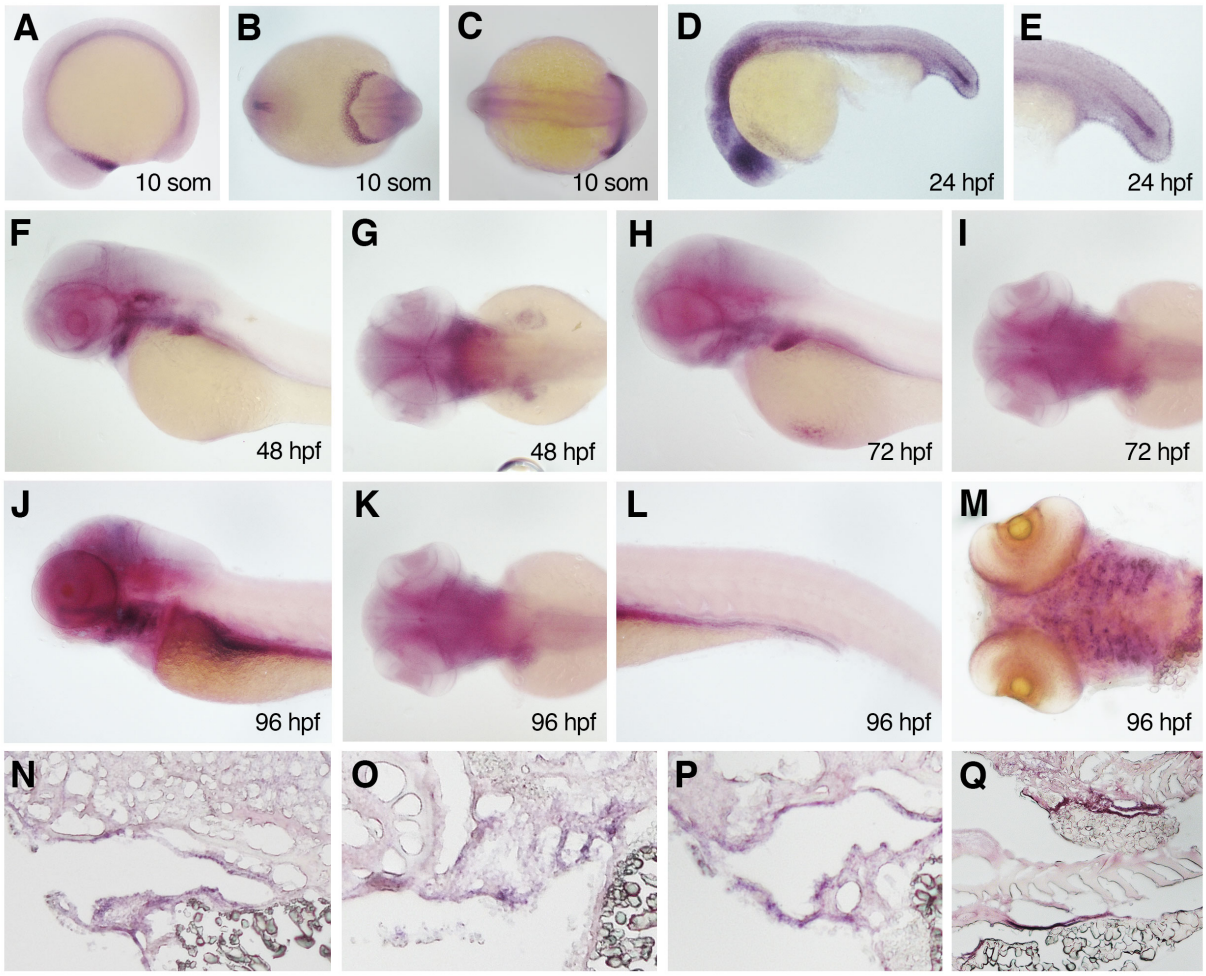

Figure 47. *copa* WISH analysis at different time points during craniofacial development.

(A-C) 10 somites; ventral and lateral views with clear expression at the polster and notochord.

(D) 24hpf with a zoomed view of the tail area (E) highlighting the posterior notochord expression.

(F-G) 48hpf lateral and ventral view showing expression in the pharyngeal arches, pectoral fin, liver bud and cranial sutures.

(H-I) 72hpf lateral and ventral view showing clear expression within the craniofacial region, liver bud, lining of the gut and cranial sutures.

(J-M) 96hpf ventral, lateral, zoomed tail, zoomed head views with clear expression within the craniofacial cartilage structures, liver, gut lining and swim bladder.

(N-P) Sagittal sections of the craniofacial region of a 96hpf embryo showing expression with the surrounding mesenchyme as oppose to within the chondrocytes.

(Q) Sagittal section of the stomach showing strong expression within the epithelial lining.

5.2.5. copa knockout results in failure of NCC specification and differentiation

To determine if early NCC specification and differentiation is affected in *copa* mutants, we carried out molecular analysis of key neural crest genes at the 10 somites stage (onset of NCC migration) and 48hpf (prior to craniofacial morphogenesis). Analysis of early NCC markers *sox9a, sox10* (NCC migration and survival), *foxd3* (NCC induction and specification) and *dlx2a* (NCC migration, survival and differentiation) at 10-somites stage in the *copa* mutants was largely unaffected with similar expression patterns (**Figure 48**). Note: we performed gene expression analysis on the whole clutch for each marker in order to conserve mendelian ratio. These embryos with corresponding expression pattern were then confirmed by genotyping.

In 48hpf WT embryos, *sox9a* expression in WT localizes to the preformed ethmoid plate, pharyngeal arches, cranial sutures and pectoral fin. However, in *copa* mutant, there appears to be a greater expression of *sox9a* (**Figure 48**D). *sox10* expression in WT is expressed within the pharyngeal arches and otic vesicle by 48hpf (**Figure 48**G). *copa* mutants did not show any increase in distribution pattern of *sox10* expression, with extensive ectopic expression within the melanocytes throughout the embryo and strong expression within the pharyngeal arch (**Figure 48**H).

To assess NCC induction and development, we assess the expression of *forkhead box D3* (*foxd3*). *foxd3* is a critical gene for NC development including survival, and maintenance of NC progenitor pools (Montero-Balaguer et al., 2006, Dottori et al., 2001, Teng et al., 2008). In WT, at 48hpf, *foxd3* expression appears within the cranial satellite glia associated with the cranial ganglia within the pre otic and post otic placodes (**Figure 48**K). In *copa* mutants however, this expression pattern appears greater and stronger especially within the cranial ganglia (**Figure 48**L).

We looked at the expression of *dlx2a*, a gene key in NCC migration, survival, differentiation of CNCC into sensory ganglia and maturation of craniofacial cartilage elements. In WT, *dlx2a* expression at 48hpf appears within the gill arches, otic vesicle, mandibular and hyoid arches as well as the diencephalon anteriorly (**Figure 48**O). In *copa* mutant, we observed greater expression of *dlx2a* (**Figure 48**P).

Overall, we observed a change in NCC marker patterns by 48hpf with stronger expressions of *sox9a*, *foxd3* and *dlx2a* and ectopic expression of *sox10* in *copa* mutant. These suggests that *copa* mutation seem to affect early NCC development.

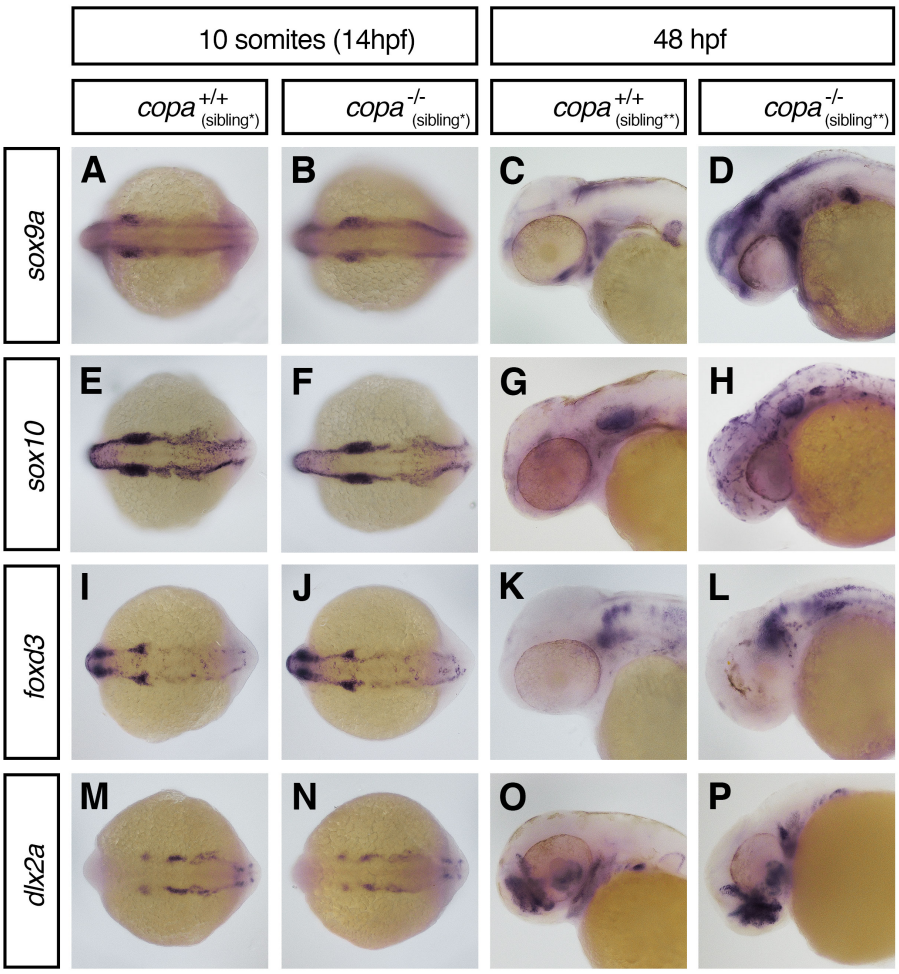

Figure 48. WISH of NCC markers in *copa* mutant at 10 somites and 48hpf.

(A-D) *sox9a*, (E-H) *sox10*, (I-L) *foxd3*, and (M-P) *dlx2a* expression levels in *copa* mutant compared to WT sibling within the same clutch.

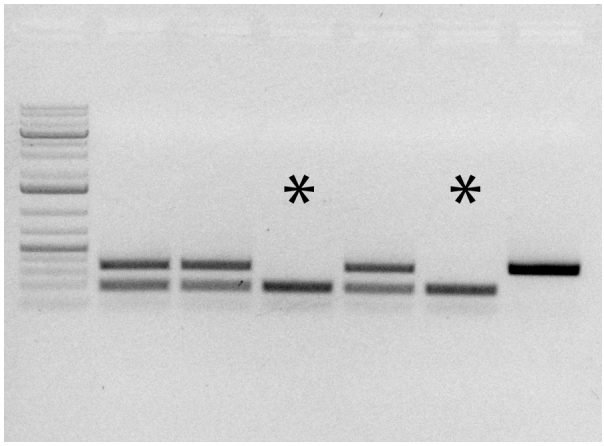

Figure 49. *copa* WISH genotyping.

Following in situ hybridization, embryos at 10 somites (in figure 34) were genotyped to ensure homozygocity due to similar expression pattern. Above is an example gel electrophoresis for the *sox9a* clutch where 7 embryos were imaged and then subsequently genotyped. Two homozygotes were identified in the genotyping experiment and therefore the previous figure represented this result.

5.2.6. Upregulation of UPR genes in copa mutant

Protein folding within the ER is extremely sensitive to altered changes within its microenvironment such as nutrient status, protein synthesis or external pathogenic stimuli (Wang and Kaufman, 2014). Perturbations in protein folding cause an accumulation of unfolded or misfolded proteins leading to ER stress (Sovolyova et al., 2014). Trafficking defects has also been described to induce ER stress by disrupting the ER protein-folding environment (Sovolyova et al., 2014). The build-up of ER stress causes the activation of the unfolded protein response (UPR) system, a critical signalling pathway in maintaining productive ER protein folding and cellular stress. The UPR pathway has been described in various pathological diseases such as tumorigenesis (Kim et al., 2012, Scriven et al., 2009, Wang and Kaufman, 2014) and in early development (Coutinho et al., 2004).

(BIP; also known as GRP78 and HSP5A), a binding immunoglobulin protein has been described as being important in the UPR activation cascade. Misfolded proteins bind to BIP and the reduction in free BIP levels in turn induces further transcription of *BIP* and the activation of the UPR pathway (Kozutsumi et al., 1988). This activation causes a transient attenuation of protein synthesis, increases protein trafficking through the ER, protein folding, and increased protein degradation pathway and autophagy. If the ER stress exceeds these adaptive responses and protein—folding defects are not resolved, cells will enter apoptosis (Kozutsumi et al., 1988).

The UPR has several parallel signalling branches, two of which focused on this study: 1) inositol-requiring protein (IRE1a)-X-box binding protein (XBP1) and 1) activating transcription factor 6a (ATF6a). IRE1a is a type 1 transmembrane protein with a cytosolic serine/threonine kinase domain. When not stressed, HSP90 and HSP72 bind to IRE1a cytosolic domain to stabilize it (Gupta et al., 2010, Marcu et al., 2002) and BIP binds to IRE1a luminal domain to prevent dimerization. During ER stress, misfolded proteins will bind to BIP, thereby releasing IRE1a for autophosphorylation and oligomierzation that in turns activates its kinases to cleave *Xbp1* mRNA. This cleavage removes a 26-base intron to create a transcriptionally active form of Xbp1 that then enters the nucleus to regulate target genes and enhance protein folding and trafficking (Calfon et al., 2002).

ATF6 is another transmembrane protein that under non-stressed conditions remains within the ER through its interaction with BIP (Guan et al., 2009, Ye et al., 2000). During ER

stress, ATF6 is released from BIP and traffics to the Golgi apparatus for processing by protease and then activate the regulated intramembrane proteolysis process. Other evidence has also shown that upon induction of ER stress, ATF6 induces BIP that binds to unfolded proteins and relieve the stress (Guan et al., 2009, Ye et al., 2000).

Since these genes are important in the UPR pathway, we examined mRNA transcript levels of *bip*, *ire1a* and *atf6a* (a zebrafish duplicate gene of *ATF6)* in 48hpf *copa* mutant homozygotes and found statistically significant upregulation of these genes compared to WT (**Figure 50**). Therefore, loss of *copa* can be seen to induce a stress response.

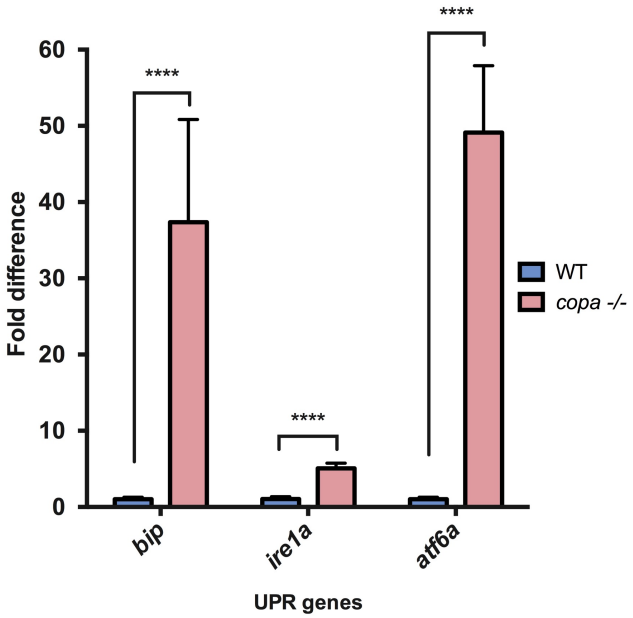

Figure 50. Upregulation of UPR pathway genes in *copa* mutant.
qPCR on *bip*, *ire1a* and *atf6a*, essential genes in the UPR signalling pathway. 48hpf *copa* mutant homozygotes cDNA were used for analysis. Ubiquitous housekeeping gene eif1a was used as an internal WT stage-matched controls. Two-paired T-test was used where **** indicates $p<0.0001$.

5.2.7. Tissue-specific CRISPR copa knockout

Early embryonic lethality represents a major hurdle in assessing craniofacial development that only starts around 55hpf. In fact, in zebrafish, it has been estimated that over 1400 genes are embryonic lethal before 55 hpf (Amsterdam et al., 2004). Therefore, in this circumstance, whole gene knockout using the $copa^{hi1872Tg}$ mutant may not be informative. We then sought to overcome the early death of $copa^{hi1872Tg}$ mutants attributed to failure in notochord differentiation by generating NCC-specific knockout of *copa.* Additionally, this will enable us to address cell autonomy questions. To achieve this, we use needed to

generate a spatio-temporal loss-of-function mutant line. Therefore, we combined the CRISPR/Cas9 gene editing technology as well as the Cre-lox system to spatio-temporally induce indel mutations (see Methods and Materials).

5.2.7.1. Limitations of other existing gene-silencing methods in zebrafish

In zebrafish, transient knockdown of a gene using morpholino enables assessment of loss-of-function in embryos (Nasevicius and Ekker, 2000). Morpholinos acts by binding to the transcription site or splice sites of pre mRNAs, thus blocking translation or splicing of the mRNA (Summerton and Weller, 1997). However, morpholinos present their own limitations, with nonspecific toxicity and off-target effects, limiting its utilization (Eisen and Smith, 2008). Additionally, morpholinos functions for about 3 days where its effects then taper off, thus precluding studies in older embryos and adults.

Other gene editing methods have been employed including Zinc-finger nucleases (ZFN) and transcription activator-like effector nucleases (TALEN) (Miller et al., 2011, Urnov et al., 2005). These are enzymes engineered to cleave specific DNA sequences by inducing double-strand breaks and activating the repair mechanism via non-homologous end joining. Even though these methods allow loss-of-function studies in both embryos and adults through stable mutant line generations, the design of new nuclease is incredibly tedious, racking in high cost and compounded by its low mutation efficiency.

The CRISPR/Cas9 gene editing technology uses just a single endonuclease, Cas9 to target a specific sequence within the genome. One of the many advantages of CRISPR/Cas9 to the other methods includes an ease of use and high efficiency, making it a fundamental tool to easily assess loss-of-function phenotype (Jinek et al., 2012). This improved specificity of mutagenesis uses dimeric RNA-guided Folk nuclease and with an optimized CRISPR-associated 9 (Cas9) that also reduces off-target effects (Jinek et al., 2012). The codon-optimized Cas9 nuclease in zebrafish has such high efficiency, that biallelic mutagenesis can be achieved in the F0 generation, allowing assessment of phenotype in the injected embryos (Hwang et al., 2013). Engineered gRNAs comprises of a 20-nucleotide complementary to the target DNA sequence with a 3’ motif that forms a secondary structure that interacts with the Cas9 endonuclease. The Cas9 loads the gRNA and search the genome for the complementary target sequence. When the sequence is followed by a proto-spacer adjacent motif (PAM), Cas9 will cleave the DNA within the gRNA seed

(Sternberg et al., 2014). This cleavage causes a double strand break within the genome. This break is repaired most likely by alternative nonhomologous end joining (also called NHEJ), which favours apparition of mutations; insertions, or deletions (indels). Therefore, if these indels occur within coding sequences, the targeted gene may be disrupted for example through the introduction of frameshifts of early stop codons.

However, to allow spatiotemporal control over gene inactivation, a new tissue-specific CRISPR/Cas9 knockout has been employed by taking advantage of the conditional Cre/lox technology (Mosimann et al., 2011, Ablain et al., 2015). Successful disruption of the *urod* and *mitfa* gene showed that the CRISPR/Cas9 knockout technology could be spatially controlled in blood lineage in zebrafish (Ablain et al., 2015).

5.2.7.2. Generation of copa CRISPR knockout line

Prior to generating tissue-specific loss of function, we tested the guide RNAs (gRNA) by generating whole organism knockouts with the designed gRNA. Using CHOPCHOP (hyyps://chopchop.rc.fas.harvard.edu) prediction algorithm, a gRNA for *copa* was designed (on exon 2) to contain a 20 bp target sequence with two GG residues at the 5' end for efficient transcription from the T7 promoter and ends with the PAM NGG for the efficient Cas9 binding (**Figure 51**). The seed gRNA is then cloned into the pDR274 vector that contains the gRNA scaffold and a T7 promoter.

The desired single targeting gRNA is then generated by *in vitro* transcription with a T7 promoter after linearizing the pDR274 plasmid and subsequently purified. The mix of gRNA and Cas9 RNA was co-injected into one-cell staged embryos to induce RNA-guided targeted DNA double-strand breaks mediated by the codon optimized Cas9 enzyme. The injected F0 were then screened to observe the efficiency of the gRNA. This was achieved by extracting DNA from the embryos 24-48hpf and by performing microsatellite DNA fragment analysis following PCR amplification of the region. Here, the WT fragment is 285 bp and the mutant allele we have successfully generated is 275 bp, thus potentially a 10 bp deletion has been incurred (**Figure 51**B). Further cloning experiments will elucidate the nucleotide deleted from the allele. This will be achieved by ligating the amplified PCR product from the identified heterozygote into a pGEM-T-easy vector and following selection of positive colonies, subjected to sequencing to identify the deletion.

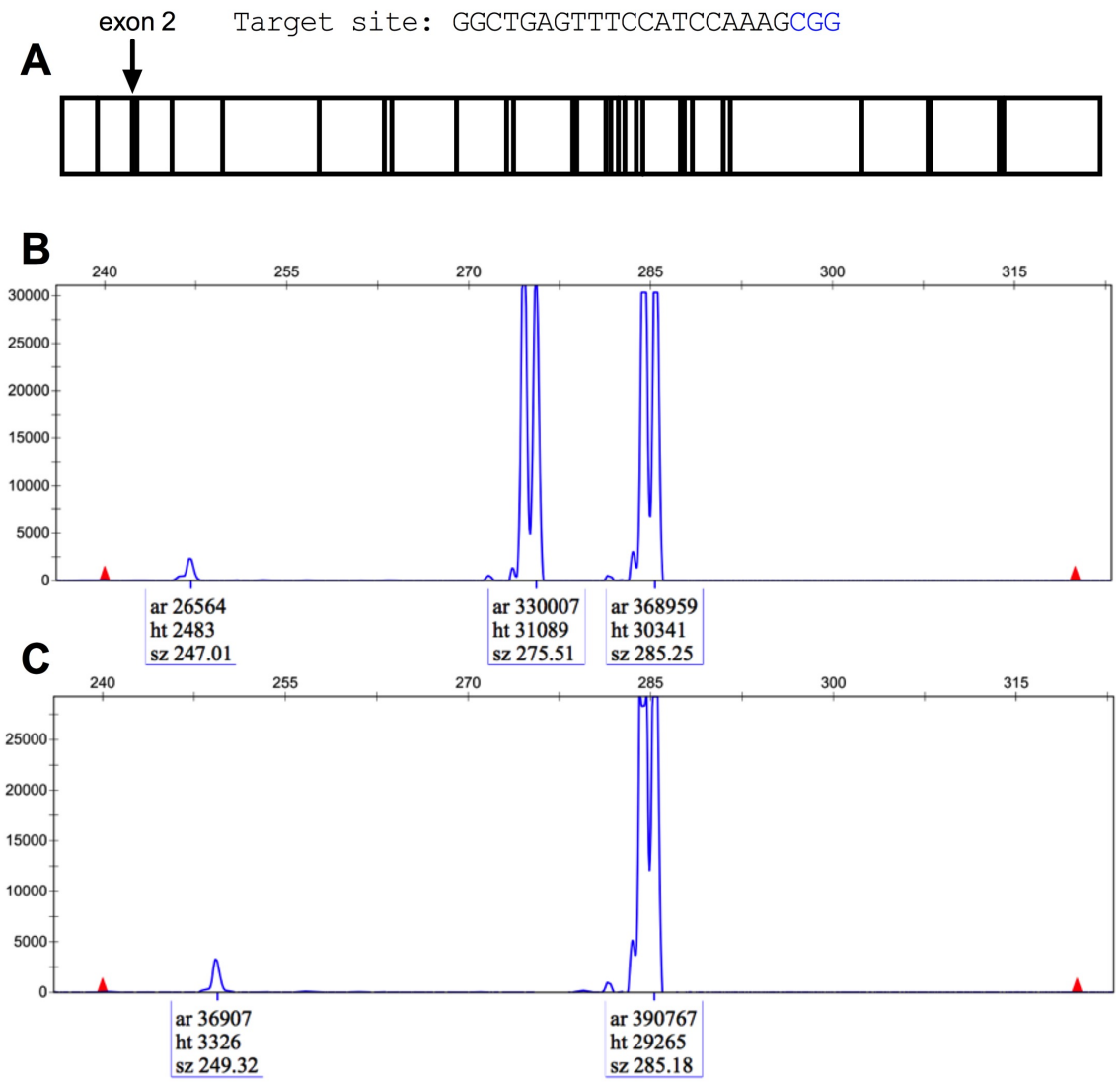

Figure 51. *copa* CRISPR target site and microsatellite DNA fragment analysis of mutant line generation.

(A). Target site generated from online bioinformatics software and target site at exon 2 chosen. PAM sites indicated in blue highlight. (B, C). Microsatellite DNA fragment analysis of F0 adult (B) mutant and (C) WT control. WT peak at 285 bp while mutant allele peak at 275 bp indicating a potential 10 bp deletion incurred by CRISPR/Cas9.

5.2.7.3. Generation of sox10-specific CRISPR knockout line

Having determined that the target gRNA induces an effective indel, we then used the target sequence to construct vectors based on the Tol2 transposase (Gateway) technology (Kawakami et al., 2004). The Gateway technology allows the Cas9 sequence codon-optimized for zebrafish to be inserted with a tissue-specific promoter. For the final gateway construct, we used three separate approaches: 1) using a *ubi*:hulk (*ubi*:loxP-STOP-loxP-GFP), 2) *ubi*:switch (*ubi*:loxP-GFP-STOP-loxP) (Mosimann et al., 2011) and

10X Upstream activating sequence (UAS) as promoters within the p5'. We then cloned the CRISPR seed sequence under the control of a zebrafish U6 promoter at the 5' end of the gRNA scaffold into a destination *U6*:gRNA cassette with a heart transgenesis marker (*cmlc*:GFP) (Ablain et al., 2015). A Gateway reaction then allows the assembly of a Cas9 sequence (pME) under the control of the promoters (p5E') and followed by poly-A (p3E') inserted into the destination *U6*:gRNA vector. Three separate constructs were generated to address the need of three different promoters. These constructs were subsequently injected with Tol2 mRNA (20 ng/uL) into one cell-stage embryos (**Figure 52**).

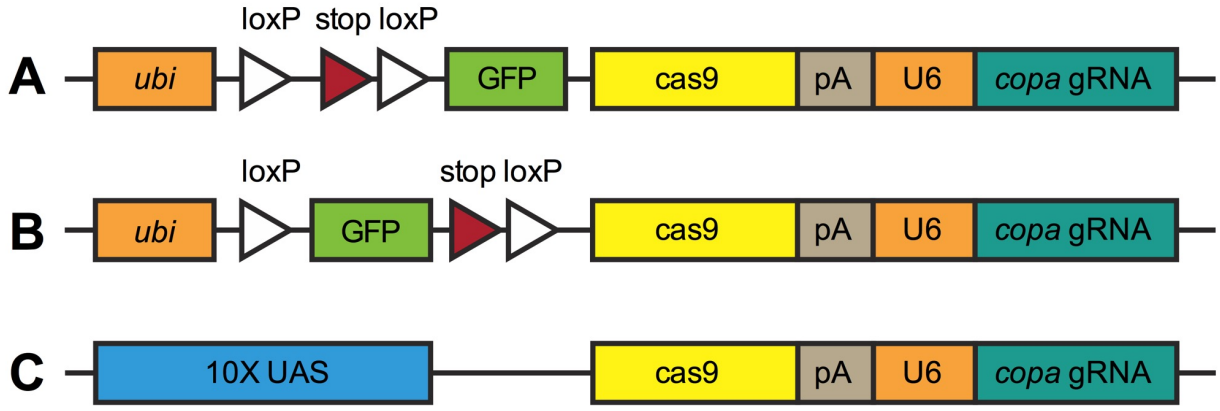

Figure 52. Tissue specific CRISPR constructs strategies.

(A). Ubiquitous switch from dark to GFP (*ubi*:hulk) upon Cre induction to drive cas9 and U6 promoter transcribing the *copa* gRNA. (B). Ubiquitous switch GFP to dark (*ubi*:switch) upon Cre induction to drive copa gRNA. (C). Upstream activating sequence (UAS) promoter 10X repeat sequence during the cas9/*copa* gRNA construct. UAS promoter will activate upon a tissue specific gal4.

The use of the *ubi*:switch/*ubi*:hulk/UAS promoters is to take advantage of the tamoxifen-inducible Cre/lox system by crossing a tissue specific Cre-ERT2 stable fish line (in this case, *sox10*:CreERT2) to allow spatiotemporal assessment of *copa* gene function during craniofacial development. As a positive control, we crossed the CRISPR *copa* fish line with a *ubi*:CreERT2 line to determine if tamoxifen treatment will recapitulate the phenotype of the whole-organism CRISPR knockout and the *copa*^{hi1872Tg} mutant line. Additionally, other tissue specific lines made in our laboratory such as a *krt4*:creERT2 line enables assessment of *copa* within epithelial cells. This will enable us to answer key questions regarding the requirements of *copa* within craniofacial chondrocytes or surrounding mesenchyme.

5.3. Discussion

Intracellular trafficking systems, including COPI, COPII and clathrin complexes are fundamental in maintaining cellular homeostasis. Various disorders such as cranio-lenticulo-sutural dysplasia and osteogenesis imperfect due to mutations in the COPII complex have underscored the importance of these intracellular transport mechanisms. Only recently mutations in components of *COPI* have been found to cause germline diseases. A mutation in *COPA*, which encodes the α-COP subunit of COPI was described in patients with hereditary autoimmune-mediated lung disease and arthritis (Watkin et al., 2015). They showed that there was impaired binding of proteins targeted for retrograde Golgi to ER transport. This subsequently led to ER stress and upregulation of Th17 priming cytokines, an effector T cell population implicated in autoimmunity. A more recent paper linked a loss-of-function heterozygous mutation in *ARCN1*, which encodes the delta-COP subunit of COPI (Izumi et al., 2016). They found that *ARCN1* deficiency led to defective type 1 collagen transport and therefore a reduction in collagen secretions leading to skeletal defects (including micrognathia and microcephaly). Like the mutation in *COPA*, the authors found that the *COPD* mutation disrupted intracellular trafficking causing an accumulation of proteins within the ER and upregulation of the unfolded protein response (UPR) pathway. However, the authors noted that ARCN1 is directly responsible for the intracellular transport of type 1 collagen and that the collagen defect is not secondary to the UPR upregulation. This paper appeared to contradict findings from previously published work showing COPI loss-of-function using *copa* morpholino injections (Izumi et al., 2016). Izumi and colleages also compared COPI-knockdown fish to a *sec23a*-deficient fish (part of the COPII mechanism) and found that *copa* does not have a role in trafficking of ECM proteins during chondrogenesis (Lang et al., 2006). However, ventral craniofacial structures and the neurocranium were noticeably smaller and shorter than their WT sibling. Although patterning is unaffected, hypertrophy and maturation of chondrocytes could account for the smaller size, but was not addressed in the paper. Additionally, previous studies have found a significant difference between morphant-induced phenotype (morpholino knockdown) versus mutant-induced phenotype (knock-out) (Kok et al., 2015). In fact, up to 80 percent of published morphant defects with the Sanger Zebrafish Mutation Project were not observed in the mutant embryos (Kok et al., 2015). Rossi and colleagues found that there was genetic compensation in knockouts compared to gene knockdowns that could account for the large phenotypic differences (Rossi et al., 2015). However, more than a decade of morpholino use in various

developmental model organisms have transformed the field of developmental biology. While new gene editing nucleases has great promise, it is still at its infancy and when use in conjunction with other approaches like morpholinos can provide better conclusion on functional relevance (Blum et al., 2015). Therefore, this project aims to elucidate *copa* requirements in craniofacial chondrogenesis by generating neural crest cell specific knockouts and addressing the role of trafficking in neural crest cell induction, migration and specification.

5.3.1. hi1872Tg mutant disrupts copa function

Using a viral insertion mutant line, we found that the *hi1872Tg* mutant successfully recapitulated the homozygote phenotype from an ENU mutagenesis (*sneezy*) previously described to encode the *copa* subunit (Coutinho et al., 2004). The coatomer complex consists of seven polypeptides that form the coat of COPI vesicles. These vesicles are important for membrane trafficking in the secretory pathway and essential for Golgi functions. Without it, normal transport of proteins from the ER and Golgi is disrupted and cells undergo apoptosis (Schekman and Orci, 1996). Previous studies as well as the *in situ* assays in this project have characterized early expression profiles of *copa* and showed that it is provided maternally and ubiquitously expressed within the chordamesoderm and notochord (Coutinho et al., 2004). Once the notochord has differentiated, later expression time points reveal strong levels within metabolically active organs such as the liver as well as the pharyngeal arches. Interestingly, given its essential function in intracellular processes, *copa* does not remain ubiquitously expresses. Instead, it appears to be regulated in a spatiotemporal manner. Previously reported expression analysis of *copb1, copb', cope, copd* and *copg2* share a similar profile. However, *copz* differed from the observed expression of the other coatomer subunits. *copz1* does not appear to be upregulated within the chordamesoderm and notochord during development. A *copz1* insertional mutagenesis line showed no defects in the notochord or melanocytes but presented with a degenerate eye (Golling et al., 2002). Although we cannot rule out that other coatomer subunits are not involve in eye development due to early lethality, it is interesting that *copz* is dispensible for notochord development. It is possible that copz2 compensates for the loss of *copz1*. Double knockout mutant lines will highlight this possibility. Therefore, to underscore the importance of COPI requirements during craniofacial development; we generated tissue specific knockout lines taking advantage of both the Tol2 transgene and Cre/lox system.

5.3.2. Tissue specific knockout of copa using CRISPR/Cas9

The advent of new genome editing technologies has generated waves of excitement within the scientific community. The ability to target any part of the genome with ease using RNA guided endonucleases has given investigators unprecedented rapid access to study gene function and its regulatory components (Cong et al., 2013, Jinek et al., 2012, Zhang et al., 2011). In addition, their potential use as therapeutic tools has been demonstrated in several studies using precise homologous recombination based editing (Perez et al., 2008, Shwartz et al., 2012, Yin et al., 2014). In the CRISPR/Cas9 system, Cas9 make targeted double stranded DNA breaks that is then repaired using either homogous recombination or non-homogous end joining (NHEJ) (Jinek et al., 2012). The latter is the predominant repair pathway in cells, which is a highly inefficient process that usually leads to mutagenic changes due to small insertions or deletions. The CRISPR technology has now become the genome editing tool of choice predominantly due to the low cost, high efficiency and ease of synthesis, access and use (Mali et al., 2013, Jinek et al., 2012).

Tissue specific CRISPR/Cas9 in zebrafish represents a recent advancement in zebrafish genome editing (Ablain et al., 2015). The targeting vector contains a tissue-specific promoter driving Cas9 towards the gRNA that is specific for the gene. The advantages of this system with *copa* gene is that it allows for: 1) the generation of stable zebrafish lines with a tissue-specific gene knockout that can be spatially controlled, 2) the assessment of cell autonomy in loss-of-function studies and 3) avoidance of embryonic lethality due to notochord defects. To test the potential of this approach, we first tested the *copa* gRNA designed to target exon 2 with a predicted truncation and disruption of protein function. The results showed that the CRISPR gRNA can make targeted breaks at a high efficiency. Therefore we inserted this gRNA with the *ubi*:switch promoter action. The reason for not using a *sox10* promoter was to act as a control for the efficiency of tamixofen induction. By inducing as early as 6hpf, we may be able to recapitulate the whole-organism loss-of-function and reproduce the previous phenotype as previously described (Coutinho et al., 2004) as recovered in the T7 CRISPR knockout system line. This will serve as a landmark to determine the suitable concentration and duration of tamoxifen induction as well as the efficiency of the tissue-specific vector construct. From here, we could perform spatio-temporal loss-of-function of *copa* on NCC during craniofacial development. Preliminary analyses from gene expression of *sox9a, sox10, dlx2a* and *foxd3* shows that NCC induction is primarily unperturbed and migration does not appear to be affected at 10 somites.

However, 48hpf analysis shows marked upregulation of all 4 gene expressions. A potential explanation lies in the activation of the stress response pathway/unfolded protein response (UPR) during development when COPI mechanism is disrupted.

5.3.3. Loss and gain of function in COPA leads to ER stress

Previous studies have showed that loss of COPI function in response to Brefaldin A treatment causes a disruption in the secretory organelle structure (Coutinho et al., 2004). This led to a build-up of unfolded protein and the activation of the UPR pathway that ultimately triggers the stress-response mechanisms, the apoptotic and authophagy pathways (Coutinho et al., 2004). This finding was also true in *COPA* variants in patients with autoimmune-mediated lung disease and arthritis. Lung biopsies in COPA deficient patients showed evidence of increase in molecular chaperone binding immunoglobulin protein (BiP), a key factor and indicator of ER stress (Watkin et al., 2015). They consolidated this finding by performing siRNA *COPA* knock-down experiments in Human Embryonic Kidney (HEK) cells and observed that reducing *COPA* expression led to ER stress and increase in *BiP* expression. Interestingly, when they then overexpressed human mutant variants of *COPA*, they found a similar elevation of *BiP* compared to WT (Watkin et al., 2015). These findings are alighed with our own results that also showed an upregulation of UPR genes in 48hpf *copa* mutants.

Similarly, the loss of *ARCN1*, which encodes *COPD* resulted in the overexpression of ER stress response genes, *ATF4, DDIT3* and *HSPA5* (Izumi et al., 2016). Interestingly, when they treated skin fibroblast line with thapsigargin, an inhibitor of the ER Ca ATPase (Namba et al., 2007) and tunicamycin, an inhibitor of glycoprotein synthesis (Oslowski and Urano, 2011), artificial ER stress was achieved and triggered *ARCN1* overexpression, although the amount of *ARCN1* remained unchanged. This suggests the increase *ARCN1* turnover during stress response. This effect was also observed in Brefaldin treated zebrafish embryos where *copa* mRNA expression was increased within the notochord (Coutinho et al., 2004). These suggest that COPI may play a major role in ameliorating the induction of ER stress response. Therefore, the reduction in COPI mechanism will trigger ER stress response and when the rate of protein synthesis exceeds the capacity of proteins folding and proteins degradation machinery, cell death occurs (Sovolyova et al., 2014). This may explain why all 4 genes; *sox9a*, *sox10*, *foxd3* and *dlx2a* were seen to be overexpressed in our *in situ* experiments. There may be over-activation of these genes to

compensate for the lack of specification. This is more evident with *sox10* where ectopic expression is observed within presumed melanocytes. It may be worth determining the expression of *microphthalmia-associated transcription factor (mitf)*, a gene involved in melanogenesis.

Interestingly expressions of these genes (*sox9a*, *sox10*, *foxd3* and *dlx2a)* at 10 somites were unaffected in our experiments. These results and the *copa* expression time course analysis may indicate that cope may not have a major role in early NCC development. As we have shown, *copa* is highly expressed in the forebrain and notochord, but it is not until 48hpf that its expression is seen within the pharyngeal arches and then, the craniofacial structures. This expression has been shown in previous studies (Coutinho et al., 2004). By 24hpf, an elevated demand of coatomer has been shown to be required to accustomed to the high secretory demand of notochord cells as seen by the upregulation of *copa* in the chordamesoderm (Coutinho et al., 2004). This therefore led to the earlier appearance of the defects. Therefore, the tissue specific knockout will help shed light into specific requirements of COPI subunits in NCC development. In addition, knockouts of the UPR genes, in particular *bip,* will determine if the persistent overexpression of NCC genes we observed here is specific to COPI loss-of-function or whether the similar phenotype could be induced by disrupting the UPR pathway.

It is interesting how *copa* is regulated in a tissue specific and temporal manner. One would expect that an essential cellular trafficking function would be ubiquitously expressed during development. However, it may be that once sufficient coatomer subunits are made to form the COPI vesicles, these can be recycled rather than exhausting further efforts into manufacturing more cargo subunits. Therefore, increased requirements shifts from one tissue type to the other based on cellular demands during critical developmental stages.

5.4. Summary and future directions

Mutations affecting the trafficking mechanism have demonstrated essential and specific roles of coatomer during early development and craniofacial malformations. This project has concentrated on describing a novel viral insertional mutant, studying the effects of *copa* loss of function on NCC development and UPR pathway and finally development of a tissue-specific knockout CRISPR line. Though many questions remain to be answered, especially concerning the spatio-temporal role of COPI during NCC development and possible signalling pathways that acts through this mechanism, much has been learnt about trafficking during early development.

Future directions and link with Project 1 will include studying WLS retrograde transport via COPI and spatio-temporal control of Wnt secretion during craniofacial development. A recent study showed how Wnts are transported from the ER to the Golgi through WLS retrograde shuttling (Yu et al., 2014). They identified the basis for early step Wnt signalling where newly palmitoleated Wnts binds to WLS and moves from the ER to the plasma membrane via the Golgi. Subsequently, WLS is then recycled back using key elements of the ER-Golgi intermediate compartment. However, many questions remain such as whether the ER stores a pool of unused WLS to be used for recycling and if so, what is the half-life of WLS and what regulates WLS activity?

Retrograde trafficking is a growing area of scientific interest. COPI and COPII vesicles play clear roles during craniofacial development predominantly found to be due to failure of collagen deposition by developing chondrocytes. However, the tissue specific requirement of COPI vesicles opens the field to how other cells transport proteins and maintain tissue homeostasis. A recent RNAi screen identified ERGIC2 as a key component of the Golgi-ER pathway traffic used by exotoxins such as ricin, Shiga toxin and Pseudomonas (Moreau et al., 2011). This remarkable ability of bacteria to highjack the trafficking mechanism remains to be understood.

Chapter 6: Final summary and future directions

This thesis will hopefully shed some light onto the importance of Wnt signalling in patterning the cartilage anlage to direct future bone development. We have found that the non-canonical Wnt signalling pathway is key in orientating chondrocytes appropriately along their polarity lines. The alignment of cilia allows them to receive signals from the surrounding mesenchyme to activate the endochondral ossification process and transdifferentiation into osteoblasts. The lack of non-canonical Wnt signalling severely affects the way chondrocytes dynamically interact with each other, thereby affecting the normal stacking and intercalation process, key for lengthening and building the arch of the mandible. Previous work in the lab also showed that apart from the mandible, the maxilla is severely affected by this signalling pathway which could underlie a cause for orofacial clefting defects (such as cleft lip and palate). Future areas of research will include understanding the gene network involving various signalling pathways and transcription factors to control and fine tune the shape of the face that makes each of us unique. Modulating Wnt signalling by overexpressing and knocking out key Wnt genes followed by RNA-seq will help provide insights into the different genes regulated during craniofacial development.

The second take away message is the powerful model organism; the zebrafish in studying craniofacial defects. It represents a cheap, quick and reliable model to understand genotype-phenotype correlation which is an excellent translation tool for novel genes discovered in genome-wide studies. With a high homology to the human genome, organogenesis and development of various structures involves similar key genes and regulatory networks. Future areas of research will be using this model to perform large scale chemical screen to test for drugs that can potentially mitigate craniofacial defects during development. This forms the basis of functional biology by understanding gene causing diseases and through this, discover new drugs that can then be directly used for patient care.

Craniofacial development represents a complex field in developmental biology with many human malformations unexplained on both the genetic and mechanistic level. While most genetic studies focus on mutations in coding regions of important genes, an area vastly unexplored is the non-coding regions and cis-regulatory elements that influences

transcription factor bindings and ultimately the larger gene regulatory network that help specify a certain tissue. This for me is the real beauty in craniofacial developmental biology - the precise orchestration of transcription factors, enhancers/silencers and promoters to sculpt the face and produce a unique architectural masterpiece in every single individual. This represents an interesting work for future investigations. Functionally assessing non-coding gene variants and how human mutations (such as single nucleotide polymorphism) affects craniofacial development will help understand the role of 'junk DNA'. This will involve employing chromatin accessibility assays (such as ATAC-seq, DNAse1-seq), transcriptomics work (RNA-seq) and detailed bioinformatics analysis coupled with non-coding region knockouts to functionally test their significance.

Additionally, other open questions remain in the context of Wnt secretion. Such as, where exactly do Wnt proteins load onto cargos? How do cells recognize a fully loaded cargo versus empty cargo? How much Wnt can be loaded into one cargo? What differentiates anterograde and retrograde routes? How long do these vesicles or cargos last for and how many times can they be recycled prior to constructing a new one? Mechanisms of hijacking these cargos may provide new avenues for drug delivery intracellularly without the need for vectors. Furthermore, investigating where other parallel intracellular delivery mechanisms can help determine tissue-specific trafficking needs. Indeed, previous studies where removal of vesicle-bound Wnts only partially reduce Wnt activity suggesting other secretion routes are present (Gross et al., 2012).

In the context of endochondral ossification, further work looking at the crosstalk between Hedgehogs and Wnts remains to be explored. The newer concept of transdifferentiation of hypertrophic chondrocytes into osteoblast has been explored in the literature (Yang et al., 2014). This changes our view on how endochondral bone is formed and have important implications in bone regeneration. However, the underlying mechanisms which cause this molecular switch remain to be explored. Here, I implicate the non-canonical Wnts in making this switch by potential cross-talk with Indian Hedgehog signalling. Further work is required and may uncover downstream effectors which activate the transdifferentiation process.

Craniofacial development remains a niche yet complex research field. However, it is populated with exciting avenues to explore and provide insight into the evolutionary diversity across species.

References

ABLAIN, J., DURAND, E. M., YANG, S., ZHOU, Y. & ZON, L. I. 2015. A CRISPR/Cas9 vector system for tissue-specific gene disruption in zebrafish. *Dev Cell,* 32**,** 756-64.

ADAMS, D. S., KELLER, R. & KOEHL, M. A. 1990. The mechanics of notochord elongation, straightening and stiffening in the embryo of Xenopus laevis. *Development,* 110**,** 115-30.

AHN, Y., SANDERSON, B. W., KLEIN, O. D. & KRUMLAUF, R. 2010. Inhibition of Wnt signaling by Wise (Sostdc1) and negative feedback from Shh controls tooth number and patterning. *Development,* 137**,** 3221-31.

ALEXANDER, C., PILOTO, S., LE PABIC, P. & SCHILLING, T. F. 2014. Wnt signaling interacts with bmp and edn1 to regulate dorsal-ventral patterning and growth of the craniofacial skeleton. *PLoS Genet,* 10**,** e1004479.

AMSTERDAM, A., BURGESS, S., GOLLING, G., CHEN, W., SUN, Z., TOWNSEND, K., FARRINGTON, S., HALDI, M. & HOPKINS, N. 1999. A large-scale insertional mutagenesis screen in zebrafish. *Genes Dev,* 13**,** 2713-24.

AMSTERDAM, A., NISSEN, R. M., SUN, Z., SWINDELL, E. C., FARRINGTON, S. & HOPKINS, N. 2004. Identification of 315 genes essential for early zebrafish development. *Proc Natl Acad Sci U S A,* 101**,** 12792-7.

ANTHWAL, N., JOSHI, L. & TUCKER, A. S. 2013. Evolution of the mammalian middle ear and jaw: adaptations and novel structures. *J Anat,* 222**,** 147-60.

AUER, T. O. & DEL BENE, F. 2014. CRISPR/Cas9 and TALEN-mediated knock-in approaches in zebrafish. *Methods,* 69**,** 142-50.

BANZIGER, C., SOLDINI, D., SCHUTT, C., ZIPPERLEN, P., HAUSMANN, G. & BASLER, K. 2006. Wntless, a conserved membrane protein dedicated to the secretion of Wnt proteins from signaling cells. *Cell,* 125**,** 509-22.

BARLOWE, C., ORCI, L., YEUNG, T., HOSOBUCHI, M., HAMAMOTO, S., SALAMA, N., REXACH, M. F., RAVAZZOLA, M., AMHERDT, M. & SCHEKMAN, R. 1994. COPII: a membrane coat formed by Sec proteins that drive vesicle budding from the endoplasmic reticulum. *Cell,* 77**,** 895-907.

BASCH, M. L., BRONNER-FRASER, M. & GARCIA-CASTRO, M. I. 2006. Specification of the neural crest occurs during gastrulation and requires Pax7. *Nature,* 441**,** 218-22.

BEDNAREK, S. Y., RAVAZZOLA, M., HOSOBUCHI, M., AMHERDT, M., PERRELET, A., SCHEKMAN, R. & ORCI, L. 1995. COPI- and COPII-coated vesicles bud directly from the endoplasmic reticulum in yeast. *Cell,* 83**,** 1183-96.

BELENKAYA, T. Y., WU, Y., TANG, X., ZHOU, B., CHENG, L., SHARMA, Y. V., YAN, D., SELVA, E. M. & LIN, X. 2008. The retromer complex influences Wnt secretion by recycling wntless from endosomes to the trans-Golgi network. *Dev Cell,* 14**,** 120-31.

BETANCUR, P., BRONNER-FRASER, M. & SAUKA-SPENGLER, T. 2010. Assembling neural crest regulatory circuits into a gene regulatory network. *Annu Rev Cell Dev Biol,* 26**,** 581-603.

BHATT, S., DIAZ, R. & TRAINOR, P. A. 2013. Signals and switches in Mammalian neural crest cell differentiation. *Cold Spring Harb Perspect Biol,* 5.

BIRD, N. C. & MABEE, P. M. 2003. Developmental morphology of the axial skeleton of the zebrafish, Danio rerio (Ostariophysi: Cyprinidae). *Dev Dyn,* 228**,** 337-57.
BLUM, M., DE ROBERTIS, E. M., WALLINGFORD, J. B. & NIEHRS, C. 2015. Morpholinos: Antisense and Sensibility. *Dev Cell,* 35**,** 145-9.
BONFANTI, L., MIRONOV, A. A., JR., MARTINEZ-MENARGUEZ, J. A., MARTELLA, O., FUSELLA, A., BALDASSARRE, M., BUCCIONE, R., GEUZE, H. J., MIRONOV, A. A. & LUINI, A. 1998. Procollagen traverses the Golgi stack without leaving the lumen of cisternae: evidence for cisternal maturation. *Cell,* 95**,** 993-1003.
BOYDEN, L. M., MAO, J., BELSKY, J., MITZNER, L., FARHI, A., MITNICK, M. A., WU, D., INSOGNA, K. & LIFTON, R. P. 2002. High bone density due to a mutation in LDL-receptor-related protein 5. *N Engl J Med,* 346**,** 1513-21.
BRADLEY, E. W. & DRISSI, M. H. 2010. WNT5A regulates chondrocyte differentiation through differential use of the CaN/NFAT and IKK/NF-kappaB pathways. *Mol Endocrinol,* 24**,** 1581-93.
BRADLEY, E. W. & DRISSI, M. H. 2011. Wnt5b regulates mesenchymal cell aggregation and chondrocyte differentiation through the planar cell polarity pathway. *J Cell Physiol,* 226**,** 1683-93.
BRONNER, M. E. & LEDOUARIN, N. M. 2012. Development and evolution of the neural crest: an overview. *Dev Biol,* 366**,** 2-9.
BURNS, A. J. & DOUARIN, N. M. 1998. The sacral neural crest contributes neurons and glia to the post-umbilical gut: spatiotemporal analysis of the development of the enteric nervous system. *Development,* 125**,** 4335-47.
BURNS, A. J. & LE DOUARIN, N. M. 2001. Enteric nervous system development: analysis of the selective developmental potentialities of vagal and sacral neural crest cells using quail-chick chimeras. *Anat Rec,* 262**,** 16-28.
CALFON, M., ZENG, H., URANO, F., TILL, J. H., HUBBARD, S. R., HARDING, H. P., CLARK, S. G. & RON, D. 2002. IRE1 couples endoplasmic reticulum load to secretory capacity by processing the XBP-1 mRNA. *Nature,* 415**,** 92-6.
CALOS, M. P. 2016. Genome Editing Techniques and Their Therapeutic Applications. *Clin Pharmacol Ther*.
CHOE, C. P., COLLAZO, A., TRINH LE, A., PAN, L., MOENS, C. B. & CRUMP, J. G. 2013. Wnt-dependent epithelial transitions drive pharyngeal pouch formation. *Dev Cell,* 24**,** 296-309.
CICCIA, A. & ELLEDGE, S. J. 2010. The DNA damage response: making it safe to play with knives. *Mol Cell,* 40**,** 179-204.
CLEAVER, O. & KRIEG, P. A. 2001. Notochord patterning of the endoderm. *Dev Biol,* 234**,** 1-12.
CLEAVER, O., SEUFERT, D. W. & KRIEG, P. A. 2000. Endoderm patterning by the notochord: development of the hypochord in Xenopus. *Development,* 127**,** 869-79.
CLEMENT, A., WIWEGER, M., VON DER HARDT, S., RUSCH, M. A., SELLECK, S. B., CHIEN, C. B. & ROEHL, H. H. 2008. Regulation of zebrafish skeletogenesis by ext2/dackel and papst1/pinscher. *PLoS Genet,* 4**,** e1000136.
CLEVERS, H. & NUSSE, R. 2012. Wnt/beta-catenin signaling and disease. *Cell,* 149**,** 1192-205.
CONCANNON, M. R. & ALBERTSON, R. C. 2015. The genetic and developmental basis of an exaggerated craniofacial trait in East African cichlids. *J Exp Zool B Mol Dev Evol,* 324**,** 662-70.

CONG, L., RAN, F. A., COX, D., LIN, S., BARRETTO, R., HABIB, N., HSU, P. D., WU, X., JIANG, W., MARRAFFINI, L. A. & ZHANG, F. 2013. Multiplex genome engineering using CRISPR/Cas systems. *Science,* 339**,** 819-23.

COOMBS, G. S., YU, J., CANNING, C. A., VELTRI, C. A., COVEY, T. M., CHEONG, J. K., UTOMO, V., BANERJEE, N., ZHANG, Z. H., JADULCO, R. C., CONCEPCION, G. P., BUGNI, T. S., HARPER, M. K., MIHALEK, I., JONES, C. M., IRELAND, C. M. & VIRSHUP, D. M. 2010. WLS-dependent secretion of WNT3A requires Ser209 acylation and vacuolar acidification. *J Cell Sci,* 123**,** 3357-67.

COULY, G., CREUZET, S., BENNACEUR, S., VINCENT, C. & LE DOUARIN, N. M. 2002. Interactions between Hox-negative cephalic neural crest cells and the foregut endoderm in patterning the facial skeleton in the vertebrate head. *Development,* 129**,** 1061-73.

COUTINHO, P., PARSONS, M. J., THOMAS, K. A., HIRST, E. M., SAUDE, L., CAMPOS, I., WILLIAMS, P. H. & STEMPLE, D. L. 2004. Differential requirements for COPI transport during vertebrate early development. *Dev Cell,* 7**,** 547-58.

CURTIN, E., HICKEY, G., KAMEL, G., DAVIDSON, A. J. & LIAO, E. C. 2011. Zebrafish wnt9a is expressed in pharyngeal ectoderm and is required for palate and lower jaw development. *Mech Dev,* 128**,** 104-15.

CURTIN, J. A., QUINT, E., TSIPOURI, V., ARKELL, R. M., CATTANACH, B., COPP, A. J., HENDERSON, D. J., SPURR, N., STANIER, P., FISHER, E. M., NOLAN, P. M., STEEL, K. P., BROWN, S. D., GRAY, I. C. & MURDOCH, J. N. 2003. Mutation of Celsr1 disrupts planar polarity of inner ear hair cells and causes severe neural tube defects in the mouse. *Curr Biol,* 13**,** 1129-33.

DAY, T. F., GUO, X., GARRETT-BEAL, L. & YANG, Y. 2005. Wnt/beta-catenin signaling in mesenchymal progenitors controls osteoblast and chondrocyte differentiation during vertebrate skeletogenesis. *Dev Cell,* 8**,** 739-50.

DEPEW, M. J., LUFKIN, T. & RUBENSTEIN, J. L. 2002. Specification of jaw subdivisions by Dlx genes. *Science,* 298**,** 381-5.

DEREGOWSKI, V., GAZZERRO, E., PRIEST, L., RYDZIEL, S. & CANALIS, E. 2006. Notch 1 overexpression inhibits osteoblastogenesis by suppressing Wnt/beta-catenin but not bone morphogenetic protein signaling. *J Biol Chem,* 281**,** 6203-10.

DICKSON, C., SMITH, R., BROOKES, S. & PETERS, G. 1984. Tumorigenesis by mouse mammary tumor virus: proviral activation of a cellular gene in the common integration region int-2. *Cell,* 37**,** 529-36.

DIXON, M., DEED, R., ACLAND, P., MOORE, R., WHYTE, A., PETERS, G. & DICKSON, C. 1989. Detection and characterization of the fibroblast growth factor-related oncoprotein INT-2. *Mol Cell Biol,* 9**,** 4896-902.

DIXON, M. J., MARAZITA, M. L., BEATY, T. H. & MURRAY, J. C. 2011. Cleft lip and palate: understanding genetic and environmental influences. *Nat Rev Genet,* 12**,** 167-78.

DODONOVA, S. O., DIESTELKOETTER-BACHERT, P., VON APPEN, A., HAGEN, W. J., BECK, R., BECK, M., WIELAND, F. & BRIGGS, J. A. 2015. VESICULAR TRANSPORT. A structure of the COPI coat and the role of coat proteins in membrane vesicle assembly. *Science,* 349**,** 195-8.

DOTTORI, M., GROSS, M. K., LABOSKY, P. & GOULDING, M. 2001. The winged-helix transcription factor Foxd3 suppresses interneuron differentiation and promotes neural crest cell fate. *Development,* 128**,** 4127-38.

DOUDNA, J. A. & CHARPENTIER, E. 2014. Genome editing. The new frontier of genome engineering with CRISPR-Cas9. *Science,* 346**,** 1258096.
DOUGHERTY, M., KAMEL, G., GRIMALDI, M., GFRERER, L., SHUBINETS, V., ETHIER, R., HICKEY, G., CORNELL, R. A. & LIAO, E. C. 2013. Distinct requirements for wnt9a and irf6 in extension and integration mechanisms during zebrafish palate morphogenesis. *Development,* 140**,** 76-81.
DOUGHERTY, M., KAMEL, G., SHUBINETS, V., HICKEY, G., GRIMALDI, M. & LIAO, E. C. 2012. Embryonic fate map of first pharyngeal arch structures in the sox10: kaede zebrafish transgenic model. *J Craniofac Surg,* 23**,** 1333-7.
DRIEVER, W., SOLNICA-KREZEL, L., SCHIER, A. F., NEUHAUSS, S. C., MALICKI, J., STEMPLE, D. L., STAINIER, D. Y., ZWARTKRUIS, F., ABDELILAH, S., RANGINI, Z., BELAK, J. & BOGGS, C. 1996. A genetic screen for mutations affecting embryogenesis in zebrafish. *Development,* 123**,** 37-46.
DUPIN, E., REAL, C. & LEDOUARIN, N. 2001. The neural crest stem cells: control of neural crest cell fate and plasticity by endothelin-3. *An Acad Bras Cienc,* 73**,** 533-45.
EALBA, E. L., JHEON, A. H., HALL, J., CURANTZ, C., BUTCHER, K. D. & SCHNEIDER, R. A. 2015. Neural crest-mediated bone resorption is a determinant of species-specific jaw length. *Dev Biol,* 408**,** 151-63.
EAMES, B. F., AMORES, A., YAN, Y. L. & POSTLETHWAIT, J. H. 2012. Evolution of the osteoblast: skeletogenesis in gar and zebrafish. *BMC Evol Biol,* 12**,** 27.
EAMES, B. F., DELAURIER, A., ULLMANN, B., HUYCKE, T. R., NICHOLS, J. T., DOWD, J., MCFADDEN, M., SASAKI, M. M. & KIMMEL, C. B. 2013. FishFace: interactive atlas of zebrafish craniofacial development at cellular resolution. *BMC Dev Biol,* 13**,** 23.
EAMES, B. F. & SCHNEIDER, R. A. 2008. The genesis of cartilage size and shape during development and evolution. *Development,* 135**,** 3947-58.
EAMES, B. F., SHARPE, P. T. & HELMS, J. A. 2004. Hierarchy revealed in the specification of three skeletal fates by Sox9 and Runx2. *Dev Biol,* 274**,** 188-200.
EISEN, J. S. & SMITH, J. C. 2008. Controlling morpholino experiments: don't stop making antisense. *Development,* 135**,** 1735-43.
EKKER, S. C. & LARSON, J. D. 2001. Morphant technology in model developmental systems. *Genesis,* 30**,** 89-93.
EL-NACHEF, W. & GRIKSCHEIT, T. 2014. Enteric nervous system cell replacement therapy for Hirschsprung disease: beyond tissue-engineered intestine. *Eur J Pediatr Surg,* 24**,** 214-8.
FANTO, M. & MCNEILL, H. 2004. Planar polarity from flies to vertebrates. *J Cell Sci,* 117**,** 527-33.
FLORES, M. V., TSANG, V. W., HU, W., KALEV-ZYLINSKA, M., POSTLETHWAIT, J., CROSIER, P., CROSIER, K. & FISHER, S. 2004. Duplicate zebrafish runx2 orthologues are expressed in developing skeletal elements. *Gene Expr Patterns,* 4**,** 573-81.
FROMME, J. C., RAVAZZOLA, M., HAMAMOTO, S., AL-BALWI, M., EYAID, W., BOYADJIEV, S. A., COSSON, P., SCHEKMAN, R. & ORCI, L. 2007. The genetic basis of a craniofacial disease provides insight into COPII coat assembly. *Dev Cell,* 13**,** 623-34.
FROMMER, J. & MARGOLIES, M. R. 1971. Contribution of Meckel's cartilage to ossification of the mandible in mice. *J Dent Res,* 50**,** 1260-7.

GAIANO, N., AMSTERDAM, A., KAWAKAMI, K., ALLENDE, M., BECKER, T. & HOPKINS, N. 1996. Insertional mutagenesis and rapid cloning of essential genes in zebrafish. *Nature,* 383**,** 829-32.

GALLAHAN, D. & CALLAHAN, R. 1987. Mammary tumorigenesis in feral mice: identification of a new int locus in mouse mammary tumor virus (Czech II)-induced mammary tumors. *J Virol,* 61**,** 66-74.

GARBES, L., KIM, K., RIESS, A., HOYER-KUHN, H., BELEGGIA, F., BEVOT, A., KIM, M. J., HUH, Y. H., KWEON, H. S., SAVARIRAYAN, R., AMOR, D., KAKADIA, P. M., LINDIG, T., KAGAN, K. O., BECKER, J., BOYADJIEV, S. A., WOLLNIK, B., SEMLER, O., BOHLANDER, S. K., KIM, J. & NETZER, C. 2015. Mutations in SEC24D, encoding a component of the COPII machinery, cause a syndromic form of osteogenesis imperfecta. *Am J Hum Genet,* 96**,** 432-9.

GAUR, T., LENGNER, C. J., HOVHANNISYAN, H., BHAT, R. A., BODINE, P. V., KOMM, B. S., JAVED, A., VAN WIJNEN, A. J., STEIN, J. L., STEIN, G. S. & LIAN, J. B. 2005. Canonical WNT signaling promotes osteogenesis by directly stimulating Runx2 gene expression. *J Biol Chem,* 280**,** 33132-40.

GFRERER, L., DOUGHERTY, M. & LIAO, E. C. 2013. Visualization of craniofacial development in the sox10: kaede transgenic zebrafish line using time-lapse confocal microscopy. *J Vis Exp***,** e50525.

GLASS, D. A., 2ND, BIALEK, P., AHN, J. D., STARBUCK, M., PATEL, M. S., CLEVERS, H., TAKETO, M. M., LONG, F., MCMAHON, A. P., LANG, R. A. & KARSENTY, G. 2005. Canonical Wnt signaling in differentiated osteoblasts controls osteoclast differentiation. *Dev Cell,* 8**,** 751-64.

GLICK, B. S. & LUINI, A. 2011. Models for Golgi traffic: a critical assessment. *Cold Spring Harb Perspect Biol,* 3**,** a005215.

GLICK, B. S. & NAKANO, A. 2009. Membrane traffic within the Golgi apparatus. *Annu Rev Cell Dev Biol,* 25**,** 113-32.

GOLDSTEIN, D. J. & HOROBIN, R. W. 1974. Surface staining of cartilage by Alcian blue, with reference to the role of microscopic dye aggregates in histological staining. *Histochem J,* 6**,** 175-84.

GOLLING, G., AMSTERDAM, A., SUN, Z., ANTONELLI, M., MALDONADO, E., CHEN, W., BURGESS, S., HALDI, M., ARTZT, K., FARRINGTON, S., LIN, S. Y., NISSEN, R. M. & HOPKINS, N. 2002. Insertional mutagenesis in zebrafish rapidly identifies genes essential for early vertebrate development. *Nat Genet,* 31**,** 135-40.

GONG, Y., SLEE, R. B., FUKAI, N., RAWADI, G., ROMAN-ROMAN, S., REGINATO, A. M., WANG, H., CUNDY, T., GLORIEUX, F. H., LEV, D., ZACHARIN, M., OEXLE, K., MARCELINO, J., SUWAIRI, W., HEEGER, S., SABATAKOS, G., APTE, S., ADKINS, W. N., ALLGROVE, J., ARSLAN-KIRCHNER, M., BATCH, J. A., BEIGHTON, P., BLACK, G. C., BOLES, R. G., BOON, L. M., BORRONE, C., BRUNNER, H. G., CARLE, G. F., DALLAPICCOLA, B., DE PAEPE, A., FLOEGE, B., HALFHIDE, M. L., HALL, B., HENNEKAM, R. C., HIROSE, T., JANS, A., JUPPNER, H., KIM, C. A., KEPPLER-NOREUIL, K., KOHLSCHUETTER, A., LACOMBE, D., LAMBERT, M., LEMYRE, E., LETTEBOER, T., PELTONEN, L., RAMESAR, R. S., ROMANENGO, M., SOMER, H., STEICHEN-GERSDORF, E., STEINMANN, B., SULLIVAN, B., SUPERTI-FURGA, A., SWOBODA, W., VAN DEN BOOGAARD, M. J., VAN HUL, W., VIKKULA, M., VOTRUBA, M., ZABEL, B., GARCIA, T., BARON, R., OLSEN, B. R., WARMAN, M. L. & OSTEOPOROSIS-PSEUDOGLIOMA SYNDROME

COLLABORATIVE, G. 2001. LDL receptor-related protein 5 (LRP5) affects bone accrual and eye development. *Cell,* 107**,** 513-23.
GREINER, J. F., GRUNWALD, L. M., MULLER, J., SUDHOFF, H., WIDERA, D., KALTSCHMIDT, C. & KALTSCHMIDT, B. 2014. Culture bag systems for clinical applications of adult human neural crest-derived stem cells. *Stem Cell Res Ther,* 5**,** 34.
GROSS, J. C. & BOUTROS, M. 2013. Secretion and extracellular space travel of Wnt proteins. *Curr Opin Genet Dev,* 23**,** 385-90.
GROSS, J. C., CHAUDHARY, V., BARTSCHERER, K. & BOUTROS, M. 2012. Active Wnt proteins are secreted on exosomes. *Nat Cell Biol,* 14**,** 1036-45.
GUAN, D., WANG, H., LI, V. E., XU, Y., YANG, M. & SHEN, Z. 2009. N-glycosylation of ATF6beta is essential for its proteolytic cleavage and transcriptional repressor function to ATF6alpha. *J Cell Biochem,* 108**,** 825-31.
GUO, X., DAY, T. F., JIANG, X., GARRETT-BEAL, L., TOPOL, L. & YANG, Y. 2004. Wnt/beta-catenin signaling is sufficient and necessary for synovial joint formation. *Genes Dev,* 18**,** 2404-17.
GUPTA, S., DEEPTI, A., DEEGAN, S., LISBONA, F., HETZ, C. & SAMALI, A. 2010. HSP72 protects cells from ER stress-induced apoptosis via enhancement of IRE1alpha-XBP1 signaling through a physical interaction. *PLoS Biol,* 8**,** e1000410.
HALL, B. K. 2000. The neural crest as a fourth germ layer and vertebrates as quadroblastic not triploblastic. *Evol Dev,* 2**,** 3-5.
HAMBURGER, V. 1969. Hans Spemann and the organizer concept. *Experientia,* 25**,** 1121-5.
HAMMOND, C. L. & SCHULTE-MERKER, S. 2009. Two populations of endochondral osteoblasts with differential sensitivity to Hedgehog signalling. *Development,* 136**,** 3991-4000.
HARLAND, R. & GERHART, J. 1997. Formation and function of Spemann's organizer. *Annu Rev Cell Dev Biol,* 13**,** 611-67.
HARTLEY, J. L. 2003. Use of the gateway system for protein expression in multiple hosts. *Curr Protoc Protein Sci,* Chapter 5**,** Unit 5 17.
HARTMANN, C. 2006. A Wnt canon orchestrating osteoblastogenesis. *Trends Cell Biol,* 16**,** 151-8.
HARTMANN, C. & TABIN, C. J. 2000. Dual roles of Wnt signaling during chondrogenesis in the chicken limb. *Development,* 127**,** 3141-59.
HARTMANN, C. & TABIN, C. J. 2001. Wnt-14 plays a pivotal role in inducing synovial joint formation in the developing appendicular skeleton. *Cell,* 104**,** 341-51.
HEISENBERG, C. P., TADA, M., RAUCH, G. J., SAUDE, L., CONCHA, M. L., GEISLER, R., STEMPLE, D. L., SMITH, J. C. & WILSON, S. W. 2000. Silberblick/Wnt11 mediates convergent extension movements during zebrafish gastrulation. *Nature,* 405**,** 76-81.
HEUZE, Y., SINGH, N., BASILICO, C., JABS, E. W., HOLMES, G. & RICHTSMEIER, J. T. 2014. Morphological comparison of the craniofacial phenotypes of mouse models expressing the Apert FGFR2 S252W mutation in neural crest- or mesoderm-derived tissues. *Bone,* 63**,** 101-9.
HILL, T. P., SPATER, D., TAKETO, M. M., BIRCHMEIER, W. & HARTMANN, C. 2005. Canonical Wnt/beta-catenin signaling prevents osteoblasts from differentiating into chondrocytes. *Dev Cell,* 8**,** 727-38.

HOCHGREB-HAGELE, T., KOO, D. E. & BRONNER, M. E. 2015. Znf385C mediates a novel p53-dependent transcriptional switch to control timing of facial bone formation. *Dev Biol,* 400**,** 23-32.
HORTON, R. M., HUNT, H. D., HO, S. N., PULLEN, J. K. & PEASE, L. R. 1989. Engineering hybrid genes without the use of restriction enzymes: gene splicing by overlap extension. *Gene,* 77**,** 61-8.
HUANG, X. & SAINT-JEANNET, J. P. 2004. Induction of the neural crest and the opportunities of life on the edge. *Dev Biol,* 275**,** 1-11.
HULSEY, C. D., FRASER, G. J. & STREELMAN, J. T. 2005. Evolution and development of complex biomechanical systems: 300 million years of fish jaws. *Zebrafish,* 2**,** 243-57.
HWANG, W. Y., FU, Y., REYON, D., MAEDER, M. L., TSAI, S. Q., SANDER, J. D., PETERSON, R. T., YEH, J. R. & JOUNG, J. K. 2013. Efficient genome editing in zebrafish using a CRISPR-Cas system. *Nat Biotechnol,* 31**,** 227-9.
ICHIKAWA, Y., WATAHIKI, J., NAMPO, T., NOSE, K., YAMAMOTO, G., IRIE, T., MISHIMA, K. & MAKI, K. 2015. Differences in the developmental origins of the periosteum may influence bone healing. *J Periodontal Res,* 50**,** 468-78.
IRION, U., KRAUSS, J. & NUSSLEIN-VOLHARD, C. 2014. Precise and efficient genome editing in zebrafish using the CRISPR/Cas9 system. *Development,* 141**,** 4827-30.
IZUMI, K., BRETT, M., NISHI, E., DRUNAT, S., TAN, E. S., FUJIKI, K., LEBON, S., CHAM, B., MASUDA, K., ARAKAWA, M., JACQUINET, A., YAMAZUMI, Y., CHEN, S. T., VERLOES, A., OKADA, Y., KATOU, Y., NAKAMURA, T., AKIYAMA, T., GRESSENS, P., FOO, R., PASSEMARD, S., TAN, E. C., EL GHOUZZI, V. & SHIRAHIGE, K. 2016. ARCN1 Mutations Cause a Recognizable Craniofacial Syndrome Due to COPI-Mediated Transport Defects. *Am J Hum Genet,* 99**,** 451-9.
JAVIDAN, Y. & SCHILLING, T. F. 2004. Development of cartilage and bone. *Methods Cell Biol,* 76**,** 415-36.
JEZEWSKI, P. A., FANG, P. K., PAYNE-FERREIRA, T. L. & YELICK, P. C. 2008. Zebrafish Wnt9b synteny and expression during first and second arch, heart, and pectoral fin bud morphogenesis. *Zebrafish,* 5**,** 169-77.
JIANG, R., BUSH, J. O. & LIDRAL, A. C. 2006. Development of the upper lip: morphogenetic and molecular mechanisms. *Dev Dyn,* 235**,** 1152-66.
JINEK, M., CHYLINSKI, K., FONFARA, I., HAUER, M., DOUDNA, J. A. & CHARPENTIER, E. 2012. A programmable dual-RNA-guided DNA endonuclease in adaptive bacterial immunity. *Science,* 337**,** 816-21.
JING, Y., ZHOU, X., HAN, X., JING, J., VON DER MARK, K., WANG, J., DE CROMBRUGGHE, B., HINTON, R. J. & FENG, J. Q. 2015. Chondrocytes Directly Transform into Bone Cells in Mandibular Condyle Growth. *J Dent Res,* 94**,** 1668-75.
KAGUE, E., GALLAGHER, M., BURKE, S., PARSONS, M., FRANZ-ODENDAAL, T. & FISHER, S. 2012. Skeletogenic fate of zebrafish cranial and trunk neural crest. *PLoS One,* 7**,** e47394.
KAHN, J., SHWARTZ, Y., BLITZ, E., KRIEF, S., SHARIR, A., BREITEL, D. A., RATTENBACH, R., RELAIX, F., MAIRE, P., ROUNTREE, R. B., KINGSLEY, D. M. & ZELZER, E. 2009. Muscle contraction is necessary to maintain joint progenitor cell fate. *Dev Cell,* 16**,** 734-43.
KAMIYA, N., YE, L., KOBAYASHI, T., MOCHIDA, Y., YAMAUCHI, M., KRONENBERG, H. M., FENG, J. Q. & MISHINA, Y. 2008. BMP signaling negatively regulates bone mass through sclerostin by inhibiting the canonical Wnt pathway. *Development,* 135**,** 3801-11.

KARSENTY, G. 2003. The complexities of skeletal biology. *Nature,* 423**,** 316-8.
KAWAKAMI, K., TAKEDA, H., KAWAKAMI, N., KOBAYASHI, M., MATSUDA, N. & MISHINA, M. 2004. A transposon-mediated gene trap approach identifies developmentally regulated genes in zebrafish. *Dev Cell,* 7**,** 133-44.
KAWAKAMI, M., OKUDA, H., TATSUMI, K., KIRITA, T. & WANAKA, A. 2014. Inhibition of Wnt/beta-catenin pathway by Dickkopf-1 [corrected] affects midfacial morphogenesis in chick embryo. *J Biosci Bioeng,* 117**,** 664-9.
KIM, K. M., YU, T. K., CHU, H. H., PARK, H. S., JANG, K. Y., MOON, W. S., KANG, M. J., LEE, D. G., KIM, M. H., LEE, J. H. & CHUNG, M. J. 2012. Expression of ER stress and autophagy-related molecules in human non-small cell lung cancer and premalignant lesions. *Int J Cancer,* 131**,** E362-70.
KIM, Y. G., CHA, J. & CHANDRASEGARAN, S. 1996. Hybrid restriction enzymes: zinc finger fusions to Fok I cleavage domain. *Proc Natl Acad Sci U S A,* 93**,** 1156-60.
KIMMEL, C. B., BALLARD, W. W., KIMMEL, S. R., ULLMANN, B. & SCHILLING, T. F. 1995. Stages of embryonic development of the zebrafish. *Dev Dyn,* 203**,** 253-310.
KIMMEL, C. B., DELAURIER, A., ULLMANN, B., DOWD, J. & MCFADDEN, M. 2010. Modes of developmental outgrowth and shaping of a craniofacial bone in zebrafish. *PLoS One,* 5**,** e9475.
KOK, F. O., SHIN, M., NI, C. W., GUPTA, A., GROSSE, A. S., VAN IMPEL, A., KIRCHMAIER, B. C., PETERSON-MADURO, J., KOURKOULIS, G., MALE, I., DESANTIS, D. F., SHEPPARD-TINDELL, S., EBARASI, L., BETSHOLTZ, C., SCHULTE-MERKER, S., WOLFE, S. A. & LAWSON, N. D. 2015. Reverse genetic screening reveals poor correlation between morpholino-induced and mutant phenotypes in zebrafish. *Dev Cell,* 32**,** 97-108.
KONDO, S., SCHUTTE, B. C., RICHARDSON, R. J., BJORK, B. C., KNIGHT, A. S., WATANABE, Y., HOWARD, E., DE LIMA, R. L., DAACK-HIRSCH, S., SANDER, A., MCDONALD-MCGINN, D. M., ZACKAI, E. H., LAMMER, E. J., AYLSWORTH, A. S., ARDINGER, H. H., LIDRAL, A. C., POBER, B. R., MORENO, L., ARCOS-BURGOS, M., VALENCIA, C., HOUDAYER, C., BAHUAU, M., MORETTI-FERREIRA, D., RICHIERI-COSTA, A., DIXON, M. J. & MURRAY, J. C. 2002. Mutations in IRF6 cause Van der Woude and popliteal pterygium syndromes. *Nat Genet,* 32**,** 285-9.
KONIG, N., TROLLE, C., KAPURALIN, K., ADAMEYKO, I., MITRECIC, D., ALDSKOGIUS, H., SHORTLAND, P. J. & KOZLOVA, E. N. 2014. Murine neural crest stem cells and embryonic stem cell-derived neuron precursors survive and differentiate after transplantation in a model of dorsal root avulsion. *J Tissue Eng Regen Med*.
KOZUTSUMI, Y., SEGAL, M., NORMINGTON, K., GETHING, M. J. & SAMBROOK, J. 1988. The presence of malfolded proteins in the endoplasmic reticulum signals the induction of glucose-regulated proteins. *Nature,* 332**,** 462-4.
KRISHNAN, V., BRYANT, H. U. & MACDOUGALD, O. A. 2006. Regulation of bone mass by Wnt signaling. *J Clin Invest,* 116**,** 1202-9.
KRONENBERG, H. M. 2003. Developmental regulation of the growth plate. *Nature,* 423**,** 332-6.
KUAN, Y. S., ROBERSON, S., AKITAKE, C. M., FORTUNO, L., GAMSE, J., MOENS, C. & HALPERN, M. E. 2015. Distinct requirements for Wntless in habenular development. *Dev Biol,* 406**,** 117-28.

KURIHARA, Y., KURIHARA, H., SUZUKI, H., KODAMA, T., MAEMURA, K., NAGAI, R., ODA, H., KUWAKI, T., CAO, W. H., KAMADA, N. & ET AL. 1994. Elevated blood pressure and craniofacial abnormalities in mice deficient in endothelin-1. *Nature,* 368**,** 703-10.

KUROSAKA, H., IULIANELLA, A., WILLIAMS, T. & TRAINOR, P. A. 2014. Disrupting hedgehog and WNT signaling interactions promotes cleft lip pathogenesis. *J Clin Invest,* 124**,** 1660-71.

LANG, M. R., LAPIERRE, L. A., FROTSCHER, M., GOLDENRING, J. R. & KNAPIK, E. W. 2006. Secretory COPII coat component Sec23a is essential for craniofacial chondrocyte maturation. *Nat Genet,* 38**,** 1198-203.

LE PABIC, P., NG, C. & SCHILLING, T. F. 2014. Fat-Dachsous signaling coordinates cartilage differentiation and polarity during craniofacial development. *PLoS Genet,* 10**,** e1004726.

LECLAIR, E. E., MUI, S. R., HUANG, A., TOPCZEWSKA, J. M. & TOPCZEWSKI, J. 2009. Craniofacial skeletal defects of adult zebrafish Glypican 4 (knypek) mutants. *Dev Dyn,* 238**,** 2550-63.

LEWIS, J. L., BONNER, J., MODRELL, M., RAGLAND, J. W., MOON, R. T., DORSKY, R. I. & RAIBLE, D. W. 2004. Reiterated Wnt signaling during zebrafish neural crest development. *Development,* 131**,** 1299-308.

LIU, B., ROOKER, S. M. & HELMS, J. A. 2010. Molecular control of facial morphology. *Semin Cell Dev Biol,* 21**,** 309-13.

LOGAN, C. Y. & NUSSE, R. 2004. The Wnt signaling pathway in development and disease. *Annu Rev Cell Dev Biol,* 20**,** 781-810.

LONG, F., CHUNG, U. I., OHBA, S., MCMAHON, J., KRONENBERG, H. M. & MCMAHON, A. P. 2004. Ihh signaling is directly required for the osteoblast lineage in the endochondral skeleton. *Development,* 131**,** 1309-18.

LONG, F., JOENG, K. S., XUAN, S., EFSTRATIADIS, A. & MCMAHON, A. P. 2006. Independent regulation of skeletal growth by Ihh and IGF signaling. *Dev Biol,* 298**,** 327-33.

LUINI, A. 2011. A brief history of the cisternal progression-maturation model. *Cell Logist,* 1**,** 6-11.

MACKIE, E. J., AHMED, Y. A., TATARCZUCH, L., CHEN, K. S. & MIRAMS, M. 2008. Endochondral ossification: how cartilage is converted into bone in the developing skeleton. *Int J Biochem Cell Biol,* 40**,** 46-62.

MAEDA, K., KOBAYASHI, Y., UDAGAWA, N., UEHARA, S., ISHIHARA, A., MIZOGUCHI, T., KIKUCHI, Y., TAKADA, I., KATO, S., KANI, S., NISHITA, M., MARUMO, K., MARTIN, T. J., MINAMI, Y. & TAKAHASHI, N. 2012. Wnt5a-Ror2 signaling between osteoblast-lineage cells and osteoclast precursors enhances osteoclastogenesis. *Nat Med,* 18**,** 405-12.

MALI, P., YANG, L., ESVELT, K. M., AACH, J., GUELL, M., DICARLO, J. E., NORVILLE, J. E. & CHURCH, G. M. 2013. RNA-guided human genome engineering via Cas9. *Science,* 339**,** 823-6.

MARCU, M. G., DOYLE, M., BERTOLOTTI, A., RON, D., HENDERSHOT, L. & NECKERS, L. 2002. Heat shock protein 90 modulates the unfolded protein response by stabilizing IRE1alpha. *Mol Cell Biol,* 22**,** 8506-13.

MARTINEZ-MENARGUEZ, J. A., PREKERIS, R., OORSCHOT, V. M., SCHELLER, R., SLOT, J. W., GEUZE, H. J. & KLUMPERMAN, J. 2001. Peri-Golgi vesicles contain retrograde but not anterograde proteins consistent with the cisternal progression model of intra-Golgi transport. *J Cell Biol,* 155**,** 1213-24.

MARUYAMA, T., JIANG, M. & HSU, W. 2013. Gpr177, a novel locus for bone mineral density and osteoporosis, regulates osteogenesis and chondrogenesis in skeletal development. *J Bone Miner Res,* 28**,** 1150-9.
MCCARTHY, N., WETHERILL, L., LOVELY, C. B., SWARTZ, M. E., FOROUD, T. M. & EBERHART, J. K. 2013. Pdgfra protects against ethanol-induced craniofacial defects in a zebrafish model of FASD. *Development,* 140**,** 3254-65.
MCCOLLUM, C. W., DUCHARME, N. A., BONDESSON, M. & GUSTAFSSON, J. A. 2011. Developmental toxicity screening in zebrafish. *Birth Defects Res C Embryo Today,* 93**,** 67-114.
MEHTA, R. S. & WAINWRIGHT, P. C. 2008. Functional morphology of the pharyngeal jaw apparatus in moray eels. *J Morphol,* 269**,** 604-19.
MERRILL, A. E., EAMES, B. F., WESTON, S. J., HEATH, T. & SCHNEIDER, R. A. 2008. Mesenchyme-dependent BMP signaling directs the timing of mandibular osteogenesis. *Development,* 135**,** 1223-34.
MILET, C. & MONSORO-BURQ, A. H. 2012. Neural crest induction at the neural plate border in vertebrates. *Dev Biol,* 366**,** 22-33.
MILLER, C. T., SCHILLING, T. F., LEE, K., PARKER, J. & KIMMEL, C. B. 2000. sucker encodes a zebrafish Endothelin-1 required for ventral pharyngeal arch development. *Development,* 127**,** 3815-28.
MILLER, C. T., YELON, D., STAINIER, D. Y. & KIMMEL, C. B. 2003. Two endothelin 1 effectors, hand2 and bapx1, pattern ventral pharyngeal cartilage and the jaw joint. *Development,* 130**,** 1353-65.
MILLER, J. C., TAN, S., QIAO, G., BARLOW, K. A., WANG, J., XIA, D. F., MENG, X., PASCHON, D. E., LEUNG, E., HINKLEY, S. J., DULAY, G. P., HUA, K. L., ANKOUDINOVA, I., COST, G. J., URNOV, F. D., ZHANG, H. S., HOLMES, M. C., ZHANG, L., GREGORY, P. D. & REBAR, E. J. 2011. A TALE nuclease architecture for efficient genome editing. *Nat Biotechnol,* 29**,** 143-8.
MINOUX, M. & RIJLI, F. M. 2010. Molecular mechanisms of cranial neural crest cell migration and patterning in craniofacial development. *Development,* 137**,** 2605-21.
MONROE, D. G., MCGEE-LAWRENCE, M. E., OURSLER, M. J. & WESTENDORF, J. J. 2012. Update on Wnt signaling in bone cell biology and bone disease. *Gene,* 492**,** 1-18.
MONTERO-BALAGUER, M., LANG, M. R., SACHDEV, S. W., KNAPPMEYER, C., STEWART, R. A., DE LA GUARDIA, A., HATZOPOULOS, A. K. & KNAPIK, E. W. 2006. The mother superior mutation ablates foxd3 activity in neural crest progenitor cells and depletes neural crest derivatives in zebrafish. *Dev Dyn,* 235**,** 3199-212.
MOREAU, D., KUMAR, P., WANG, S. C., CHAUMET, A., CHEW, S. Y., CHEVALLEY, H. & BARD, F. 2011. Genome-wide RNAi screens identify genes required for Ricin and PE intoxications. *Dev Cell,* 21**,** 231-44.
MORK, L. & CRUMP, G. 2015. Zebrafish Craniofacial Development: A Window into Early Patterning. *Curr Top Dev Biol,* 115**,** 235-69.
MOSCOU, M. J. & BOGDANOVE, A. J. 2009. A simple cipher governs DNA recognition by TAL effectors. *Science,* 326**,** 1501.
MOSIMANN, C., KAUFMAN, C. K., LI, P., PUGACH, E. K., TAMPLIN, O. J. & ZON, L. I. 2011. Ubiquitous transgene expression and Cre-based recombination driven by the ubiquitin promoter in zebrafish. *Development,* 138**,** 169-77.

MUKHERJEE, K., ISHII, K., PILLALAMARRI, V., KAMMIN, T., ATKIN, J. F., HICKEY, S. E., XI, Q. J., ZEPEDA, C. J., GUSELLA, J. F., TALKOWSKI, M. E., MORTON, C. C., MAAS, R. L. & LIAO, E. C. 2016. Actin capping protein CAPZB regulates cell morphology, differentiation, and neural crest migration in craniofacial morphogenesisdagger. *Hum Mol Genet,* 25**,** 1255-70.

NAIR, S., LI, W., CORNELL, R. & SCHILLING, T. F. 2007. Requirements for Endothelin type-A receptors and Endothelin-1 signaling in the facial ectoderm for the patterning of skeletogenic neural crest cells in zebrafish. *Development,* 134**,** 335-45.

NAKASHIMA, K., ZHOU, X., KUNKEL, G., ZHANG, Z., DENG, J. M., BEHRINGER, R. R. & DE CROMBRUGGHE, B. 2002. The novel zinc finger-containing transcription factor osterix is required for osteoblast differentiation and bone formation. *Cell,* 108**,** 17-29.

NAKAYAMA, N., HAN, C. Y., CAM, L., LEE, J. I., PRETORIUS, J., FISHER, S., ROSENFELD, R., SCULLY, S., NISHINAKAMURA, R., DURYEA, D., VAN, G., BOLON, B., YOKOTA, T. & ZHANG, K. 2004. A novel chordin-like BMP inhibitor, CHL2, expressed preferentially in chondrocytes of developing cartilage and osteoarthritic joint cartilage. *Development,* 131**,** 229-40.

NAMBA, T., ISHIHARA, T., TANAKA, K., HOSHINO, T. & MIZUSHIMA, T. 2007. Transcriptional activation of ATF6 by endoplasmic reticulum stressors. *Biochem Biophys Res Commun,* 355**,** 543-8.

NASEVICIUS, A. & EKKER, S. C. 2000. Effective targeted gene 'knockdown' in zebrafish. *Nat Genet,* 26**,** 216-20.

NEUHAUSS, S. C., SOLNICA-KREZEL, L., SCHIER, A. F., ZWARTKRUIS, F., STEMPLE, D. L., MALICKI, J., ABDELILAH, S., STAINIER, D. Y. & DRIEVER, W. 1996. Mutations affecting craniofacial development in zebrafish. *Development,* 123**,** 357-67.

NOONAN, K. J., HUNZIKER, E. B., NESSLER, J. & BUCKWALTER, J. A. 1998. Changes in cell, matrix compartment, and fibrillar collagen volumes between growth-plate zones. *J Orthop Res,* 16**,** 500-8.

NOORDERMEER, J., KLINGENSMITH, J., PERRIMON, N. & NUSSE, R. 1994. dishevelled and armadillo act in the wingless signalling pathway in Drosophila. *Nature,* 367**,** 80-3.

NOWLAN, N. C., MURPHY, P. & PRENDERGAST, P. J. 2008. A dynamic pattern of mechanical stimulation promotes ossification in avian embryonic long bones. *J Biomech,* 41**,** 249-58.

NUSSE, R. 2015. Cell signalling: Disarming Wnt. *Nature,* 519**,** 163-4.

NUSSE, R., BROWN, A., PAPKOFF, J., SCAMBLER, P., SHACKLEFORD, G., MCMAHON, A., MOON, R. & VARMUS, H. 1991. A new nomenclature for int-1 and related genes: the Wnt gene family. *Cell,* 64**,** 231.

NUSSE, R. & VARMUS, H. E. 1982. Many tumors induced by the mouse mammary tumor virus contain a provirus integrated in the same region of the host genome. *Cell,* 31**,** 99-109.

NUSSLEIN-VOLHARD, C. & WIESCHAUS, E. 1980. Mutations affecting segment number and polarity in Drosophila. *Nature,* 287**,** 795-801.

OLSEN, B. R., REGINATO, A. M. & WANG, W. 2000. Bone development. *Annu Rev Cell Dev Biol,* 16**,** 191-220.

OSLOWSKI, C. M. & URANO, F. 2011. Measuring ER stress and the unfolded protein response using mammalian tissue culture system. *Methods Enzymol,* 490**,** 71-92.

PAN, Y. A., FREUNDLICH, T., WEISSMAN, T. A., SCHOPPIK, D., WANG, X. C., ZIMMERMAN, S., CIRUNA, B., SANES, J. R., LICHTMAN, J. W. & SCHIER, A. F. 2013. Zebrabow: multispectral cell labeling for cell tracing and lineage analysis in zebrafish. *Development,* 140**,** 2835-46.

PARSONS, K. J. & ALBERTSON, R. C. 2009. Roles for Bmp4 and CaM1 in shaping the jaw: evo-devo and beyond. *Annu Rev Genet,* 43**,** 369-88.

PARSONS, K. J., TRENT TAYLOR, A., POWDER, K. E. & ALBERTSON, R. C. 2014. Wnt signalling underlies the evolution of new phenotypes and craniofacial variability in Lake Malawi cichlids. *Nat Commun,* 5**,** 3629.

PARSONS, M. J., POLLARD, S. M., SAUDE, L., FELDMAN, B., COUTINHO, P., HIRST, E. M. & STEMPLE, D. L. 2002. Zebrafish mutants identify an essential role for laminins in notochord formation. *Development,* 129**,** 3137-46.

PAUL, S., SCHINDLER, S., GIOVANNONE, D., DE MILLO TERRAZZANI, A., MARIANI, F. V. & CRUMP, J. G. 2016. Ihha induces hybrid cartilage-bone cells during zebrafish jawbone regeneration. *Development*.

PEREZ, E. E., WANG, J., MILLER, J. C., JOUVENOT, Y., KIM, K. A., LIU, O., WANG, N., LEE, G., BARTSEVICH, V. V., LEE, Y. L., GUSCHIN, D. Y., RUPNIEWSKI, I., WAITE, A. J., CARPENITO, C., CARROLL, R. G., ORANGE, J. S., URNOV, F. D., REBAR, E. J., ANDO, D., GREGORY, P. D., RILEY, J. L., HOLMES, M. C. & JUNE, C. H. 2008. Establishment of HIV-1 resistance in CD4+ T cells by genome editing using zinc-finger nucleases. *Nat Biotechnol,* 26**,** 808-16.

PIOTROWSKI, T., SCHILLING, T. F., BRAND, M., JIANG, Y. J., HEISENBERG, C. P., BEUCHLE, D., GRANDEL, H., VAN EEDEN, F. J., FURUTANI-SEIKI, M., GRANATO, M., HAFFTER, P., HAMMERSCHMIDT, M., KANE, D. A., KELSH, R. N., MULLINS, M. C., ODENTHAL, J., WARGA, R. M. & NUSSLEIN-VOLHARD, C. 1996. Jaw and branchial arch mutants in zebrafish II: anterior arches and cartilage differentiation. *Development,* 123**,** 345-56.

PORT, F., KUSTER, M., HERR, P., FURGER, E., BANZIGER, C., HAUSMANN, G. & BASLER, K. 2008. Wingless secretion promotes and requires retromer-dependent cycling of Wntless. *Nat Cell Biol,* 10**,** 178-85.

QUARTO, N., WAN, D. C., KWAN, M. D., PANETTA, N. J., LI, S. & LONGAKER, M. T. 2010. Origin matters: differences in embryonic tissue origin and Wnt signaling determine the osteogenic potential and healing capacity of frontal and parietal calvarial bones. *J Bone Miner Res,* 25**,** 1680-94.

RICKS, J. E., RYDER, V. M., BRIDGEWATER, L. C., SCHAALJE, B. & SEEGMILLER, R. E. 2002. Altered mandibular development precedes the time of palate closure in mice homozygous for disproportionate micromelia: an oral clefting model supporting the Pierre-Robin sequence. *Teratology,* 65**,** 116-20.

RIJSEWIJK, F., SCHUERMANN, M., WAGENAAR, E., PARREN, P., WEIGEL, D. & NUSSE, R. 1987. The Drosophila homolog of the mouse mammary oncogene int-1 is identical to the segment polarity gene wingless. *Cell,* 50**,** 649-57.

RIVADENEIRA, F., STYRKARSDOTTIR, U., ESTRADA, K., HALLDORSSON, B. V., HSU, Y. H., RICHARDS, J. B., ZILLIKENS, M. C., KAVVOURA, F. K., AMIN, N., AULCHENKO, Y. S., CUPPLES, L. A., DELOUKAS, P., DEMISSIE, S., GRUNDBERG, E., HOFMAN, A., KONG, A., KARASIK, D., VAN MEURS, J. B., OOSTRA, B., PASTINEN, T., POLS, H. A., SIGURDSSON, G., SORANZO, N., THORLEIFSSON, G.,

THORSTEINSDOTTIR, U., WILLIAMS, F. M., WILSON, S. G., ZHOU, Y., RALSTON, S. H., VAN DUIJN, C. M., SPECTOR, T., KIEL, D. P., STEFANSSON, K., IOANNIDIS, J. P., UITTERLINDEN, A. G. & GENETIC FACTORS FOR OSTEOPOROSIS, C. 2009. Twenty bone-mineral-density loci identified by large-scale meta-analysis of genome-wide association studies. *Nat Genet,* 41**,** 1199-206.

ROBBINS, J., BLONDEL, B. J., GALLAHAN, D. & CALLAHAN, R. 1992. Mouse mammary tumor gene int-3: a member of the notch gene family transforms mammary epithelial cells. *J Virol,* 66**,** 2594-9.

ROBERTS, R. J. 2005. How restriction enzymes became the workhorses of molecular biology. *Proc Natl Acad Sci U S A,* 102**,** 5905-8.

ROCHARD, L., GASTER, S., LING, I., HARLAND, R., HALPERN, M. E. & LIAO, E. C. in press. Roles of Wnt pathway genes *wls, wnt9a, wnt5b, frzb* and *gpc4* in regulating convergent-extension during palate morphogenesis. *Development*.

ROCHARD, L., MONICA, S. D., LING, I. T., KONG, Y., ROBERSON, S., HARLAND, R., HALPERN, M. & LIAO, E. C. 2016. Roles of Wnt pathway genes wls, wnt9a, wnt5b, frzb and gpc4 in regulating convergent-extension during palate morphogenesis. *Development*.

RODDA, S. J. & MCMAHON, A. P. 2006. Distinct roles for Hedgehog and canonical Wnt signaling in specification, differentiation and maintenance of osteoblast progenitors. *Development,* 133**,** 3231-44.

ROSSI, A., KONTARAKIS, Z., GERRI, C., NOLTE, H., HOLPER, S., KRUGER, M. & STAINIER, D. Y. 2015. Genetic compensation induced by deleterious mutations but not gene knockdowns. *Nature,* 524**,** 230-3.

SARMAH, S., BARRALLO-GIMENO, A., MELVILLE, D. B., TOPCZEWSKI, J., SOLNICA-KREZEL, L. & KNAPIK, E. W. 2010. Sec24D-dependent transport of extracellular matrix proteins is required for zebrafish skeletal morphogenesis. *PLoS One,* 5**,** e10367.

SAUKA-SPENGLER, T. & BRONNER, M. 2010. Snapshot: neural crest. *Cell,* 143**,** 486-486 e1.

SAVOSTIN-ASLING, I. & ASLING, C. W. 1973. Resorption of calcified cartilage as seen in Meckel's cartilage of rats. *Anat Rec,* 176**,** 345-59.

SCHEKMAN, R. & ORCI, L. 1996. Coat proteins and vesicle budding. *Science,* 271**,** 1526-33.

SCHILLING, T. F. & KIMMEL, C. B. 1994. Segment and cell type lineage restrictions during pharyngeal arch development in the zebrafish embryo. *Development,* 120**,** 483-94.

SCHILLING, T. F. & KIMMEL, C. B. 1997. Musculoskeletal patterning in the pharyngeal segments of the zebrafish embryo. *Development,* 124**,** 2945-60.

SCHILLING, T. F., PIOTROWSKI, T., GRANDEL, H., BRAND, M., HEISENBERG, C. P., JIANG, Y. J., BEUCHLE, D., HAMMERSCHMIDT, M., KANE, D. A., MULLINS, M. C., VAN EEDEN, F. J., KELSH, R. N., FURUTANI-SEIKI, M., GRANATO, M., HAFFTER, P., ODENTHAL, J., WARGA, R. M., TROWE, T. & NUSSLEIN-VOLHARD, C. 1996. Jaw and branchial arch mutants in zebrafish I: branchial arches. *Development,* 123**,** 329-44.

SCHNEIDER, R. A. & HELMS, J. A. 2003. The cellular and molecular origins of beak morphology. *Science,* 299**,** 565-8.

SCRIVEN, P., COULSON, S., HAINES, R., BALASUBRAMANIAN, S., CROSS, S. & WYLD, L. 2009. Activation and clinical significance of the unfolded protein response in breast cancer. *Br J Cancer,* 101**,** 1692-8.

SEMENOV, M. V., HABAS, R., MACDONALD, B. T. & HE, X. 2007. SnapShot: Noncanonical Wnt Signaling Pathways. *Cell,* 131**,** 1378.
SEPICH, D. S., USMANI, M., PAWLICKI, S. & SOLNICA-KREZEL, L. 2011. Wnt/PCP signaling controls intracellular position of MTOCs during gastrulation convergence and extension movements. *Development,* 138**,** 543-52.
SHWARTZ, Y., FARKAS, Z., STERN, T., ASZODI, A. & ZELZER, E. 2012. Muscle contraction controls skeletal morphogenesis through regulation of chondrocyte convergent extension. *Dev Biol,* 370**,** 154-63.
SIMOES-COSTA, M. & BRONNER, M. E. 2013. Insights into neural crest development and evolution from genomic analysis. *Genome Res,* 23**,** 1069-80.
SINGH, S. P., HOLDWAY, J. E. & POSS, K. D. 2012. Regeneration of amputated zebrafish fin rays from de novo osteoblasts. *Dev Cell,* 22**,** 879-86.
SISSON, B. E., DALE, R. M., MUI, S. R., TOPCZEWSKA, J. M. & TOPCZEWSKI, J. 2015. A role of glypican4 and wnt5b in chondrocyte stacking underlying craniofacial cartilage morphogenesis. *Mech Dev,* 138 Pt 3**,** 279-90.
SOVOLYOVA, N., HEALY, S., SAMALI, A. & LOGUE, S. E. 2014. Stressed to death - mechanisms of ER stress-induced cell death. *Biol Chem,* 395**,** 1-13.
SPATER, D., HILL, T. P., O'SULLIVAN R, J., GRUBER, M., CONNER, D. A. & HARTMANN, C. 2006. Wnt9a signaling is required for joint integrity and regulation of Ihh during chondrogenesis. *Development,* 133**,** 3039-49.
ST-JACQUES, B., HAMMERSCHMIDT, M. & MCMAHON, A. P. 1999. Indian hedgehog signaling regulates proliferation and differentiation of chondrocytes and is essential for bone formation. *Genes Dev,* 13**,** 2072-86.
STERNBERG, S. H., REDDING, S., JINEK, M., GREENE, E. C. & DOUDNA, J. A. 2014. DNA interrogation by the CRISPR RNA-guided endonuclease Cas9. *Nature,* 507**,** 62-7.
STORM, E. E. & KINGSLEY, D. M. 1999. GDF5 coordinates bone and joint formation during digit development. *Dev Biol,* 209**,** 11-27.
SUMMERTON, J. & WELLER, D. 1997. Morpholino antisense oligomers: design, preparation, and properties. *Antisense Nucleic Acid Drug Dev,* 7**,** 187-95.
SZOSTAK, J. W., ORR-WEAVER, T. L., ROTHSTEIN, R. J. & STAHL, F. W. 1983. The double-strand-break repair model for recombination. *Cell,* 33**,** 25-35.
TADA, M. & SMITH, J. C. 2000. Xwnt11 is a target of Xenopus Brachyury: regulation of gastrulation movements via Dishevelled, but not through the canonical Wnt pathway. *Development,* 127**,** 2227-38.
TAKAHASHI, N., MAEDA, K., ISHIHARA, A., UEHARA, S. & KOBAYASHI, Y. 2011. Regulatory mechanism of osteoclastogenesis by RANKL and Wnt signals. *Front Biosci (Landmark Ed),* 16**,** 21-30.
TENG, L., MUNDELL, N. A., FRIST, A. Y., WANG, Q. & LABOSKY, P. A. 2008. Requirement for Foxd3 in the maintenance of neural crest progenitors. *Development,* 135**,** 1615-24.
THISSE, C. & THISSE, B. 2008. High-resolution in situ hybridization to whole-mount zebrafish embryos. *Nat Protoc,* 3**,** 59-69.
TOPCZEWSKI, J., DALE, R. M. & SISSON, B. E. 2011. Planar cell polarity signaling in craniofacial development. *Organogenesis,* 7**,** 255-9.
TOPOL, L., CHEN, W., SONG, H., DAY, T. F. & YANG, Y. 2009. Sox9 inhibits Wnt signaling by promoting beta-catenin phosphorylation in the nucleus. *J Biol Chem,* 284**,** 3323-33.

TOWNLEY, A. K., FENG, Y., SCHMIDT, K., CARTER, D. A., PORTER, R., VERKADE, P. & STEPHENS, D. J. 2008. Efficient coupling of Sec23-Sec24 to Sec13-Sec31 drives COPII-dependent collagen secretion and is essential for normal craniofacial development. *J Cell Sci,* 121**,** 3025-34.

TU, X., JOENG, K. S., NAKAYAMA, K. I., NAKAYAMA, K., RAJAGOPAL, J., CARROLL, T. J., MCMAHON, A. P. & LONG, F. 2007. Noncanonical Wnt signaling through G protein-linked PKCdelta activation promotes bone formation. *Dev Cell,* 12**,** 113-27.

URNOV, F. D., MILLER, J. C., LEE, Y. L., BEAUSEJOUR, C. M., ROCK, J. M., AUGUSTUS, S., JAMIESON, A. C., PORTEUS, M. H., GREGORY, P. D. & HOLMES, M. C. 2005. Highly efficient endogenous human gene correction using designed zinc-finger nucleases. *Nature,* 435**,** 646-51.

VAN AMERONGEN, R. & NUSSE, R. 2009. Towards an integrated view of Wnt signaling in development. *Development,* 136**,** 3205-14.

VEEMAN, M. T., AXELROD, J. D. & MOON, R. T. 2003. A second canon. Functions and mechanisms of beta-catenin-independent Wnt signaling. *Dev Cell,* 5**,** 367-77.

VERDUZCO, D. & AMATRUDA, J. F. 2011. Analysis of cell proliferation, senescence, and cell death in zebrafish embryos. *Methods Cell Biol,* 101**,** 19-38.

WALHOUT, A. J., TEMPLE, G. F., BRASCH, M. A., HARTLEY, J. L., LORSON, M. A., VAN DEN HEUVEL, S. & VIDAL, M. 2000. GATEWAY recombinational cloning: application to the cloning of large numbers of open reading frames or ORFeomes. *Methods Enzymol,* 328**,** 575-92.

WALKER, M. B. & KIMMEL, C. B. 2007. A two-color acid-free cartilage and bone stain for zebrafish larvae. *Biotech Histochem,* 82**,** 23-8.

WALLINGFORD, J. B., FRASER, S. E. & HARLAND, R. M. 2002. Convergent extension: the molecular control of polarized cell movement during embryonic development. *Dev Cell,* 2**,** 695-706.

WANG, J., MARK, S., ZHANG, X., QIAN, D., YOO, S. J., RADDE-GALLWITZ, K., ZHANG, Y., LIN, X., COLLAZO, A., WYNSHAW-BORIS, A. & CHEN, P. 2005. Regulation of polarized extension and planar cell polarity in the cochlea by the vertebrate PCP pathway. *Nat Genet,* 37**,** 980-5.

WANG, M. & KAUFMAN, R. J. 2014. The impact of the endoplasmic reticulum protein-folding environment on cancer development. *Nat Rev Cancer,* 14**,** 581-97.

WATERS, M. G., SERAFINI, T. & ROTHMAN, J. E. 1991. 'Coatomer': a cytosolic protein complex containing subunits of non-clathrin-coated Golgi transport vesicles. *Nature,* 349**,** 248-51.

WATKIN, L. B., JESSEN, B., WISZNIEWSKI, W., VECE, T. J., JAN, M., SHA, Y., THAMSEN, M., SANTOS-CORTEZ, R. L., LEE, K., GAMBIN, T., FORBES, L. R., LAW, C. S., STRAY-PEDERSEN, A., CHENG, M. H., MACE, E. M., ANDERSON, M. S., LIU, D., TANG, L. F., NICHOLAS, S. K., NAHMOD, K., MAKEDONAS, G., CANTER, D. L., KWOK, P. Y., HICKS, J., JONES, K. D., PENNEY, S., JHANGIANI, S. N., ROSENBLUM, M. D., DELL, S. D., WATERFIELD, M. R., PAPA, F. R., MUZNY, D. M., ZAITLEN, N., LEAL, S. M., GONZAGA-JAUREGUI, C., BAYLOR-HOPKINS CENTER FOR MENDELIAN, G., BOERWINKLE, E., EISSA, N. T., GIBBS, R. A., LUPSKI, J. R., ORANGE, J. S. & SHUM, A. K. 2015. COPA mutations impair ER-Golgi transport and cause hereditary autoimmune-mediated lung disease and arthritis. *Nat Genet,* 47**,** 654-60.

WESTERFIELD, M. 1995. *The Zebrafish Book* Eugene, Oregon, University of Oregon Press
WIESCHAUS, E. & RIGGLEMAN, R. 1987. Autonomous requirements for the segment polarity gene armadillo during Drosophila embryogenesis. *Cell,* 49**,** 177-84.
WILKIE, A. O. & MORRISS-KAY, G. M. 2001. Genetics of craniofacial development and malformation. *Nat Rev Genet,* 2**,** 458-68.
WILLEMS, B., TAO, S., YU, T., HUYSSEUNE, A., WITTEN, P. E. & WINKLER, C. 2015. The Wnt Co-Receptor Lrp5 Is Required for Cranial Neural Crest Cell Migration in Zebrafish. *PLoS One,* 10**,** e0131768.
WU, B. T., WEN, S. H., HWANG, S. P., HUANG, C. J. & KUAN, Y. S. 2015. Control of Wnt5b secretion by Wntless modulates chondrogenic cell proliferation through fine-tuning fgf3 expression. *J Cell Sci,* 128**,** 2328-39.
YAN, Y. L., MILLER, C. T., NISSEN, R. M., SINGER, A., LIU, D., KIRN, A., DRAPER, B., WILLOUGHBY, J., MORCOS, P. A., AMSTERDAM, A., CHUNG, B. C., WESTERFIELD, M., HAFFTER, P., HOPKINS, N., KIMMEL, C. & POSTLETHWAIT, J. H. 2002. A zebrafish sox9 gene required for cartilage morphogenesis. *Development,* 129**,** 5065-79.
YANG, L., TSANG, K. Y., TANG, H. C., CHAN, D. & CHEAH, K. S. 2014. Hypertrophic chondrocytes can become osteoblasts and osteocytes in endochondral bone formation. *Proc Natl Acad Sci U S A,* 111**,** 12097-102.
YANG, Y., TOPOL, L., LEE, H. & WU, J. 2003. Wnt5a and Wnt5b exhibit distinct activities in coordinating chondrocyte proliferation and differentiation. *Development,* 130**,** 1003-15.
YE, J., RAWSON, R. B., KOMURO, R., CHEN, X., DAVE, U. P., PRYWES, R., BROWN, M. S. & GOLDSTEIN, J. L. 2000. ER stress induces cleavage of membrane-bound ATF6 by the same proteases that process SREBPs. *Mol Cell,* 6**,** 1355-64.
YIN, H., XUE, W., CHEN, S., BOGORAD, R. L., BENEDETTI, E., GROMPE, M., KOTELIANSKY, V., SHARP, P. A., JACKS, T. & ANDERSON, D. G. 2014. Genome editing with Cas9 in adult mice corrects a disease mutation and phenotype. *Nat Biotechnol,* 32**,** 551-3.
YU, J., CHIA, J., CANNING, C. A., JONES, C. M., BARD, F. A. & VIRSHUP, D. M. 2014. WLS retrograde transport to the endoplasmic reticulum during Wnt secretion. *Dev Cell,* 29**,** 277-91.
ZECCA, M., BASLER, K. & STRUHL, G. 1996. Direct and long-range action of a wingless morphogen gradient. *Cell,* 87**,** 833-44.
ZHANG, F., CONG, L., LODATO, S., KOSURI, S., CHURCH, G. M. & ARLOTTA, P. 2011. Efficient construction of sequence-specific TAL effectors for modulating mammalian transcription. *Nat Biotechnol,* 29**,** 149-53.
ZHANG, P., ZHOU, L., PEI, C., LIN, X. & YUAN, Z. 2016. Dysfunction of Wntless triggers the retrograde Golgi-to-ER transport of Wingless and induces ER stress. *Sci Rep,* 6**,** 19418.
ZHONG, Z., ZYLSTRA-DIEGEL, C. R., SCHUMACHER, C. A., BAKER, J. J., CARPENTER, A. C., RAO, S., YAO, W., GUAN, M., HELMS, J. A., LANE, N. E., LANG, R. A. & WILLIAMS, B. O. 2012. Wntless functions in mature osteoblasts to regulate bone mass. *Proc Natl Acad Sci U S A,* 109**,** E2197-204.
ZHOU, X., VON DER MARK, K., HENRY, S., NORTON, W., ADAMS, H. & DE CROMBRUGGHE, B. 2014. Chondrocytes transdifferentiate into osteoblasts in endochondral bone during development, postnatal growth and fracture healing in mice. *PLoS Genet,* 10**,** e1004820.

ZHU, X., ZHU, H., ZHANG, L., HUANG, S., CAO, J., MA, G., FENG, G., HE, L., YANG, Y. & GUO, X. 2012. Wls-mediated Wnts differentially regulate distal limb patterning and tissue morphogenesis. *Dev Biol,* 365**,** 328-38.
ZOLTEWICZ, J. S. & GERHART, J. C. 1997. The Spemann organizer of Xenopus is patterned along its anteroposterior axis at the earliest gastrula stage. *Dev Biol,* 192**,** 482-91.

Appendix

MASSACHUSETTS GENERAL HOSPITAL

Institutional Animal Care and Use Committee
Massachusetts General Hospital
149 13th Street
Charlestown, MA 02129
Tel: (617) 726-3495
Fax: (617) 724-2475

Notification of IACUC Review
Protocol #: 2010N000106

Date: 3/31/2014

To: Chienwei Chienwei Liao, MD, Ph.D
MGH, Surgery
Wang Ambulatory Care Center
Massachusetts General Hospital
15 Parkman St.
Boston
02114-3117

From: Diane McCabe IACUC Manager
Research Management

Title of Protocol:	Zebrafish embryonic craniofacial development
Sponsor(s):	Brigham and Women's Hospital, Inc.
Species / Number:	Fish/12316
Amendment #:	AME7
Expiration Date:	6/16/2016
Annual Report Date:	6/16/2014

This Amendment has been reviewed and approved by the IACUC – OLAW Assurance # A3596-01. The protocol as submitted and reviewed conforms to the USDA Animal Welfare Act, PHS Policy on Humane Care and Use of Laboratory Animals, the "ILAR Guide for the Care and Use of Laboratory Animals" and other applicable laws and regulations. The protocol is approved for a three-year period, subject to submission of annual reports.

Please note that if an IACUC member had a conflict of interest with regard to the review of this protocol, that member left the room during the discussion and the vote on this project.

As Principal Investigator you are responsible for the following:
1. Compliance with IACUC Policies governing the care and use of animals.
2. Submission using Insight of changes to this project for IACUC review and approval prior to initiation of the change.
3. Submission of annual progress reports to the IACUC for review and approval.
4. Adherence to safety requirements for the use of the following hazardous agents:

MASSACHUSETTS GENERAL HOSPITAL
Institutional Animal Care and Use Committee
Massachusetts General Hospital
149 13th Street
Charlestown, MA 02129
Tel: (617) 726-3495
Fax: (617) 724-2475

TOXIC CHEMICALS
Contact the Animals Facility Manager when animals are ordered to begin the protocol.

2013D004276 Sponsor/Funding was added.

The IACUC can and will terminate projects that are not in compliance with these requirements. Direct questions, correspondence and forms to Diane McCabe, the IACUC Manager, Tel: 617-724-9718, Fax: (617) 724-2475.

CC: Chienwei Chienwei Liao, MD, Ph.D
David Allen Lee Machon, BS